Polyspectral Signal Analysis Techniques for Condition Based Maintenance of Helicopter Drive-Train System

by

Mohammed Ahmed Hassan Mohammed

Bachelor of Scince
Cairo University, Egypt, 2001

Master of Science
Cairo University, Egypt, 2004

Submitted in Partial Fulfillment of the Requirements

for the Degree of Doctor of Philosophy in

Electrical Engineering

College of Engineering and Computing

University of South Carolina

2013

Accepted by:

Yong-June Shin, Major Professor

Charles Brice, Committee Member

Herbert Ginn, Committee Member

Abdel E. Bayoumi, Committee Member

Lacy Ford, Vice Provost and Dean of Graduate Studies

Dedication

To my beloved mother.

&

To my lovely wife Hanaa, and my kids Ahmed and Malack.

Acknowledgments

I would like to express my sincere gratitude to my dissertation advisor, Dr. Yong-June Shin, for his invaluable support and guidance throughout my doctoral study in the University of South Carolina. His continual, enthusiastic efforts to expand my academic knowledge, critical thinking, and effective communication skill were priceless and will help me through out the course of my future carrier.

I would also like to thank the distinguished members of my dissertation committee: Dr. Charles Brice, Dr. Herbert Ginn, Dr. Abdel E. Bayoumi. They gave me much valuable advice and guidance during my research which lead to the successful completion of this dissertation. In particular, I would like to acknowledge Dr. Bayoumi for his effort making all possible resources of the CBM center available to complete this research. Without his guidance and support, my success in completing this doctoral work would not have been possible.

I would also like to express my thanks to my fellow graduate students and my friends and the members of the Power IT research group in the Department of Electrical Engineering, and the CBM research center in the Department of Mechanical Engineering. A special thanks to my friend David Coats for his invaluable discussions and continuous help. He was always there extending a helping hand whenever I needed him.

I would also like to extend thanks to the Egyptian Government for my scholarship through the Government Mission program.

Most greatly I am indebted to my God, from whom all of my blessings flow, and to my loving and loyal family, particularly my mother who supported me through many

difficult times early in my life and provided an emotional, financial, and spiritual foundation which shaped my character and my work ethic into what they are today. Finally, I dedicate this work to my lovely wife, Hanaa Abu Baker. Her optimistic outlook, spiritual guidance, and unwavering commitment and support have motivated and inspired me to the finish during both the good and the inevitable difficult times.

Mohammed A. Hassan Mohammed

The University of South Carolina

July 2013

Abstract

For an efficient maintenance of a diverse fleet of air- and rotorcraft, effective condition based maintenance (CBM) must be established based on rotating components monitored vibration signals. In this dissertation, we present theory and applications of polyspectral signal processing techniques for condition based maintenance of critical components in the AH-64D helicopter tail rotor drive train system. Currently available vibration-monitoring tools are mostly built based on auto- and cross-power spectral analysis which have limited performance in detecting frequency correlations higher than second order. Studying higher order correlations provides more information about the mechanical system which helps in building more accurate diagnostic models using the same collected vibration data. Based on bispectrum as higher order spectral analysis tools, new signal processing techniques are developed to assess health conditions of different critical rotating-components. Real-world vibration data are collected from a dedicated AH-64D helicopter drive-train research test bed at the CBM center, University of South Carolina, where experimental tests are conducted to simulate accelerated conditioning in the tail rotor drive-train components.

First, cross-bispectral analysis is utilized to investigate quadratic nonlinear relationship between two vibration signals simultaneously collected from the forward and afterward hanger bearing positions in the AH-64D helicopter tail rotor drive train. Based on cross-bispectrum, quadratic nonlinear transfer function is presented to model second order nonlinearity in the drive shaft running between the two hanger bearings. Then, quadratic-nonlinearity coupling coefficient between frequency harmonics of the rotating shafts is used as condition metric to study different seeded

shaft faults compared to baseline case, namely: 1)- shaft misalignment, 2)- shaft imbalance, and 3)- combination of shaft misalignment and imbalance. Magnitude response of the proposed quadratic-nonlinearity coupling, $A_{QC}(1R, 1R)$, shows ability to detect the fault in all the studied shaft cases. Moreover, using the phase of the proposed quadratic-nonlinearity coupling shows better capabilities in distinguishing the four studied shaft settings than the conventional linear coupling based on cross-power spectrum. Phase of the $A_{QC}(1R, 1R)$ metric shows more consistent results comparing vibrations from the same shaft-conditions. It also shows bigger phase difference between the different studied cases without overlap among them. Bigger phase difference relaxes the requirements when setting threshold values to diagnose different faulted cases.

We also develop a new concept of Quadratic-Nonlinearity Power-Index spectrum, $QNLPI(f)$, that can be used in signal detection and classification, based on bicoherence spectrum. The proposed $QNLPI(f)$ is derived as a projection of the three-dimensional bicoherence spectrum into two-dimensional spectrum that quantitatively describes how much of the mean square power at certain frequency f is generated due to nonlinear quadratic interaction between different frequency components. The proposed index, $QNLPI(f)$, can be used to simplify the study of bispectrum and bicoherence signal spectra. It also inherits useful characteristics from the bicoherence such as high immunity to additive gaussian noise, high capability of nonlinear-systems identifications, and amplification invariance. The quadratic-nonlinear power spectral density $P_{QNL}(f)$ and percentage of quadratic nonlinear power $PQNLP$ are also introduced based on the $QNLPI(f)$. The $QNLPI(f)$ spectrum enables us to gain more details about nonlinear harmonic generation patterns that can be used to distinguish between different cases of mechanical faults, which in turn helps to gaining more diagnostic/prognostic capabilities.

Finally, the behavior of the helicopter's tail-rotor drive-train under more than

one simultaneous fault is investigated using the proposed signal analysis techniques. In the presence of drive-shaft faults, shaft harmonics dominate the power spectra of the vibration signals collected form faulted hanger-bearing making it hard to detect bearing's faults. Also, spectral interaction among different fault frequencies leads to unexpected frequencies to appear in the vibration spectrum which can not be explained using conventional power spectral analysis. However, bispectral analysis tools not only detect the bearing's faults in this extreme case of multi-faulted components, but also are able relate all the frequencies to their root causes and successfully links the signal processing to the physics of the underlying faults in the drive-train system.

Table of Contents

List of Tables

List of Figures

Chapter 1

Introduction

1.1 Condition Based Maintenance (CBM)

Condition Based Maintenance (CBM) is an approach where troubleshooting and repairing machines, or systems, are performed based on continuous monitoring of their parts' condition. Maintenance actions are taken based on observation and analysis rather than on event of failure (Corrective Maintenance) or by following a strict maintenance time schedule (Preventive Maintenance) [1]. Figure 1.1 summarizes different methodologies of maintenance practice. CBM, if properly established and implemented, could significantly reduce the number or extent of maintenance operations, eliminate scheduled inspections, reduce false alarms, detect incipient faults, enable autonomic diagnostics, predict useful remaining life, enhance reliability, enable information management, enable autonomic logistics, and consequently reduced life cycle costs [2].

A full CBM system consists of several functional layers as shown in Figure 1.2. According to Open Systems Architecture for Condition-based Maintenance (OSA-CBM) standard [3] and Condition Monitoring and Diagnostics of Machines ISO-13374 standard [4], followings are elements of CBM system:

Data Acquisition: converts an output from a sensor measurement to a digital parameter, representing a physical quantity and related information such as the time, velocity, acceleration, sensor configuration.

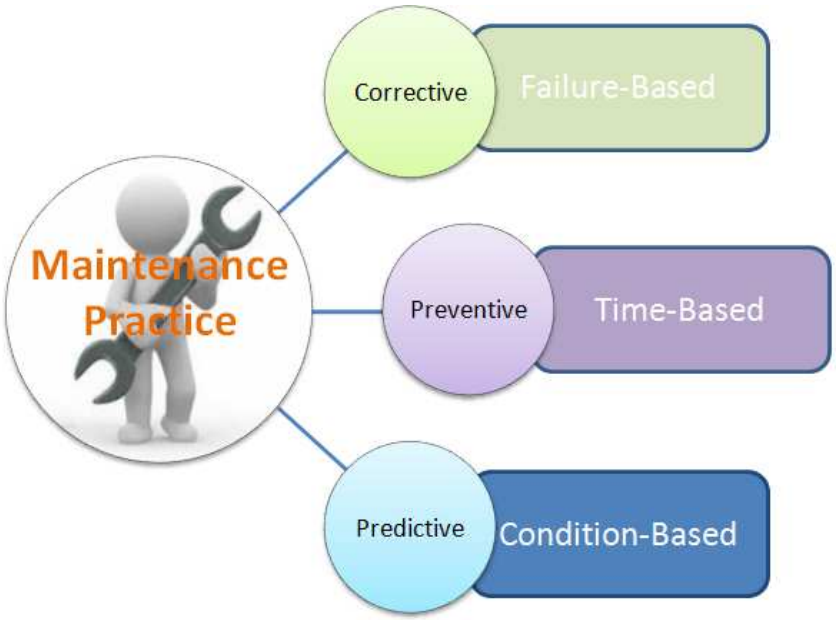

Figure 1.1 Different methodologies of maintenance practice

Data Manipulation: performs signal analysis, computes meaningful descriptors, and derives virtual sensor readings from the raw measurements.

State Detection: searches for abnormalities whenever new data is acquired, and determines in which abnormality zone, if any, the data belongs (e.g. alert or alarm).

Health Assessment (Diagnosis): diagnoses any faults and rates the current health of the equipment or process, considering all state information.

Prognostics Assessment (Prognosis): determines future health states and failure modes based on the current health assessment and projected usage loads on the equipment and/or process, as well as remaining useful life (RUL).

Advisory Generation: provides actionable information regarding maintenance or operational changes required to optimize the life of the process and/or equipment based on diagnostics/prognostics information and available resources.

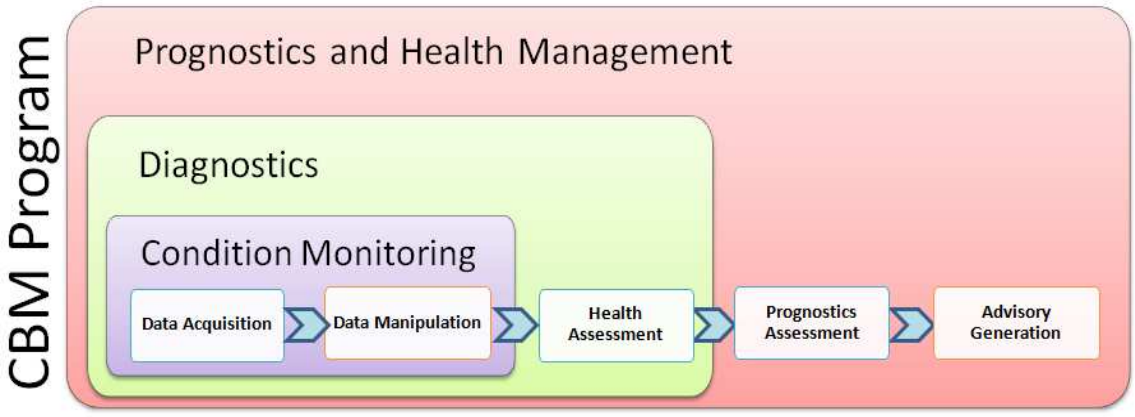

Figure 1.2 Functional layers of CBM

Data Acquisition, Data Manipulation and State Detection layers comprise Condition Monitoring system, and make a foundation of a general CBM program. Prognostic is a general term that describes a process to predicting the remaining useful life (RUL) of a component and system (how, how fast, and to what extent the diagnosed fault will progress) [5] as indicated in Figure 1.3. Currently, CBM is dominantly diagnostic, since machine condition prognosis is relatively new and by its definition has a high level of uncertainty and complexity with many remaining challenges [2].

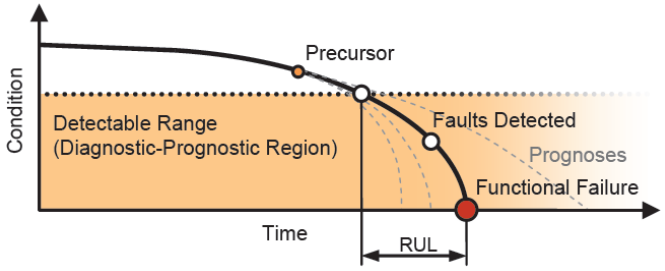

Figure 1.3 Schematic of a component lifetime curve [2].

In this dissertation, we focus our attention to improve the functionality of the CBM layers, State Detection and Health Assessment and Diagnosis, throughout the development of new signal processing techniques and algorithms based on higher-order statistical signal processing, and the implementation of those techniques in condition monitoring of critical rotating components in military helicopter.

1.2 CBM Practice in US Army Rotorcrafts

Over the past decade, great advancements have been made in field of fault detection and health diagnostic of aircraft systems [6]-[11]. The successes to date in implementing this technology in military helicopters have resulted in the large-scale deployment of health monitoring systems such as Health and Usage Monitoring Systems (HUMS) and Vibration Management Enhancement Program (VMEP), which have generated a wide range of benefits from increased safety to reduced maintenance costs [12]-[15].

The US Army and South Carolina Army National Guard (SCARNG) are currently employing the HUMS and VMEP systems to shift the standard time-based maintenance in military aviation toward the innovative CBM practice. VMEP system includes an on-board Modern Signal Processing Unit (MSPU) which continuously monitors the health conditions of crucial aircraft components such as rotor, engines, gearboxes, and drive train using tachometers and accelerometers sensors distributed throughout the helicopter's drive train as shown in Figure 1.4 [13]. The MSPU is currently deployed on AH-64 Apache, UH-60 Blackhawk and CH-47 Chinook fleets [16].

Processed data from the MSPU provides rotorcraft maintainers at the ground-based station with a collection of diagnostic and progressively prognostic vibration-based indicators summarized by Condition Indicators (CIs) or Health Indicators (HIs), which collect several CI metrics. Pre-established and baseline measurements of these typically one-dimensional CI and HI values from existing historical data and testbed verifications under extreme conditions provide rankings for the status of individual aerospace and rotorcraft components with ratings such as "Good," "Caution," and "Exceeded," which in turn provide maintainers of these fleets proactive time-independent condition based maintenance decision making [17].

(a)

(b)

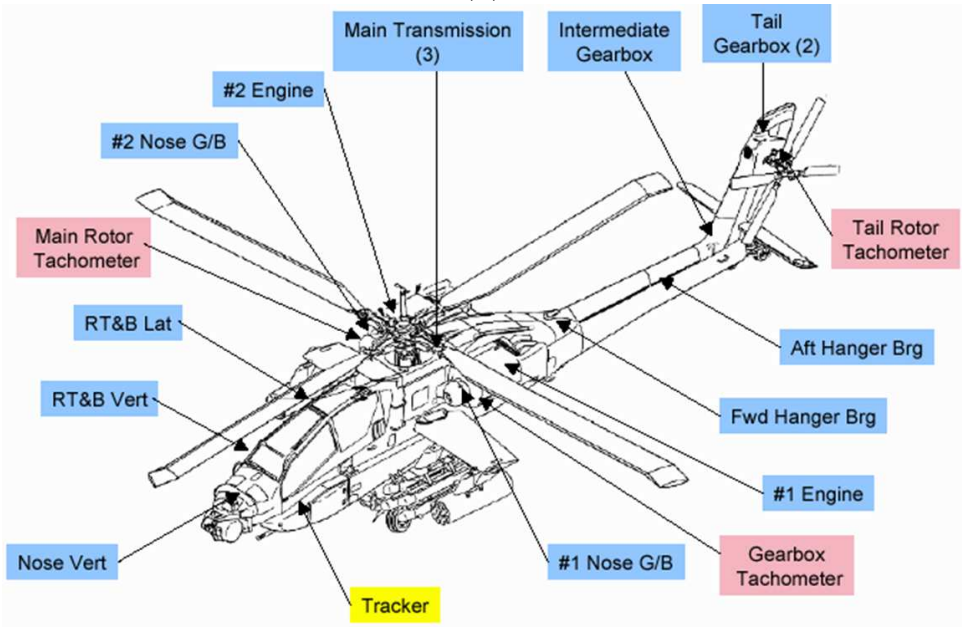

(c)

Figure 1.4 (a) AH-64A helicopter, (b) Sensor locations in an AH-64A monitored by the MSPU, and (c) Exposed-top MSPU unit [13]

1.3 CBM Practice at the University of South Carolina

Since 1998 the University of South Carolina (USC) has been working closely with the South Carolina Army National Guard (SCARNG) in number of important projects that were directed at reducing the Army aviation costs and increasing operational readiness through the implementation of CBM program [18], [19]. Research emphasis has been to collect and analyze data and to formulate requirements assisting in the transition toward CBM. The research program at USC seeks to deliver tangible results which directly contribute to CBM efforts and objectives such as: link and integrate maintenance management data with on- board sensor data and test metrics, quantify and evaluate the importance of each data field relative to CBM, understand the physics and the root causes of faults of components, subsystems and systems, explore the development of models for early detection of incipient faults, develop models to predict remaining life of components, subsystems and systems.

These efforts expanded into a fully matured CBM research center within the USC department of mechanical engineering, which hosts several aircraft component test stands in support of current US Army CBM objectives. The CBM center at the University of South Carolina has a complete AH-64D (Apache helicopter) tail rotor drive train (TRDT) test stand for on-site data collection and analysis, as shown in Figure 1.5-(b). The TRDT test stand emulates the complete tail rotor drive train from the main transmission tail rotor takeoff to the tail rotor swash plate assembly, as shown in Figure 1.5-(a).

All drive train parts on the test stand are actual aircraft hardware. The prime mover for the drive train is an 800hp AC induction motor controlled by variable frequency drive. An absorption motor of matching rating is used to simulate the torque loads that would be applied by the tail rotor blade and it is controlled by another variable frequency drive. The input and the output motors work in dynamometric configuration to save energy.

(a)

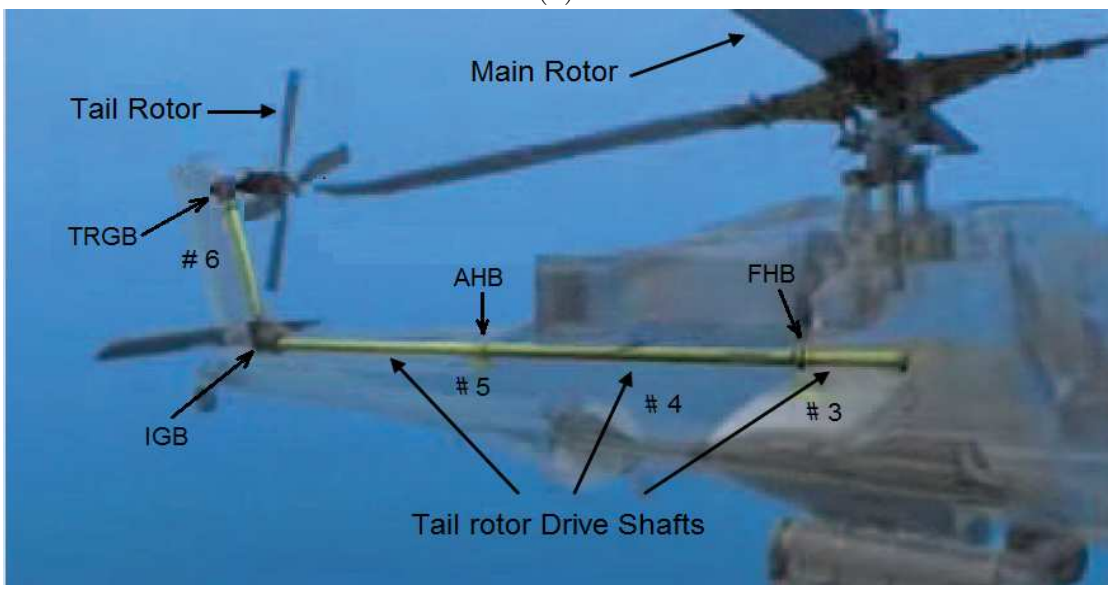

(b)

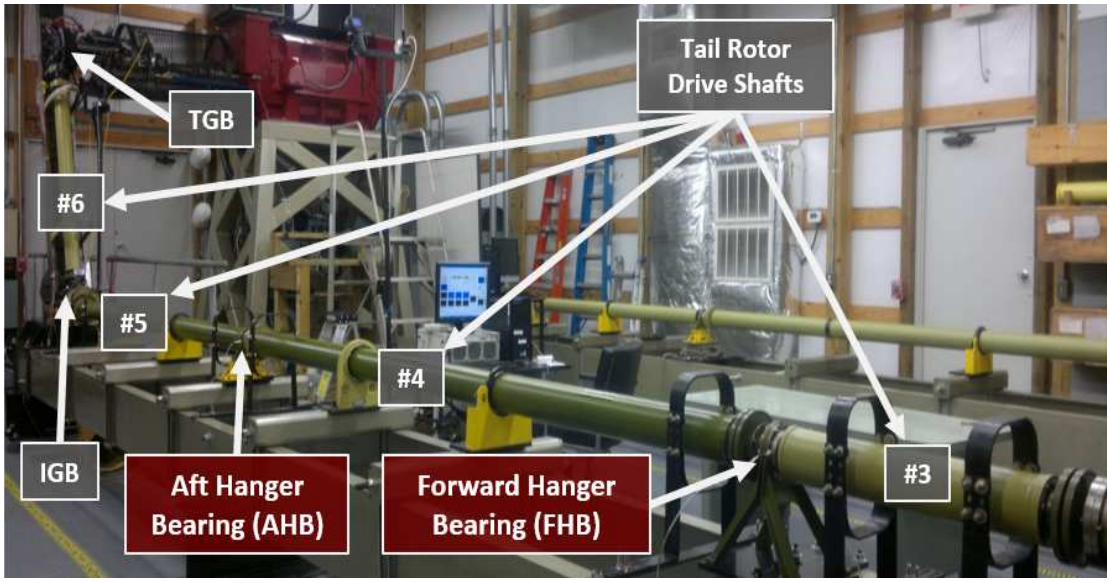

Figure 1.5 (a) Actual TRDT location on AH-64D, and (b) TRDT test stand at USC

The structure, instrumentation, data acquisition systems, and supporting hardware are in accordance with military standards. The signals being collected during the operational run of the apparatus include vibration data measured by the accelerometers, temperature measured via thermocouples, and speed and torque measurements. The measurement devices are placed at the forward (FHB) and afterward (AHB) hanger bearings and two gearboxes as shown in Figure 1.5-(b).

In this dissertation, we use vibration data collected from different locations in the TRDT test stand in order to assess health conditions of rotating mechanical components such as drive shafts, gearboxes, and hanger bearings under accelerated conditioning experiments.

1.4 Motivations

As discussed in the previous section, condition monitoring of critical components in the aircraft is achieved through processing variety of time-varying signals (waveforms) collected using sensors attached to those critical components such as vibration, acoustic, and temperatures. These signals are the appearance of the operation and wear of the components. By analyzing these characteristics signatures, we can diagnose the current status of the components.

The vibration signals are the most common and popular waveform data used in condition monitoring of rotating and reciprocating components [20]-[25]. Collected vibration data is analyzed using different signal processing techniques to extract features that are used to diagnose current conditions, or used in prognostic models to estimate the remaining useful life of a component. For example, time-domain analysis is directly based on the time waveform itself (e.g., [26], [27], [28]). Traditional time-domain analysis calculates characteristic features from time waveform signals as descriptive statistics such as mean, peak, peak- to-peak interval, standard deviation, crest factor, root mean square, skewness, kurtosis, etc. These features are usually

called time-domain features. Time-domain analysis provides cheap option for monitoring simple machines. However, in the case of complex system composed of many rotating components with different frequencies, time-domain analysis has very limited diagnostic capabilities.

Frequency-domain analysis is based on the transformed signal in frequency domain by mean of Fourier transform. Spectral analysis is the most widely used conventional analysis technique for feature extraction from vibration data [1]. The advantage of frequency-domain analysis over time-domain analysis is its ability to easily identify and isolate certain frequency components of interest and link it to a particular machine component. Vibration-monitoring using spectrum analysis is done by either looking at the whole spectrum or looking closely at certain frequency components of interest and thus extract features from the signal (e.g., [29], [30], [31]).

The most commonly used tool in spectrum analysis is auto-power spectrum which has the dimension of mean square values/Hz and indicates how the mean square value is distributed over frequency. Auto-power spectrum is the Fourier transform of the well known auto-correlation function which is second order statistics, as will be discussed in Chapter 2.

Unfortunately, conventional auto- and cross-power spectra have limited performance in detecting higher order relationship between frequencies inside the signal spectrum. For example, when the system under study exhibit some nonlinearities, various spectral components interact (or, "mix") with one another to form new combinations of "sum" and "difference" frequencies, as indicated by trigonometric identity in equation (1.1).

$$\begin{aligned}\cos(2\pi f_1 t + \theta_1) \times \cos(2\pi f_2 t + \theta_2) = \; & \tfrac{1}{2}[\cos(2\pi(f_1 + f_2)t + (\theta_1 + \theta_2)) \\ & + \cos(2\pi(f_1 - f_2)t + (\theta_1 - \theta_2)] \end{aligned} \tag{1.1}$$

This frequency mix effect due to nonlinearities in the system is depicted in Figure 1.6. In such a case, higher order correlation, and their Fourier transforms, Higher Order Spectra (HOS), are used to characterize nonlinearities in the system and signals, as will be introduced in Chapter 2. Higher-order correlation and higher-order spectra will be progressively higher-order dimensional functions of time and frequency, respectively. This is why polyspectra is sometimes used as synonym of higher-order spectra.

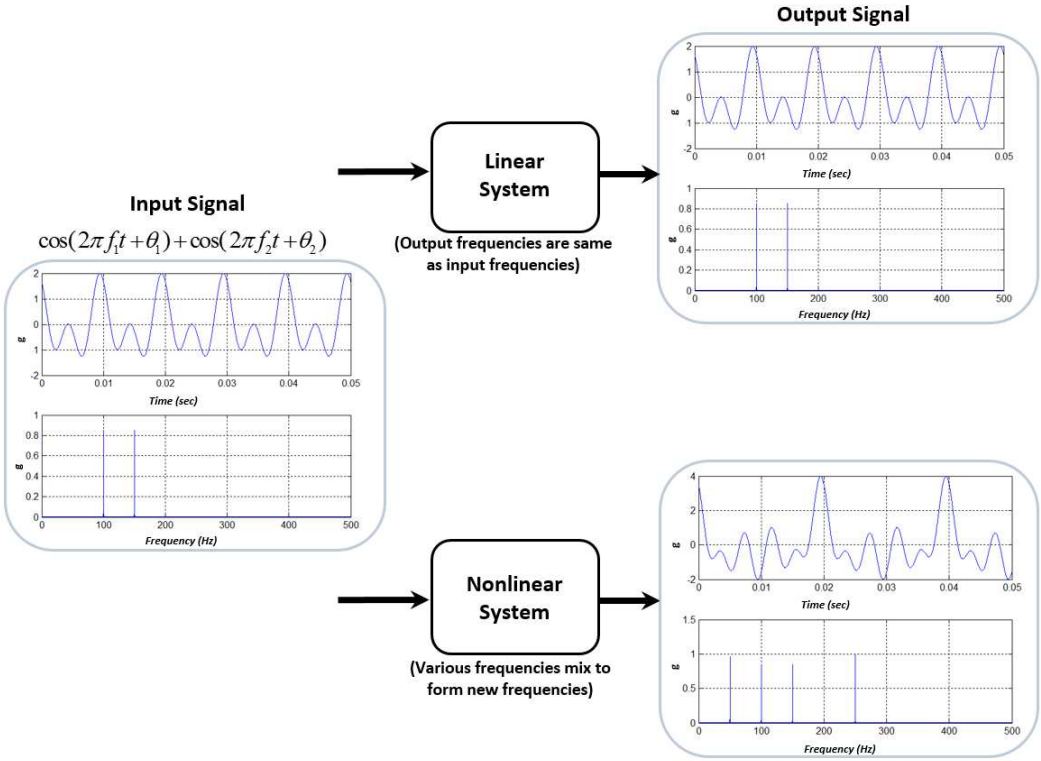

Figure 1.6 Frequency mix effect due to nonlinearities in the system

Advantages of using higher-order statistics also include:

- **Preservation of phase information** in the form of a phase difference. Note that the auto-power spectrum does not preserve phase information.
- **Detection and quantification of phase-coupling** or phase-coherence between various frequency components satisfying specific frequency selection rule.

Such phase-coupling may be introduced by nonlinear processes.

- **Insensitivity to additive and independent Gaussian noise**. For example, the third-order spectrum, bispectrum, is ideally zero for Gaussian random process.

Motivated by several advantages of the higher-order statistics mentioned above, this dissertation presents theory and applications of signal processing techniques based on higher-order statistics for condition based maintenance of critical components in the AH-64D military-helicopter tail rotor drive train system. Our objectives can be summarized as follows:

- Extracting more information from the same collected vibration data using higher-order statistics, without the need of adding more hardware.
- Developing more accurate diagnostic models by taking into consideration information from higher-order spectra.
- Understanding root causes of certain frequencies appearing in the vibration spectrum due to nonlinear system behavior and relate those frequencies to the correct fault in the mechanical system.
- Developing an easy-to-use higher-order statistics' tools for CBM applications.

1.5 Organization of the Dissertation

The remainder of this dissertation is organized as follows: In Chapter 2, we introduce the subject of higher order statistical signal processing in order to provide a bridge to following chapters and lay out mathematical foundations for signal processing algorithms that will be developed later in this dissertation.

In Chapter 3, the cross-bispectrum is used to investigate and model vibrations' spectral interaction due to quadratic nonlinearities in faulted drive shafts in an AH-

64D helicopter tail-rotor drive-train. Based on cross-bispectrum, quadratic nonlinear transfer function is presented to model second order nonlinearity in the drive shaft running between the two hanger bearings. Then, nonlinearity coupling coefficient between frequency harmonics of the rotating shafts is used as condition metric to diagnose different seeded shaft faults compared to baseline case, namely: 1)- shaft misalignment, 2)- shaft imbalance, and 3)- combination of shaft misalignment and imbalance.

In Chapter 4, we develop a new concept of Quadratic-Nonlinearity Power-Index spectrum, $QNLPI(f)$, that can be used in signal detection and classification, based on bicoherence spectrum. The proposed $QNLPI(f)$ is derived as a projection of the three-dimensional bicoherence spectrum into two-dimensional spectrum that quantitatively describes how much of the mean square power at certain frequency f is generated due to nonlinear quadratic interaction between different frequency components. The quadratic-nonlinear power spectral density $P_{QNL}(f)$ and percentage of quadratic nonlinear power $PQNLP$ are also introduced based on the $QNLPI(f)$. Concept of the proposed indices and their computational considerations are discussed first using computer generated data, and then applied to real-world vibration data to assess health conditions of different rotating components in the drive train including different combinations of drive-shaft and gearbox faults. The $QNLPI(f)$ spectrum enables us to gain more details about nonlinear harmonic generation patterns that can be used to distinguish between different cases of mechanical faults, which in turn helps to gaining more diagnostic/prognostic capabilities.

In Chapter 5, the behavior of the helicopter's tail-rotor drive-train under more than one simultaneous fault is studied using the proposed signal analysis techniques. In the presence of drive-shaft faults, shaft harmonics dominate the power spectra of the vibration signals collected form faulted hanger-bearing making it hard to detect bearing's faults. Also, spectral interaction between different fault frequencies leads

to unexpected frequencies to appear in the vibration spectrum which can not be explained using conventional power spectral analysis. However, bispectral analysis tools not only detect the bearing's faults in this extreme case of multi-faulted components, but also are able relate all frequencies to their root causes and successfully links the signal processing to the physics of the underlying faults.

Finally, conclusion of this dissertation is presented in Chapter 6.

Chapter 2

Higher Order Statistical (HOS) Analysis

In this chapter, we introduce the subject of higher order statistical signal processing in order to provide a bridge to following chapters and lay out mathematical foundations for signal processing algorithms that will be developed later in this dissertation. We initiate our discussion by considering vibration data as realization of random process that can be used to characterize unknown conditions of rotating systems. Just as random variables are characterized by certain expected values (moments) or averages such as mean and variance, random processes are also characterized by their mean value, correlation function, and various higher order correlation functions, or moment functions. Alternatively, random processes may be characterized by the Fourier transform of the various order correlation functions which are known as higher order spectra, as will be discussed in the following sections.

2.1 Higher-Order Auto-Moments and Stationary Fluctuations

In probability theory and statistics, n-order central moment of a random variable X is calculated as the expected value of integer power, n, of the the random variable X around its mean, as follows:

$$m_x^{(n)} = E\{(X - E\{X\})^n\} = \int_{-\infty}^{\infty} (x - E\{X\})^n \; f_X(x)dx \tag{2.1}$$

where $E\{.\}$ denotes the expected value operator, superscript $^{(n)}$ describes the order of the central moment, and $f_X(x)$ is the probability density function (pdf) of the

random variable X. Thus, $m_x^{(1)} = 0$ = the mean value, $m_x^{(2)}$ = mean square value, $m_x^{(3)}$ = mean cube value; and so on. Central moments are used in preference to ordinary moments, computed in terms of deviations from zero instead of from the mean, because the higher-order central moments relate only to the spread and shape of the distribution, rather than also to its location.

Higher order statistical signal processing involve generalization of various order moments in the case of random variable to moment functions (i.e., correlation functions) in the case of random process. Therefore, it is mathematically desired to assume that the random process has zero mean for computation convenience, which what we adopt through out the rest of this dissertation. In the practical cases when we will be dealing with real vibration data from monitored mechanical components, the mean of the signal is first computed and subtracted from the signal.

Based on the mathematical foundations of higher order statistical signal processing in [32], various order correlation functions can be calculated for the random process as follows:

$$\mu_x = E\{x(t)\} = 0 \text{ (or, a constant)} \tag{2.2}$$

$$R_{xx}(\tau) = E\{x^*(t)x(t+\tau)\} \tag{2.3}$$

$$R_{xxx}(\tau_1, \tau_2) = E\{x^*(t)x(t+\tau_1)x(t+\tau_2)\} \tag{2.4}$$

$$R_{xx...x}(\tau_1, \tau_2, ..., \tau_n) = E\{x^*(t)x(t+\tau_1)x(t+\tau_2)...x(t+\tau_n)\} \tag{2.5}$$

where $E\{.\}$ denotes the expected value operator and the superscript asterisk (*) denotes complex conjugate. It is worthwhile to note here that the second-order cor-

relation function, $R_{xx}(\tau)$, in equation (2.3) is the familiar auto-correlation function. The third-order correlation function, $R_{xxx}(\tau_1, \tau_2)$, is often called *bicorrelation* function, presumably because it is a function of two time variables. The fourth-order correlation function, $R_{xxxx}(\tau_1, \tau_2, \tau_3)$, is often called *tricorrelation*, and so on.

Generally, in the non-stationary case, the correlation function will be a function of time t, as well as the time differences, $\tau_1, \tau_2, ..., \tau_n$ as follows:

$$R_{xx...x}(t, \tau_1, \tau_2, ..., \tau_n) = E\{x^*(t)x(t+\tau_1)x(t+\tau_2)...x(t+\tau_n)\} \tag{2.6}$$

Zero-mean fluctuation data is considered strongly stationary (strict sense stationary) to order n if the mean and the various order correlation functions are functions of time differences only, i.e. $\tau_1, \tau_2, ..., \tau_n$. In other words, neither the mean nor the correlation functions depend on absolute time t as indicated in equations (2.2)-(2.5). In the case of analyzing linear signals and systems, it is enough to have only (2.2)-(2.3) satisfied. This case is called weakly-stationary (wide-sense stationary) signal. For three-wave interaction in quadratically nonlinear system as will be discussed later, random signal is assumed to be stationary to third order (equations (2.2)-(2.4)).

2.2 Auto-Correlation and Auto-Power Spectrum

In signal processing, the auto-correlation function $R_{xx}(\tau)$ for a wide-sense stationary signal $x(t)$ is defined as

$$R_{xx}(\tau) = x(t) \star x(t) = \int_{-\infty}^{\infty} x^*(t)x(t+\tau)dt \tag{2.7}$$

where the operation of correlation is indicated by a five-pointed star ($\star$). Auto-correlation $R_{xx}(\tau)$ is a measure of similarity (statistical dependence) between a signal $x(t)$ and time-shifted version $x(t+\tau)$. For the vibration signals collected from CBM test bed, it is not possible (from experimental point of view) to access all pos-

sible realizations of $x(t)$. Therefore, the auto-correlation in this case is statistically estimated based on a finite number of realizations as indicated in (2.3).

The Wiener-Khinchin theorem states that auto-power spectrum $P_{xx}(f)$ is the Fourier transform of the auto-correlation $R_{xx}(\tau)$ [33], [34], and can be estimated by

$$P_{xx}(f) = E\{X^*(f)X(f)\} = E\{|X(f)|^2\} \tag{2.8}$$

where $X(f)$ is the Fourier transform of $x(t)$ described by the following equation:

$$X(f) = \int_{-\infty}^{\infty} x(t)e^{-j2\pi ft}dt \tag{2.9}$$

The auto-power spectrum, $P_{xx}(f)$, in equation (2.8) has the dimensions of mean square values/Hz and it indicates how the mean square value is distributed over frequency. Thus, in case of $x(t)$ is measuring voltage signal, $[P_{xx}(f)]$ is $(volts)^2/Hz$. Moreover, wide-sense stationarity implies that, if $x(t)$ consists of finite number of complex sinusoids (as a result of Fourier transform decomposition in equation (2.9)), corresponding frequency domain components of different frequencies are uncorrelated, that the mean square value of $x(t)$ is equal to the sum of the mean square values of each frequency component.

2.3 Auto-Bicorrelation and Auto-Bispectrum

The third order auto-correlation function is known as auto-bicorrelation $R_{xxx}(\tau_1, \tau_2)$, and its two-dimensional Fourier transform is known as auto-bispectrum $B_{xxx}(f_1, f_2)$. In common practice, when bispectrum is mentioned, it is meant to be the auto-bispectrum. $R_{xxx}(\tau_1, \tau_2)$ and $B_{xxx}(f_1, f_2)$ for zero-mean strongly stationary random

signal $x(t)$ are defined in (2.10) and (2.11) respectively [35].

$$R_{xxx}(\tau_1, \tau_2) = E\{x^*(t)x(t+\tau_1)x(t+\tau_2)\} \tag{2.10}$$

$$B_{xxx}(f_1, f_2) = E\{X(f_1)X(f_2)X^*(f_3 = f_1 + f_2)\} \tag{2.11}$$

Bispectral analysis is a powerful signal processing technique in detecting second-order nonlinearity in signals and systems. When various frequency components of the vibration signal interact with one another due to quadratic nonlinearity, new combinations of frequencies are generated at both the sum and the difference of the interacting frequencies, as indicated in equation (2.12). Those frequency components are phase coupled to the primary interacted frequencies. Bispectrum uses this phase coupling signature between frequency components to detect second-order nonlinearities [36].

$$\begin{aligned}\cos(2\pi f_1 t + \theta_1) \times \cos(2\pi f_2 t + \theta_2) = \; & \tfrac{1}{2}[\cos(2\pi(f_1 + f_2)t + (\theta_1 + \theta_2)) \\ & + \cos(2\pi(f_1 - f_2)t + (\theta_1 - \theta_2)]\end{aligned} \tag{2.12}$$

The definition of the bispectrum in (2.11) shows how the bispectrum measures the statistical dependence between three waves. That is, $B_{xxx}(f_1, f_2)$ will be zero unless the following two conditions are met:

1. Waves must be present at the frequencies f_1, f_2, and $f_1 + f_2$. That is, $X(f_1)$, $X(f_2)$, and $X(f_1 + f_2)$ must be non-zero.

2. A phase coherence must be present between the three frequencies f_1, f_2, and $f_1 + f_2$.

If waves present at f_1, f_2, and f_1+f_2 are spontaneously excited independent waves, each wave will be characterized by statistical independent random phase. Thus, the sum phase of the three spectral components will be randomly distributed over $(-\pi, \pi)$. When a statistical averaging denoted by the expectation operator is carried out, the bispectrum will vanish due to the random phase mixing effect. On the other hand, if the three spectral components are nonlinearly coupled to each other, the total phase of three waves will not be random at all, although phases of each wave are randomly changing for each realization. Consequently, the statistical averaging will not lead to a zero value of the bispectrum.

The auto-bispectrum $B_{xxx}(f_1, f_2)$ is a true spectral density function indicates how the mean cube value of $x(t)$ is distributed over a two-dimensional frequency plane. Thus, in case of $x(t)$ is measuring voltage signal, $[B_{xxx}(f_1, f_2)]$ is $(volts)^3 / Hz^2$.

2.4 Higher-Order Cross-Moments

Higher-order moment functions can also be defined for two real random processes $x(t)$ and $y(t)$. The quantities $x(t)$ and $y(t)$ may, for example, represent the random excitation and response of a nonlinear system. In this case, the cross-moment functions are given as follows [32]:

$$R_{yx}(\tau) = E\{y^*(t)x(t+\tau)\} \tag{2.13}$$

$$R_{yxx}(\tau_1, \tau_2) = E\{y^*(t)x(t+\tau_1)x(t+\tau_2)\} \tag{2.14}$$

$$R_{yx\ldots x}(\tau_1, \tau_2, ..., \tau_n) = E\{y^*(t)x(t+\tau_1)x(t+\tau_2)...x(t+\tau_n)\} \tag{2.15}$$

Once again, the above equations (2.13)-(2.15) assume stationarity and zero-mean. The second-order cross-moment function, $R_{yx}(\tau)$, in equation (2.13) is the familiar cross-correlation function, while $R_{yxx}(\tau_1, \tau_2)$ and $R_{yxxx}(\tau_1, \tau_2, \tau_3)$ are referred to as *cross-bicorrelation* function and *cross-tricorrelation* function, respectively. The cross-bicorrelation and cross-tricorrelation are obviously higher-order moment functions, and their Fourier transforms, the cross-bispectrum and cross-trispectrum are extremely powerful concepts that can be used to analyze and interpret data associated with nonlinear phenomena such as nonlinear wave interactions, as we will see in the following chapters of this dissertation.

2.5 Cross-Correlation and Cross-Power Spectrum

Cross-power spectrum $C_{yx}(f)$ given in equation (2.16) is the Fourier transform of the cross-correlation function $R_{yx}(f)$ in equation (2.13). Cross-correlation function $R_{yx}(f)$ and cross-power spectrum $C_{yx}(f)$ have been fruitfully utilized in many fields of science and engineering to identify and quantify statistical linear relationships between two fluctuating quantities $x(t)$ and $y(t)$.

$$C_{yx}(f) = E\{Y^*(f)X(f)\} \tag{2.16}$$

Cross-power spectrum can be represented in terms of amplitude spectrum $|C_{yx}(f)|$ and phase spectrum $\theta_{yx}(f)$. That is,

$$C_{yx}(f) = |C_{yx}(f)|\ e^{\theta_{yx}(f)} \tag{2.17}$$

The phase of the cross-power spectrum preserves phase information in the form of a phase difference. This is perhaps the single most important property of the cross-power spectrum, and it is employed in too many applications.

2.6 Cross-Bicorrelation and Cross-Bispectrum

Cross-bispectrum $S_{xxy}(f_1, f_2)$ is the two-dimensional Fourier transform of the third order cross-correlation function $R_{yxx}(\tau_1, \tau_2)$, and it is estimated by the following equation,

$$S_{xxy}(f_1, f_2) = E\{X(f_1)X(f_2)Y^*(f_3 = f_1 + f_2)\} \tag{2.18}$$

The cross-bispectrum is quite similar to the auto-bispectrum except it may be used to detect and quantify the nonlinear interaction of two spectral components in one fluctuation record $x(t)$. The two spectral components (which represent complex amplitude of waves or oscillations) result in the appearance of a sum or difference frequency wave in second fluctuation record $y(t)$, as illustrated before in equation (2.12). Therefore, the cross-bispectrum is a key concept in modelling nonlinear systems and quantitatively evaluating complex coupling coefficient, as will be done in Chapter 3 of this dissertation.

2.7 Symmetry Properties and Region of Computation for Auto- and Cross- Bispectra

It is well known that if $x(t)$ is real, magnitude of the Fourier transform is even symmetric and its phase is odd symmetric arround the zero, that is,

$$X(-f) = X^*(f) \tag{2.19}$$

Applying the symmetry property in (2.19) to the case of $x(t)$ and $y(t)$ are real, the auto-power spectrum $P_{xx}(f)$ and the cross-power spectrum $C_{yx}(f)$ also satisfy

certain symmetry properties indicated as follows:

$$P_{xx}(-f) = P_{xx}(f) \tag{2.20}$$

$$C_{yx}(-f) = C^*_{yx}(f) \tag{2.21}$$

Consequently, one needs to calculate auto- and cross-power spectra for positive frequency only.

In a similar fashion, auto- and cross- bispectra possess certain symmetry properties in the two-dimensional bi-frequency planes. As a result of the symmetries, it is not necessary to calculate these spectra over the entire bi-frequency plane. Therefore, substituting the symmetry property from (2.19) into the auto-bispectrum equation (2.11), one can easily prove that the bispectrum possesses the following symmetry properties:

$$B_{xxx}(-f_1, -f_2) = B^*_{xxx}(f_1, f_2) \qquad \text{(symmetry property I)} \tag{2.22}$$

$$B_{xxx}(f_2, f_1) = B_{xxx}(f_1, f_2) \qquad \text{(symmetry property II)} \tag{2.23}$$

$$B_{xxx}(-f_2, -f_1) = B^*_{xxx}(f_1, f_2) \qquad \text{(symmetry property III)} \tag{2.24}$$

$$B_{xxx}(f_1, -f_2) = B^*_{xxx}(f_1 - f_2, f_2) \qquad \text{(symmetry property IV)} \tag{2.25}$$

The above symmetry properties imply that the auto-bispectrum is enough to be computed only for the octant labeled "Σ" in Figure 2.1(a). The bispectrum of all other octants are related to bispectrum in octant "Σ" using one or two properties in

equations (2.22)-(2.25), as illustrated in Figure 2.1(a). In fact, auto-bispectrum will be estimated digitally. The sampling theory implies that all f_1, f_2 and $f_3 = f_1 + f_2$ must be less than or equal to $\frac{f_s}{2}$, where f_s is the sampling frequency. Therefore, when auto-bispectrum is digitally computed, it will be plotted within the triangular region defined by the lines $f_2 = 0$, $f_2 = f_1$, and $f_2 = \frac{f_s}{2} - f_1$, as depicted in Figure 2.1(b).

The cross-bispectrum possesses the same first three symmetry properties possessed by the auto-bispectrum described above. That is, for $x(t)$ and $y(t)$ real,

$$S_{xxy}(-f_1, -f_2) = S^*_{xxy}(f_1, f_2) \qquad \text{(symmetry property I)} \tag{2.26}$$

$$S_{xxy}(f_2, f_1) = S_{xxy}(f_1, f_2) \qquad \text{(symmetry property II)} \tag{2.27}$$

$$S_{xxy}(-f_2, -f_1) = S^*_{xxy}(f_1, f_2) \qquad \text{(symmetry property III)} \tag{2.28}$$

It is important to note that symmetry property IV for the auto-bispectrum does not hold true for the cross-bispectrum. Therefore, it is necessary to compute the cross-bispectrum for both the sum region represented by octant "Σ" and the difference region represented by octant "Δ", as illustrated in Figure 2.2(a). Again, since the cross-bispectrum is to be implemented digitally, sampling theory implies that $f_1 + f_2 \leq \frac{f_s}{2}$ and $f_2 \leq \frac{f_s}{2}$. These boundaries are indicated in Figure 2.2(b).

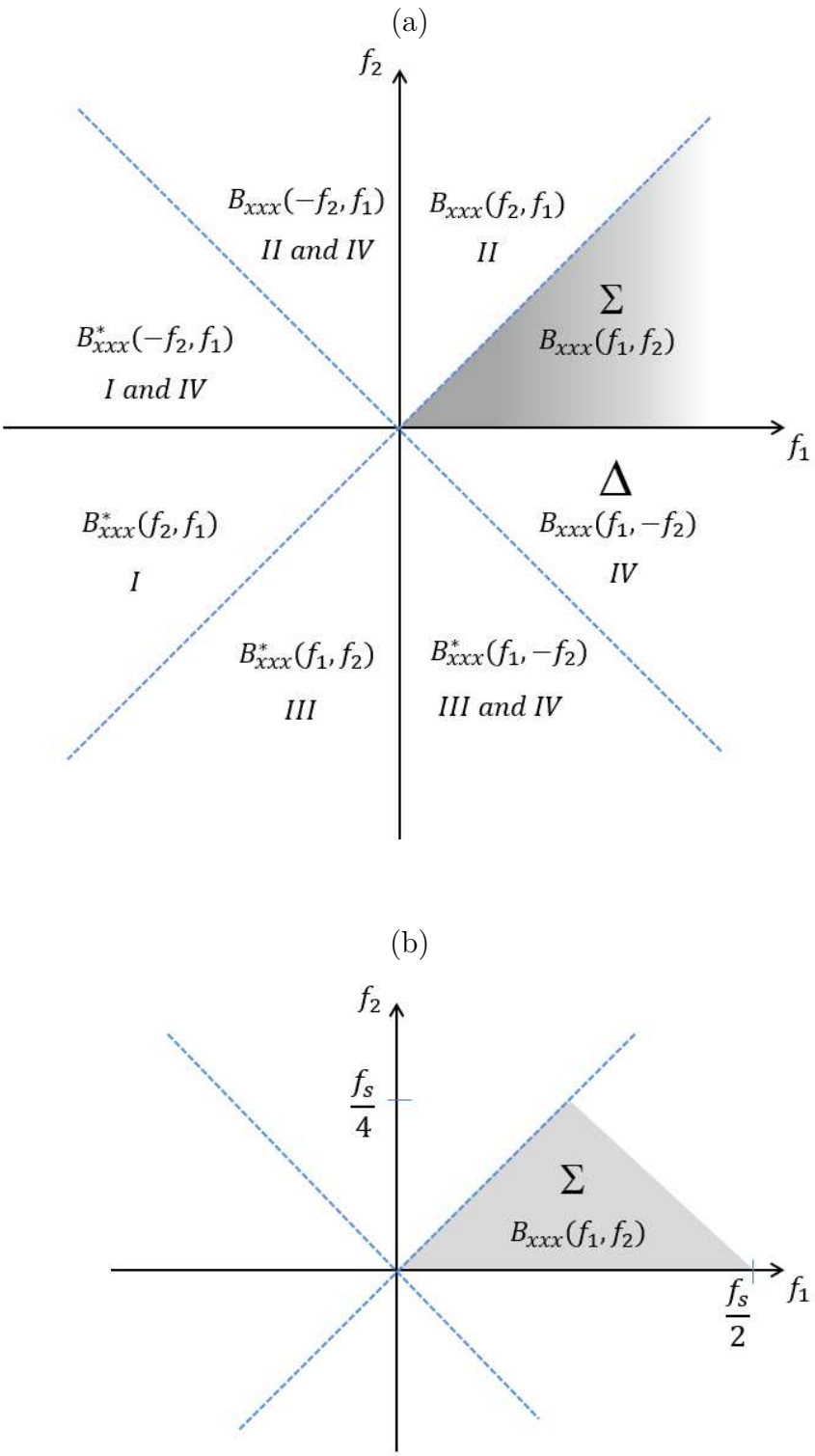

Figure 2.1 Symmetric regions and region of computation for (a) continuous auto-bispectrum (b) digitally implemented auto-bispectrum

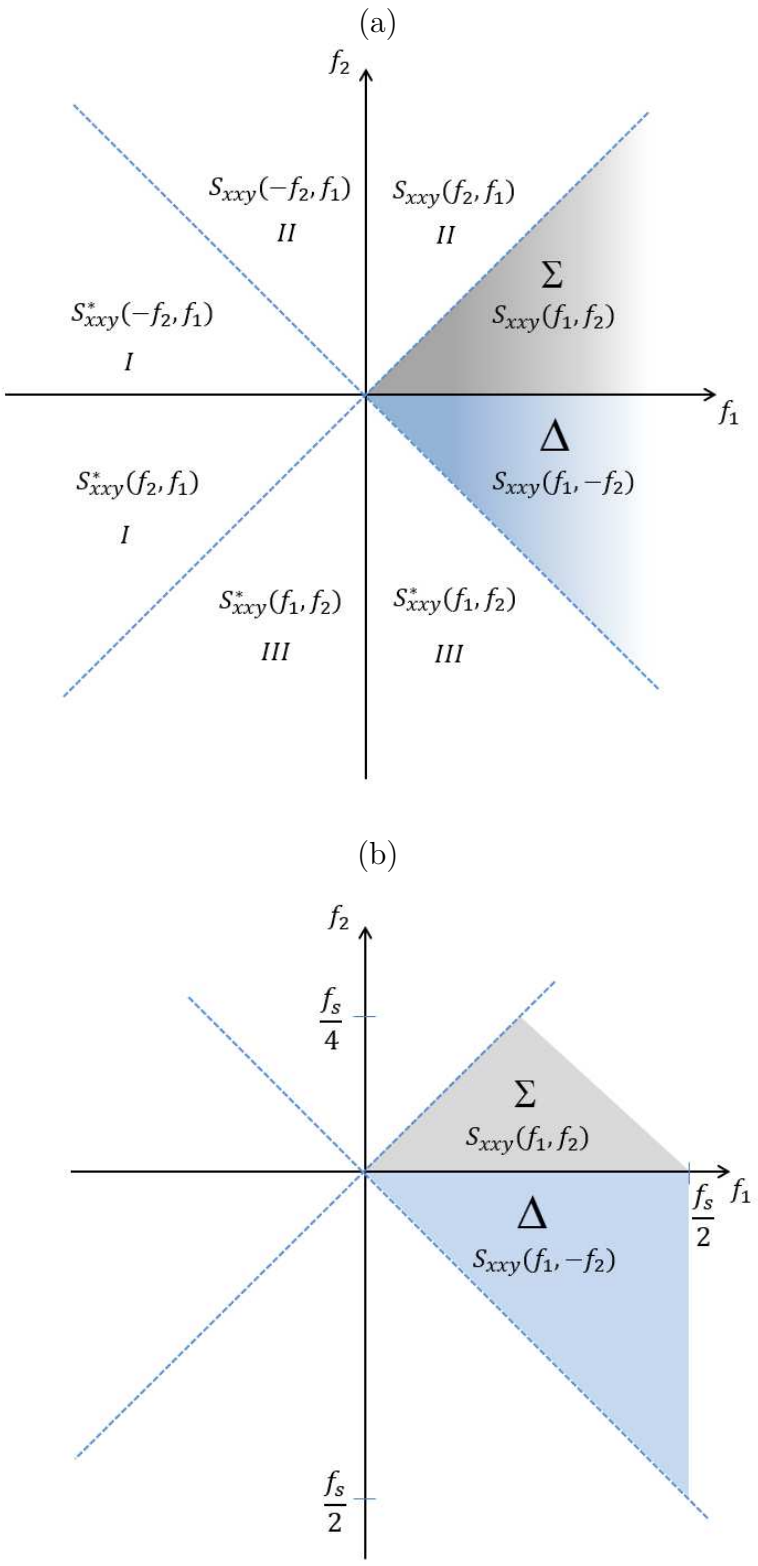

Figure 2.2 Symmetric regions and region of computation for (a) continuous cross-bispectrum (b) digitally implemented cross-bispectrum

2.8 Digital Estimation of Auto- and Cross- Bispectra

Throughout the course of this dissertation, we will be analyzing vibration data using different order of spectral analysis discussed above in order to assess health conditions of rotating mechanical components. Since vibration data is collected, stored, and processed in digital form using computer, it is important to make that link to the discrete signal processing.

Our goal in this section is to outline the procedure of how auto- and cross-bispectra are estimated directly from the Discrete Fourier Transform (DFT) of sampled versions of $x(t)$ and $y(t)$. The expected value operator, $E\{.\}$, is statistically estimated using average over ensemble of M realization of the signals under study. Assuming that M realizations of the vibration signals $x(t)$ and $y(t)$ are available and the duration of each realization is T seconds. If the sampling frequency is to be $f_s = 1/t_s$, number of samples in each realization will be $N = T/t_s$. To compute the auto- or cross-bispectrum, the following steps should be carried out.

1. Compute the mean value of each realization,

$$\begin{aligned} \overline{x^{(k)}}[n] &= \frac{1}{N}\sum_{n=0}^{N-1} x^{(k)}[n] \\ \overline{y^{(k)}}[n] &= \frac{1}{N}\sum_{n=0}^{N-1} y^{(k)}[n] \end{aligned} \tag{2.29}$$

   and subtract the mean value. It is assumed in the following steps that $x^{(k)}[n]$ and $y^{(k)}[n]$ are zero-mean where the superscript $^{(k)}$ represent the k^{th} realization of the signal.

2. Compute the DFT for each realization,

$$X^{(k)}[l] = \frac{1}{N}\sum_{n=0}^{N-1} x^{(k)}[n]\ e^{-j2\pi ln/N}$$
$$Y^{(k)}[l] = \frac{1}{N}\sum_{n=0}^{N-1} y^{(k)}[n]\ e^{-j2\pi ln/N} \tag{2.30}$$

3. Compute the sample auto- or cross-bispectrum for each realization,

$$B^{(k)}_{xxx}[l_1, l_2] = X^{(k)*}[l_1 + l_2]\ X^{(k)}[l_1]\ X^{(k)}[l_2]$$
$$S^{(k)}_{xxy}[l_1, l_2] = Y^{(k)*}[l_1 + l_2]\ X^{(k)}[l_1]\ X^{(k)}[l_2] \tag{2.31}$$

4. Estimate average the samples auto- or cross-bispectrum over the M realization to yield the final estimator,

$$B_{xxx}[l_1, l_2] = \frac{1}{M}\sum_{k=1}^{M} B^{(k)}_{xxx}[l_1, l_2]$$
$$S_{xxy}[l_1, l_2] = \frac{1}{M}\sum_{k=1}^{M} S^{(k)}_{xxy}[l_1, l_2] \tag{2.32}$$

Note that $B_{xxx}[l_1, l_2]$ needs to be computed only in the sum "Σ" region indicated in Figure 2.1(b), while $S_{xxy}[l_1, l_2]$ is computed for both the sum "Σ" and difference "Δ" regions as indicated in Figure 2.2(b).

Chapter 3

Quadratic-Nonlinearity Coupling and its Application in Health Assessment of Rotating Drive Shafts

In this chapter, the cross-bispectrum is used to investigate and model vibrations' spectral interaction due to quadratic nonlinearities in faulted drive shafts in an AH-64D helicopter tail-rotor drive-train. Based on cross-bispectrum, quadratic-nonlinear coupling metric, $A_{QC}(l,k)$, is proposed to model second-order nonlinear behaviour of the drive shafts, as will be discussed in section 3.3. The proposed quadratic-nonlinearity metric shows better capabilities in distinguishing different shaft settings than the conventional linear coupling based on cross-power spectrum, as will be discussed in section 3.5.

3.1 Introduction

Tail rotor drive train is a critical section of the aircraft in that it consists of transmission system with a single load path to transfer the power from the main rotor to the tail rotor via a system of drive shafts and gearboxes [37]. Failure of any one of these series connected components decreases the chances of landing the aircraft safely. Without the input from the tail rotor system, the ability to control and counter the torque produced by the main rotor blades does not exist. Thus, condition monitoring systems, such as HUMS and VMEP discussed in section 1.2, keep maintenance mechanics aware of the health conditions of their aircraft by continuously calculating

condition indicators using vibration data collected from those critical components during the flight [19]-[22].

Current practice in health monitoring of the tail-rotor drive-shafts involves monitoring spectral peaks from two vibration signals simultaneously collected at the two ends of each shaft [16]. Spectral peaks at the first-three shaft harmonics ($1R$, $2R$, and $3R$) are typically used as condition indicators of the shaft faults such as misalignment and imbalance [38], [39]. In order to calculate those condition indicators, either auto-power spectrum is averaged between the two vibration signals at one particular frequency (for example, $2R$), or cross-power spectrum between the two vibration signals is calculated at this particular frequency. Auto- and cross-power spectra are Fourier transforms of auto- and cross-correlation functions, respectively. Hence, one can think about cross-power spectrum as a tool to investigate linear correlation between two vibration signals in terms of spectral frequencies.

However, higher order correlations among vibration spectral components can provide valuable information about the health of rotating component. Moreover, this information comes with no additional cost in terms of adding more hardware (sensors, wiring, ect.) since all what we need is further processing of the same collected vibration data [40].

In this chapter, we utilize the cross-bispectrum as HOS tool to investigate and model quadratic nonlinear relationship between two vibration signals simultaneously collected at the forward and afterward hanger bearing positions in an AH-64D helicopter tail rotor drive train. Vibration data are gathered from dedicated condition based maintenance experimental helicopter drive-train simulating different shaft conditions, namely; baseline case, shaft misalignment, shaft imbalance, and combination of misalignment and imbalance. For each of these settings, the experiment is repeated three times using different hanger bearing articles, making a grand total of twelve experiment runs, as will be discussed in section 3.4.

Based on cross-bispectrum, quadratic-nonlinearity coupling coefficient, A_{QC}, is proposed to quantitatively describe second order nonlinearities in the drive shaft. Then, $A_{QC}(1R, 1R)$, is used as a condition metric to distinguish between the different shaft faults compared to baseline case. Magnitude response of the proposed quadratic-nonlinearity metric, $A_{QC}(1R, 1R)$, shows ability to detect the shaft fault in all the studied cases, and its phase shows better capabilities in distinguishing different shaft settings than the conventional linear coupling based on cross-power spectrum, as will be discussed in section 3.5.

3.2 Cross-Power Spectrum and Linear Coupling Between Spectral Components of Vibration Signals

When two vibration signals, $x(t)$ and $y(t)$, are collected simultaneously, cross-correlation $R_{xy}(\tau)$ is a useful function to investigate the linear relation between the two signals as given in equation (3.1).

$$R_{xy}(\tau) = E\{x(t+\tau)y^*(t)\} \tag{3.1}$$

As discussed in section 2.5, the Fourier transform of the cross-correlation function is the cross-power spectrum, $C_{XY}(f)$, as given in equation (3.2) where $X(f)$ and $Y(f)$ are the Fourier transforms of $x(t)$ and $y(t)$, respectively. The cross-power spectrum is a useful tool to describe linear correlation between the two signals as a function of frequency which is easy to relate to specific rotating component. The magnitude of the cross-power spectrum, $|C_{xy}(f)|$, describes how strong the linear coupling is between the two signals at frequency f, while its phase difference, $\theta_{XY}(f)$, can be used to differentiate between different physical faults that produce the same vibrating frequencies.

$$C_{XY}(f) = E\{X(f)Y^*(f)\} = |C_{xy}(f)| \ e^{j\theta_{XY}(f)} \tag{3.2}$$

When $X(f)$ is an input signal to a linear system, the output signal $Y(f)$ is linearly coupled to $X(f)$ in frequency domain by the following relation:

$$Y(f) = H(f)X(f) \tag{3.3}$$

where, $H(f)$, is the linear transfer function of the system.

Therefore, assuming that $X(f)$ and $Y(f)$ are two vibration signals collected at the hanger bearings supporting a drive-shaft with unknown condition, linear transfer characteristics of that shaft at any particular frequency can be theoretically estimated by substituting from (3.3) in (3.2) as follows:

$$H(f) = \frac{C^*_{XY}(f)}{E\{|X(f)|^2\}} = \frac{E\{X^*(f)Y(f)\}}{E\{|X(f)|^2\}} \tag{3.4}$$

3.3 Cross-Bispectrum and Quadratic-Nonlinear Coupling Among Spectral Components of Vibration Signals

The cross-bispectrum is the Fourier transform of the cross-bicorrelation function (third-order moment) as given in (3.5) and (3.6) as follows [32], [41]:

$$R_{xxy}(\tau_1, \tau_2) = E\{x(t+\tau_1)x(t+\tau_2)y^*(t)\} \tag{3.5}$$

$$S_{XXY}(f_1, f_2) = E\{X(f_1)X(f_2)Y^*(f_1+f_2)\} \tag{3.6}$$

The advantage of bispectrum over linear power spectral analysis is its ability to characterize quadratic nonlinearities in monitored systems. One of the characteristics of nonlinearities is that various frequencies "mix" to form new combinations of "sum"

and "difference" frequencies. An important signature to detect nonlinearity is based on the fact that there exists a phase coherence, or phase coupling, between the primary interacting frequencies and the resultant new sum and difference frequencies [35]. In other words, cross-bispectrum given in (3.6) investigates the quadratic nonlinear coupling between any two frequency components, f_1 and f_2, in signal $X(f)$ that interact to produce a third frequency, $f_1 + f_2$, at another signal $Y(f)$. This nonlinear relation is plotted in two-dimensional frequency space $(f_1 - f_2)$, as shown in Figure 2.2.

By analogy to linear transfer function in equation (3.4), the second-order nonlinearity in a the drive-shaft can be estimated based on the cross-bispectrum between two signals collected at the hanger bearings supporting that shaft. Thus, assuming that part of the power at frequency component $Y(f_1 + f_2)$ is generated due to quadratic nonlinear coupling between $X(f_1)$ and $X(f_2)$, $Y(f_1 + f_2) = A_{QC}(f_1, f_2)X(f_1)X(f_2)$, the quadratic coupling coefficient between the two frequencies f_1 and f_2 can be calculated as follows;

$$A_{QC}(f_1, f_2) = \frac{S^*_{XXY}(f_1, f_2)}{E\{|X(f_1)X(f_2)|^2\}} \tag{3.7}$$

Using average over ensemble of M realizations to estimate the expected value operators in equation (3.7), $A_{QC}(f_1, f_2)$ can be estimated directly from the discrete Fourier transform of sampled versions of $x(t)$ and $y(t)$ as follows:

$$A_{QC}(l, k) = \frac{\frac{1}{M}\sum_{i=1}^{M} X_i^*[l]\, X_i^*[k]\, Y_i[l+k]}{\frac{1}{M}\sum_{i=1}^{M} |X_i[l]\, X_i[k]|^2} \tag{3.8}$$

The quadratic-nonlinearity coupling coefficient, $A_{QC}(l, k)$, is two-dimensional complex matrix that characterizes the system under study and it is calculated for the whole same bi-frequency space as cross-bispectrum shown in Figure 2.2(b). However,

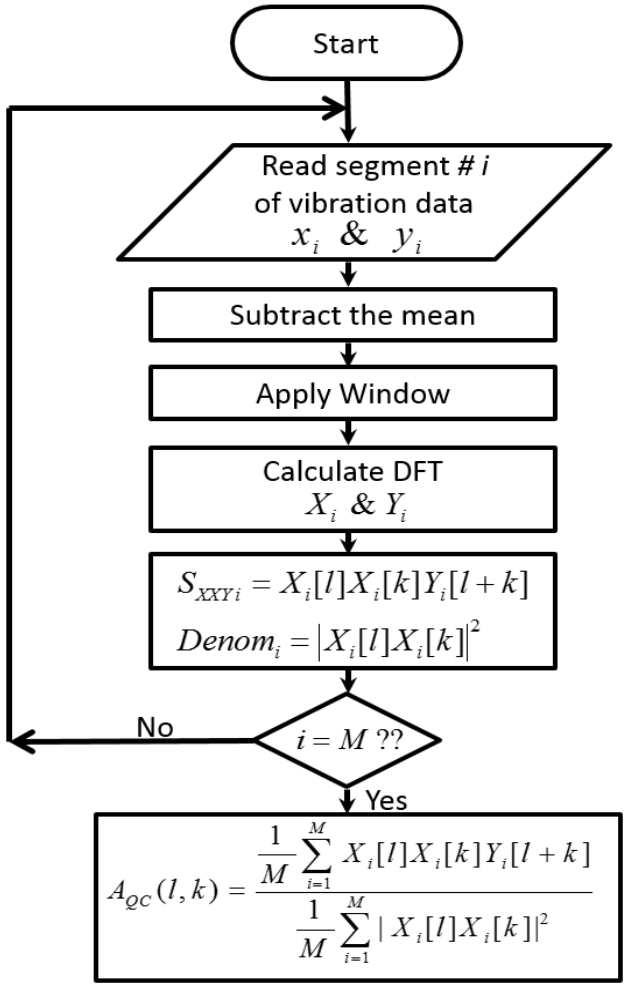

Figure 3.1 Flow diagram for digital estimation of the quadratic coupling coefficient, $A_{QC}(l,k)$

due to the division, it can be numerically unstable when the denominator is very small. Therefore, due to it its more simple definition, the cross-bispectrum will be used to analyze nonlinear signature for different drive-shaft faults. Once coupling frequency coordinate points of interest are determined, computational power, complexity, and memory can be saved by limiting the calculation to only those coordinate-points. Flow diagram for digital estimation of $A_{QC}(l,k)$ is shown in Figure 3.1.

In this chapter, we will utilize $A_{QC}(l,k)$ to measure nonlinearities in vibration signals in order to quantitatively assess health conditions of tail rotor drive train of

military rotorcraft, whose description is provided in the next section.

3.4 Experiment Setup and Vibration Data Description

The data used in this study consist of 12 experiment runs arranged in 4 sets of shaft settings taken with different shafts alignment and balance. For each shaft setting, the experiment is repeated 3 times using different hanger bearing articles in the aft position of the TRDT test stand described in section 1.3, Figure 1.5. In order to keep data organized, a naming convention is followed as summarized in Table 3.1. The first digit in the test number represents the shaft setting and varies from 0 to 3; where 0 is used to represent baseline case, 1 for unbalanced case, 2 for misalignment, and 3 for a combined case of both shaft imbalance and misalignment, respectively. The remaining of the test number consists of the serial number of the hanger bearing used at the aft position as follows: S/N: 0316, S/N: 0321, and S/N: 0373.

Table 3.1 Vibration data set and test numbers

Test number		Hanger bearing S/N		
		0316	0321	0373
Shaft setting	Baseline “0"	00316	00321	00373
	Imbalance “1"	10316	10321	10373
	Misaligned “2"	20316	20321	20373
	Imbal./Misal. “3"	30316	30321	30373

The original configuration of the test stand uses balanced drive-shafts straightly aligned as a baseline for normal operations (case “0” in Table 3.1). Aligned-unbalanced shafts (case “1” in Table 3.1) are tested under the condition of drive shaft #4 is unbalanced by 0.135 oz-in, and drive shaft #5 is unbalanced by 0.190 oz-in. Angular misalignment between shafts (case “2” in Table 3.1) is tested under 1.3° misalignment between the #3 and the #4 drive shafts, and 1.3° between the #4 and the #5 drive shafts.A combination of the last two cases, imbalance -misalignment, is also tested (case “3” in Table 3.1).

During each experiment run, accelerometers' data are collected simultaneously from the forward and afterward hanger bearing positions (denoted as FHB and AHB in Figure 1.5) once every two minutes during the course of the thirty minute run, making total of 15 data segments. Each data segment has 65536 data points collected at sampling rate of 48kHz (f_S) which results in data collection time of approximately 1.31 sec per acquisition. Vibration signals are collected during operation of the test stand at a constant rotational speed of 4863 rpm (81.05 Hz) from the prime mover, with a simulation of the output torque at 111 ft.lb. from the output motor. Rotational speed is the speed of the input shafts and hanger bearings. Output torque is given by the torque at the output of the tail rotor gearbox simulating rotor operation while the torque applied to the input shafts and hanger bearings is equal to 32.35 ft.lb.

Nominally, the acceleration at a hanger bearing should be uniform if measured anywhere along the radial direction with only a difference in phase. However, in the presence of an imbalanced shaft, there will be a normal force F_u towards the center of the bearing acting along the radial line to the imbalanced mass centroid. When there is misalignment between shafts, the shaft no longer rotates about its center of mass causing a normal force that counters the off-axis inertia, F_m. Both fault conditions lead to different accelerations at different points around the bearing and elliptical acceleration profile, D_u and D_m, as shown in Figure 3.2. This acceleration is picked up by the dedicated accelerometer in x axis and recorded as vibrations of the form:

$$D_x = A_x \cdot \cos(\omega t + \psi_x) \tag{3.9}$$

where D_x and A_x are displacements and amplitude of displacements in x axis directions, ω is angular velocity, and ψ_x is phase angles.

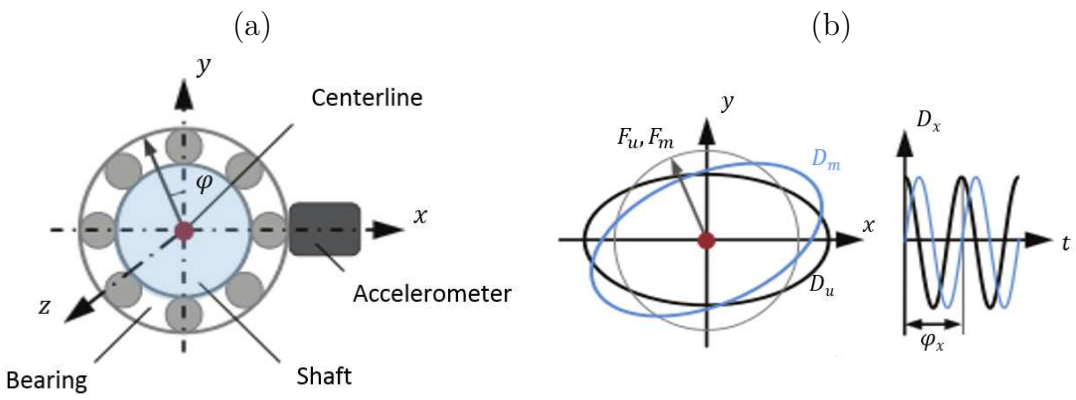

Figure 3.2 Misalignment and imbalance forces and vibrations: (a) cross-section of the bearing and the shaft at the accelerometer location, (b) displacement or vibration components in the x-axis directions (D_u orbit when $\varphi_y - \varphi_x = 90°$, D_m when $\varphi_y - \varphi_x = 120°$)

3.5 Results and Discussion

In this section, drive-shaft conditions are characterized using the vibration signals collected at the bearings supporting the shaft. Using system identification approach, both linear and quadratic transfer characteristics of the drive-shaft can be estimated based on cross-power spectrum and cross-bispectrum, respectively, as discussed in section 3.3. Vibration signals at the FHB and AHB in Figure 1.5 are used as $x(t)$ and $y(t)$. As mentioned in the previous section, each experiment run has 15 vibration data segments. In order to get bigger set of signal realizations to estimate the expected value operator by average over ensemble of M realizations, each data segment is split into two, so we have total number of M=30 data segments for each experiment run, with each segment has 32768 data points. This results in frequency resolution equal to $\Delta f = 1.46$Hz when discrete Fourier transform is calculated using fast Fourier transform (FFT) approach. In the following discussion, for easier notation of frequency values, we will use "$1R$, $2R$, $3R$, ..." to denote "first, second, third, ..." harmonics of the shaft rotating frequency ($1R = 81.05$Hz).

Figure 3.3 shows the magnitude plot of the cross-power spectrum for all shaft settings using vibration data set from hanger bearing with S/N 0321. Ideally, we expect to see very low vibrations in the baseline case. However, Figure 3.3(a) indicates that spectral peaks at $1R$ and $3R$ dominate the vibration spectrum in this case. Taking into considering the loading torque transferred to the shafts through the IGB as shown in Figure 1.5, results in Figure 3.3(a) can be interpreted as possible oscillations due to the unsymmetrical loading profile on the drive shafts which causes time varying forces at $1R$ and $3R$ frequencies.

Current practice in monitoring rotating shaft conditions involves using the vibration magnitude at the spectral peaks corresponding to the first three rotating shaft harmonics ($1R$, $2R$, and $3R$) as shaft's condition indicators [16], [39]. Comparison with the baseline is usually done on a logarithmic amplitude scale with increases of 6-8 dB considered to be significant and changes greater than 20 dB from the baseline considered serious [42]. Referring to Figure 3.3, One interesting observation is that magnitude of $2R$ frequency (161.1 Hz) is distinguishing all the faulted cases (Figure 3.3(b:d)) from the baseline case (Figure 3.3(a)) with magnitude difference exceeds 6 dB. Vibration magnitude at other shaft harmonics, $1R$ and $3R$, do not show considerable increase compared to the baseline case, as summarized in Table 3.2. Therefore, we will focus our attention to $2R$ condition indicator and we will use it to evaluate the linear coupling between the FHB and AHB vibrations in all the experimental data set.

Table 3.2 Cross-power spectral peak comparison with baseline case at shaft harmonics in dB

Spectral peak	$1R$=80.57	$2R$=161.1	$3R$=243.2
UB(10321)	3.0126	13.0387	-4.7475
MA(20321)	-0.1402	11.8538	-3.4963
UB/MA(30321)	3.0966	12.7088	-10.6793

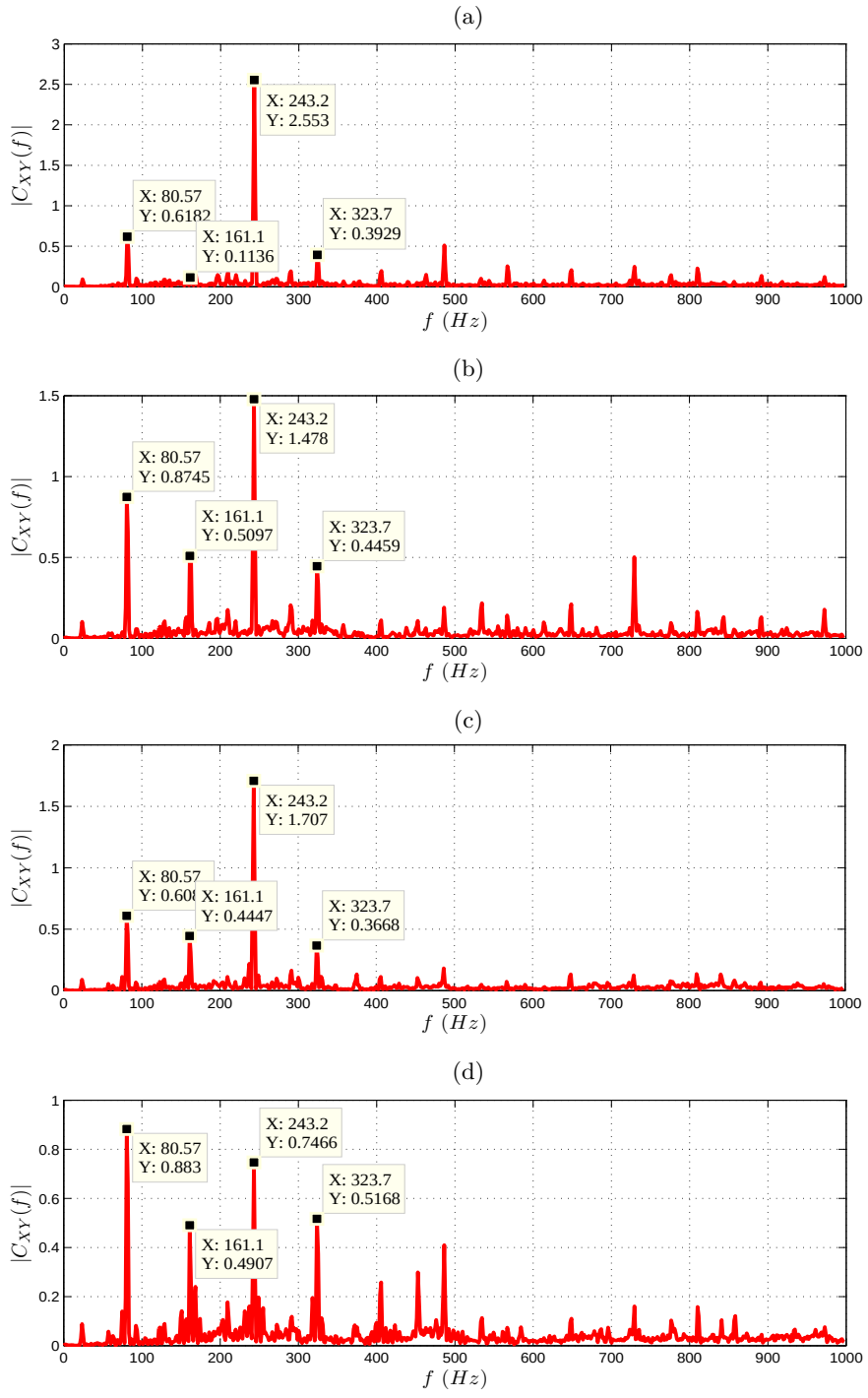

Figure 3.3 Magnitude of the cross-power spectrum between FHB and AHB vibrations: (a) 00321, (b) 10321, (c) 20321, and (d) 30321

More information can be extracted from the same vibration data by extending the analysis to include third order statistics (bispectrum) to analyze the quadratic-nonlinear behavior of the drive shaft. Magnitude of the cross-bispectrum is plotted for the same data set studied before, as shown in Figures 3.4 and 3.5. The baseline case (aligned-balanced) shown in Figure 3.4(a) has the least quadratic nonlinear frequency interaction among other cases. Highest bispectral peaks exist at the following coordinate points: $(2R, 1R)$, $(3R, 3R)$, $(3R, 1R)$, and $(4R, -1R)$. In the case of shaft imbalance shown in Figure 3.4(b), increased frequency-interaction along $2R$ frequency can be observed; namely at the coordinate points of $(2R, 2R)$, $(2R, 1R)$, and $(2R, -1R)$. Another interesting observation is the high bispectral peak at $(1R, 1R)$ compared to the baseline case.

It is worthwhile to note that this high peak at $(1R, 1R)$ coordinate point clearly distinguishes all the faulted cases (Figure 3.4(b) and 3.5(a,b)) from the baseline case (Figure 3.4(a)). Also, the physical interpretation of this frequency coupling point explains that part of the vibration power at the $2R$ frequency, which is used in conventional power spectral analysis to detect shaft abnormalities (Figure 3.3), is generated due to quadratic nonlinearity of the drive shaft causing interaction between two time varying forces at $1R$ frequency. One of those two forces exists in the baseline case due to unsymmetrical application of the torque, as discussed before in the results of Figure 3.3(a). The other interacting force is introduced when shaft misalignment and/or imbalance take place. Both of the two faults cause cyclical forces at the bearings at the speed of the shaft, but the forces due to each fault do not oscillate identically. This allows the errors to be detected uniquely by studying the quadratic coupling of vibration at the bispectral point $(1R, 1R)$.

(a)

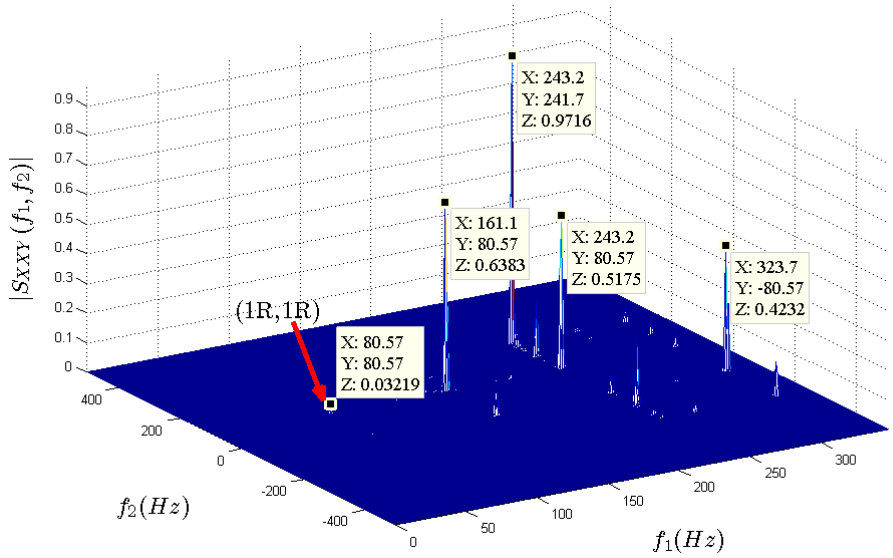

(b)

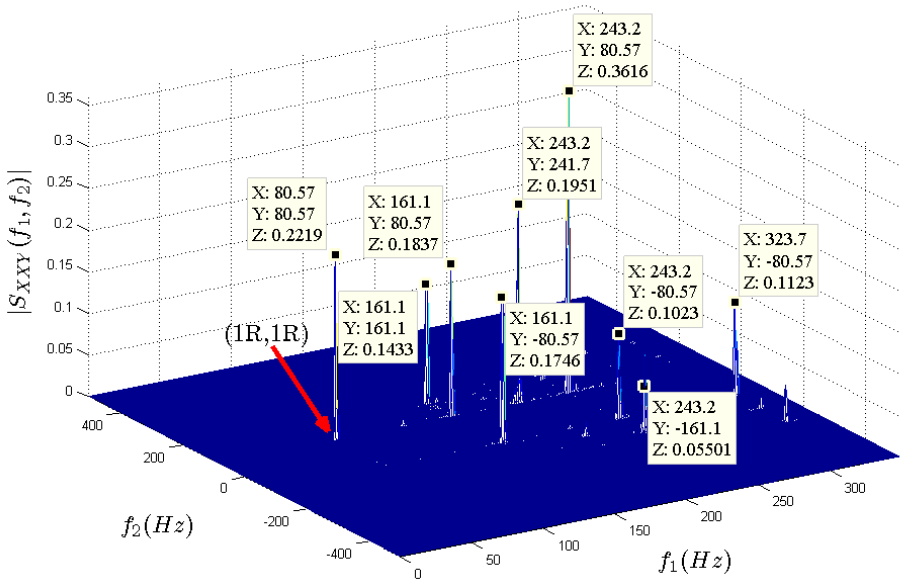

Figure 3.4 Magnitude of the cross-bispectrum between FHB and AHB vibrations: (a) 00321, and (b) 10321

(a)

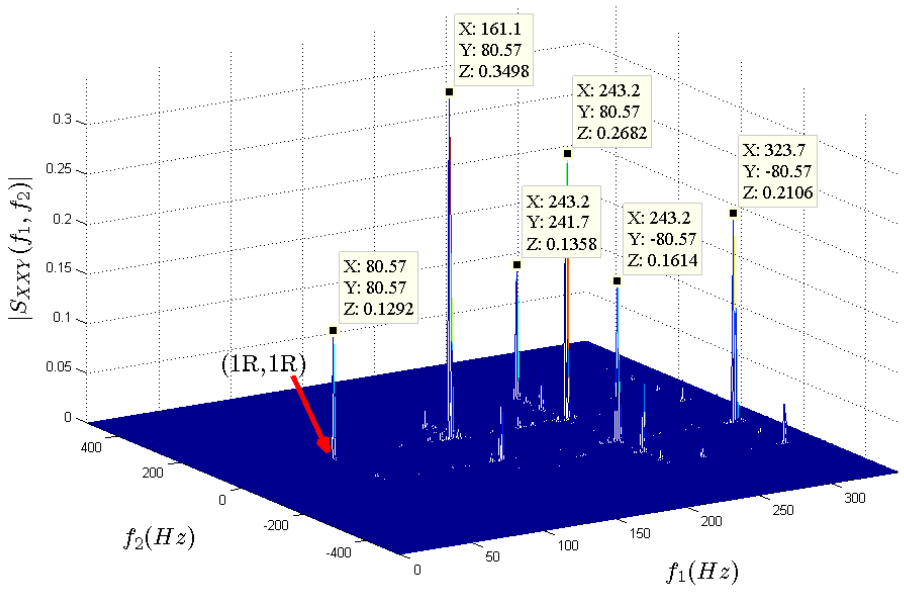

(b)

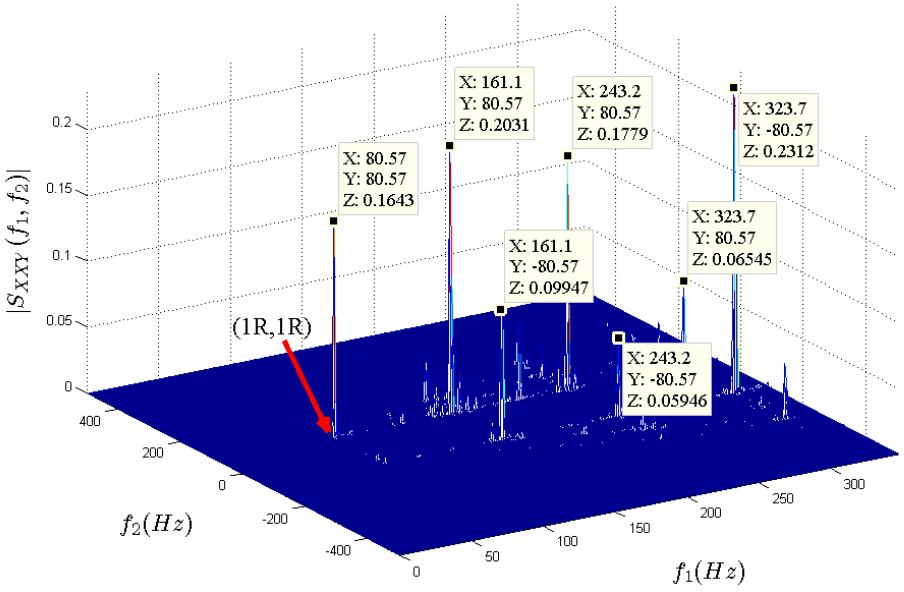

Figure 3.5 Magnitude of the cross-bispectrum between FHB and AHB vibrations: (a) 20321, and (b) 30321

Therefore, for the reasons mentioned above, although careful study of the whole cross-bispectrum may lead to more nonlinear vibration signatures, we will focus our attention to $(1R, 1R)$ coordinate point and we will use it to evaluate the nonlinear coupling between the FHB and AHB vibrations in all the experimental data set. Thus, for all the studied cases, linear transfer function in equation (3.4) is estimated at $2R$ frequency and compared to the quadratic coupling in equation (3.7) at the bi-frequency point $(1R, 1R)$, as summarized in Table 3.3 and Table 3.4.

Table 3.3 Linear coupling, $H(2R)$, for all shaft settings

Setting	SN 0316		SN 0321		SN 0373	
	$\|H\|$	ph(°)	$\|H\|$	ph(°)	$\|H\|$	ph(°)
BL(0)	0.047	65.46	0.043	84.49	0.094	68.87
UB(1)	0.251	94.81	0.293	67.49	0.268	82.88
MA(2)	0.276	80.51	0.416	66.68	0.225	46.82
UB/MA(3)	0.259	22.57	0.166	200.45	0.337	66.13

Table 3.4 Nonlinear coupling, $A_{QC}(1R, 1R)$, for all shaft settings

Setting	SN 0316		SN 0321		SN 0373	
	$\|A\|$	ph(°)	$\|A\|$	ph(°)	$\|A\|$	ph(°)
BL(0)	11.55	-66.7	10.92	-70.7	18.68	-61.4
UB(1)	59.51	2.5	60.17	-26.9	50.32	-13.7
MA(2)	53.46	174.5	78.37	160.2	74.01	234.5
UB/MA(3)	32.10	55.4	37.37	16.7	109.05	7.87

As shown in Tables 3.3 and 3.4, magnitude of both $H(2R)$ and $A_{QC}(1R, 1R)$ is higher in all the studied faulted cases than the baseline case. Thus, magnitude response of both coupling coefficients can be used as a good indication of the fault. In order to differentiate between different faulted cases, the phase of the coupling can be used. Therefore, phase of both linear and nonlinear coupling will be used to compare between them in terms of the ability of each to assess different health conditions of the drive shafts.

Phase of linear and nonlinear coupling

Phase values reported in Tables 3.3 and 3.4 are average values calculated over the entire of each experiment run. For more information about phase variations during one single experiment run, and form one run to another, Figures 3.7 and 3.6 are plotted. Phase of both linear and quadratic coupling are estimated from each data segment in each experiment run, then plotted next to each other with data from the same shaft setting is plotted with the same color and line style.

Phase of the nonlinear coupling metric shows consistent results around its average and does not overlap from shaft case to another, as shown in Figure 3.7. On the other hand, phase of the linear coupling metric overlaps from one point to another as well as from one data set to another, as shown in Figure 3.6.

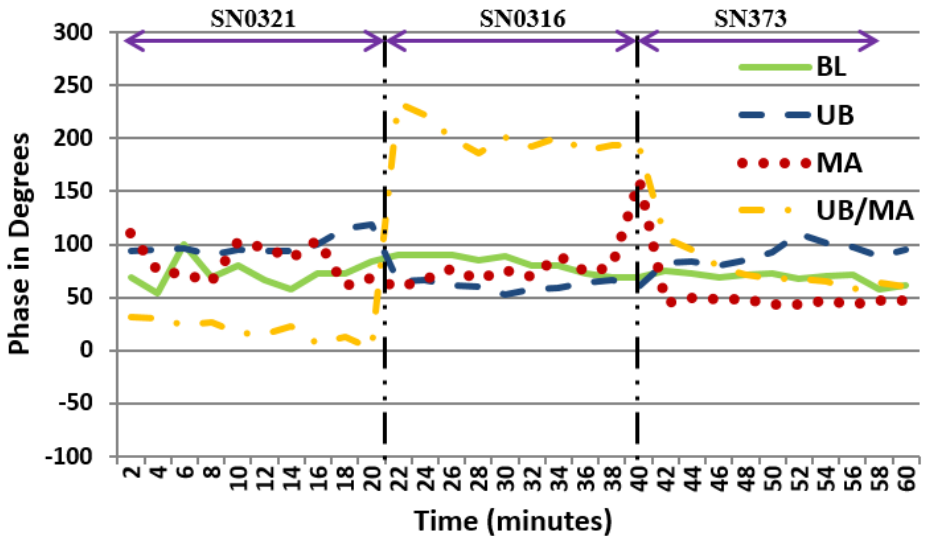

Figure 3.6 Variations in the phase values for the linear coupling metric, $H(2R)$

To compare statistical behavior of the variation in phase values shown in Figures 3.6 and 3.7, and based on central limit theory, probability distribution function of the variable phase can be approximated by normal distribution with the same mean (μ) and variance (σ^2) as shown in Figures 3.8 and 3.9. Figure 3.9 shows that, using

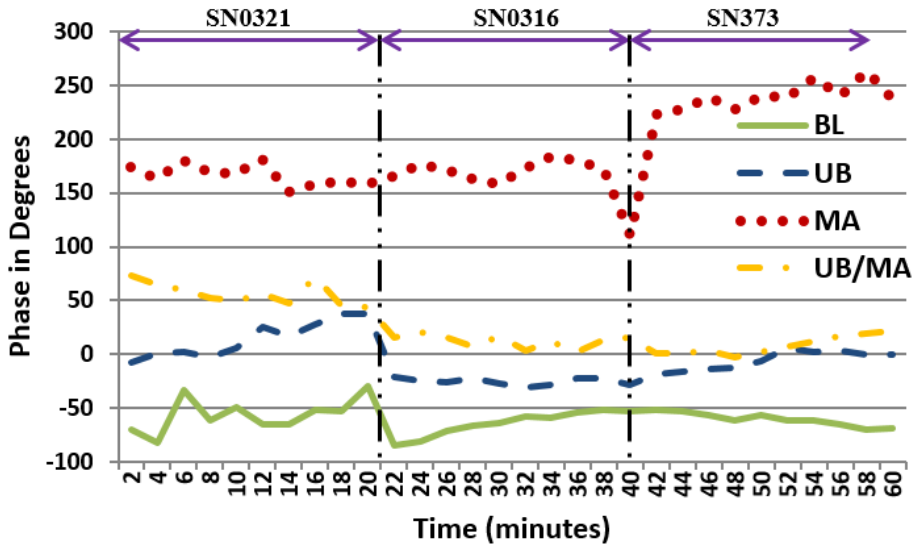

Figure 3.7 Variations in the phase values for the quadratic-nonlinear coupling metric, $A_{QC}(1R, 1R)$

the phase of the proposed quadratic coupling metric, $A_{QC}(1R, 1R)$, shaft misalignment and imbalance can be separated from the baseline case and from each others. Wider phase difference among faulted cases relax the requirements on setting the threshold values to distinguish each case, which in turn decrease the probability of false alarm. On the other hand, Figure 3.8 shows that it is hard to set the threshold values to distinguish between the studied cases using the phase of the linear coupling metric, $H(2R)$. Statistical parameters of phase variations in Figures 3.6 and 3.7 are summarized in Table 3.5.

Table 3.5 Statistical summary of phase information for linear coupling, $H(2R)$, and nonlinear coupling, $A_{QN}(1R, 1R)$

Statistical Parameter		BL	UB	MA	UB/MA
Ph(H)	*Mean* μ	74.24	84.15	70.62	97.72
	STD σ	10.84	18.43	25.95	78.95
Ph(A_{QC})	*Mean* μ	-60.29	-5.38	190.52	25.60
	STD σ	12.12	19.68	38.23	23.80

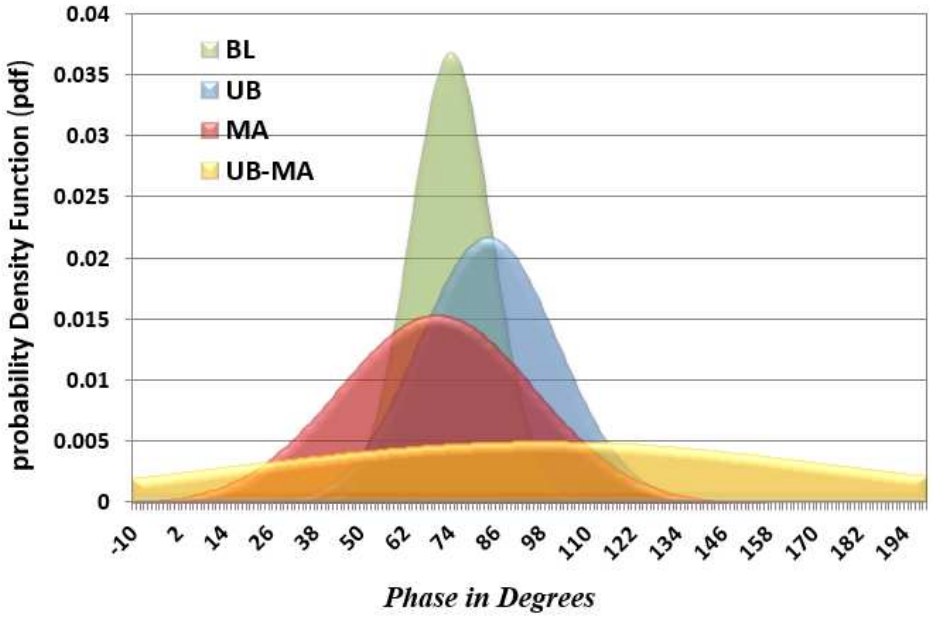

Figure 3.8 Normal distribution using μ and σ form variable phase values in Figure 3.6

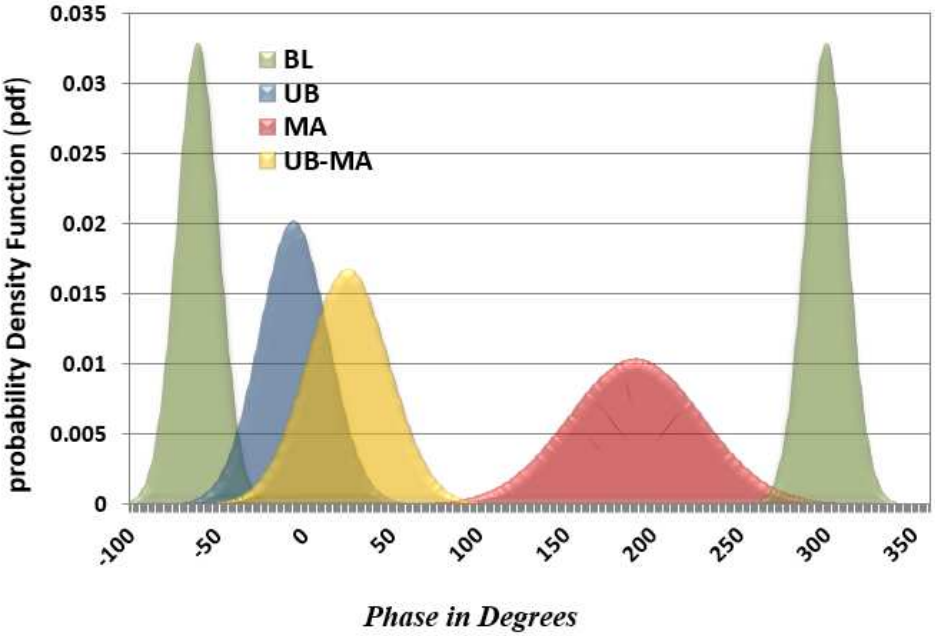

Figure 3.9 Normal distribution using μ and σ form variable phase values in Figure 3.7

3.6 Fault Detection in Presence of Noise

When power spectral peak at $2R$ frequency is used as condition indicator (CI) to detect shaft faults, magnitude of the power spectrum at this frequency is estimated and fault is detected when this magnitude exceeds predefined threshold (γ), which may be 6dB compared to baseline case, as discussed before. In the presence of white Gaussian noise, extra power added by the noise may cause a spectral peak magnitude in a small margin to the detection threshold to exceed it leading to false alarm.

In this section, we theoretically study the effect of noise on condition indicators (CIs) based on the magnitude of conventional power spectrum compared to CIs based on magnitude of bispectrum. The idea we are trying to investigate is: if a CI has a value that is close to the threshold γ, how much noise is going to move the CI level to hit the threshold level causing false alarm.

Therefore, we consider it to be fault 'detection' problem in the form of hypothesis testing [43] with null hypothesis, $\mathcal{H}_0$, and alternative hypothesis, $\mathcal{H}_1$, as follows:

$\mathcal{H}_0$: No significant fault at the frequency of interest ($CI < \gamma$)

$\mathcal{H}_1$: Significant fault at the frequency of interest ($CI \geq \gamma$)

For any hypothesis test, two types of possible errors should be considered: false-negative, and false-positive errors [44]. In the context of our fault detection problem, the false-negative error is the case when the CI is smaller than the detection threshold, $CI < \gamma$, so that no fault is indicated but in fact there is actually a fault. However, in our noise analysis study, the false-negative cases do not needed to be considered because the noise power is merely added to the CI power.

Meanwhile, the false-positive error (or false alarm error) is the case when the estimated CI is greater than the detection threshold so that it indicates the presence of fault when in fact fault does not exist. Then, the false alarm probability regarding

fault detection becomes as follows;

$$\begin{aligned} P_{fa} &= P(\mathcal{H}_1|\mathcal{H}_0) \\ P_{fa} &= P(CI \geq \gamma \mid \text{No significant fault exist}) \end{aligned} \tag{3.10}$$

In order to theoretically compare the effect of noise on CIs based on conventional power spectrum in one side versus CIs based on bispectrum on the other side, we consider a simple signal model, $x(t)$, to simulate our case as shown in equation (3.11).

$$\begin{aligned} x(t) = \quad & A_1 \cos(2\pi f_1 t + \theta_1) + A_2 \cos(2\pi f_2 t + \theta_2) \\ & + A_{12} \cos(2\pi f_1 t + \theta_1) \times \cos(2\pi f_2 t + \theta_2) \end{aligned} \tag{3.11}$$

In the following analysis, we will refer to the noisy signal as $x_n(t)$ which represent the signal under study $x(t)$ with added white Gaussian noise $n(t)$ as follow;

$$x_n(t) = x(t) + n(t) \tag{3.12}$$

Noise Effect on CIs Based on Magnitude of Conventional Power Spectrum

Consider a condition indicator CI that is based on magnitude of the power spectrum of signal $x_n(t)$ at certain frequency f ($2R$ in our shaft-fault case). This CI can be estimated from the power spectrum, as discussed in Chapter 2, as follow;

$$CI^2 = E\{X_n(f)X_n^*(f)\} = E\{(X(f) + N(f))(X(f) + N(f))^*\} \tag{3.13}$$

where $N(f)$ is the Fourier transform of the noise signal $n(t)$. Since $X(f)$ and $N(f)$ are independent, equation (3.13) can be rewritten as follows;

$$CI^2 = E\{|X(f)|^2\} + E\{|N(f)|^2\} \tag{3.14}$$

The value $E\{|X(f)|^2\}$ in equation (3.14) represents the actual value of the condition indicator based on the pure signal $x(t)$, and we will refer to this part as C_x^2. $E\{|N(f)|^2\}$ represents the power added by the noise. Assuming that the noise $n(t)$ is zero-mean Gaussian random variable ($n(t) \sim \mathcal{N}(0, \sigma_n^2)$), its discrete Fourier transform is also zero-mean Gaussian random variable ($N(f) \sim \mathcal{N}(0, \frac{\sigma_n^2}{L})$), where L is the number of discrete Fourier transform points. Recall that the expected value operator $E\{.\}$ is practically estimated using average over ensemble of M realization of the signal, as discussed in Chapter 2. Summation of magnitude squared normal distribution becomes a central chi-square random variable with M degrees of freedom, as shown in equation (3.15).

$$\begin{aligned} CI^2 &= C_x^2 + E\{|\mathcal{N}(0, \frac{\sigma_n^2}{L})|^2\} \\ &= C_x^2 + \frac{2}{M}\sum_{i=1}^{M} |\mathcal{N}_i(0, \frac{\sigma_n^2}{L})|^2 \\ &= C_x^2 + \frac{2\sigma_n^2}{LM}\ \chi_M^2 \end{aligned} \tag{3.15}$$

Substituting form equation (3.15) in equation (3.10), probability of false alarm can now be estimated as follows;

$$\begin{aligned} P_{fa} &= P(C_x^2 + \frac{2\sigma_n^2}{LM}\ \chi_M^2 \geq \gamma \mid \text{No significant fault exist}) \\ P_{fa} &= P\left(\chi_M^2 \geq \frac{LM}{2(\sigma_n/\gamma)^2} \left(1 - \left(\frac{C_x}{\gamma}\right)^2\right) \right) \end{aligned} \tag{3.16}$$

where γ indicates the fault detection threshold, (C_x/γ) is signal-to-threshold ratio (STR) which indicates how close the pure-signal is to the threshold, and (σ_n/γ) is noise-to-threshold ratio (NTR). From (3.16), we can theoretically project the probability of false alarm with respect to the noise, and clearly conclude that the probability of false alarm increases as σ_n increases. It worthwhile to mention here that equation (3.16) makes sense only when $(C_x < \gamma)$.

Figure 3.10 illustrates the theoretical and experimental results regarding the change of the probability of false alarm as the noise-to-threshold power ratio (NTR) increases, and where NTR is defined as follows;

$$\text{Noise-to-Threshold power Ratio (NTR)} = 20\log_{10}\left(\frac{\sigma_n}{\gamma}\right) \tag{3.17}$$

For this analysis, signal model in (3.11) is considered. The sampling frequency is set to 4800 Hz, f_1=80 Hz, f_2=120 Hz, number of signal segments or realizations M=15, and number of discrete Fourier transform points L=1024. The signal-to-threshold power ratio (STR) is set to 0.8 (-1.94 dB). Theoretical result is derived from (3.16), and Monte-carlo type numerical experiments are carried out using the synthesized signal in (3.11).

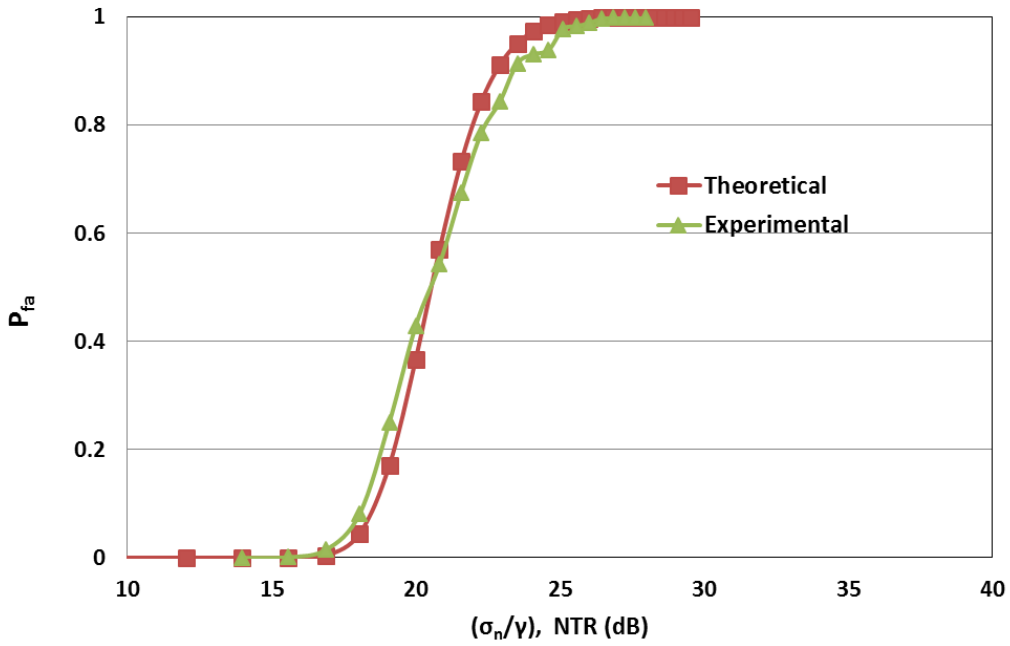

Figure 3.10 Effect of noise on CI based on magnitude of conventional power spectrum: variation of the probability of false alarm, P_{fa}, with respect to noise-to-threshold power ratio, NTR (σ_n/γ)

Moreover, using equation (3.16), we can theoretically study the variation of the probability of false alarm with respect to the number of signal realizations M, the number of discrete Fourier transform points L, and the signal-to-threshold power ratio (STR). For example, Figure 3.11 shows variations in the probability of false alarm with respect to the noise-to-threshold power ratio (NTR) at different values of signal-to-threshold power ratio (STR).

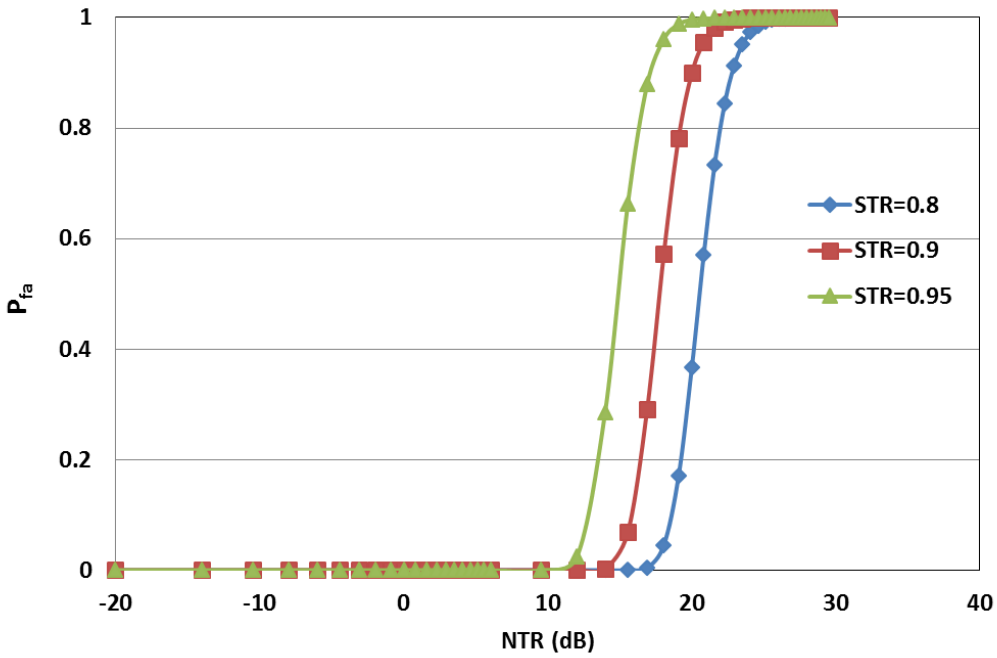

Figure 3.11 Effect of STR (C_x/γ) on the variation of the probability of false alarm, P_{fa}, with respect to NTR (σ_n/γ)

Noise Effect on Cross-Bispectrum

In this subsection, we study the effect of noise on the cross-bispectrum so we can use it to analyze the effect of noise on CI based on magnitude of cross-bispectrum.

In order to determine the statistical behaviour of the cross-bispectrum under the effect of white Gaussian noise, we start with recalling that white Gaussian noise affects all the frequency components with the same amount of noise power which

is normally distributed ($N(f) \sim \mathcal{N}(0, \frac{\sigma_n^2}{L})$) where L is the number discrete Fourier transform points. Thus, $X_n(f_1) = X(f_1) + N(f_1)$, $X_n(f_2) = X(f_2) + N(f_2)$, and the cross-bispectrum becomes as follows;

$$S_{XXY}(f_1, f_2) = E\{(X(f_1)+N(f_1))(X(f_2)+N(f_2))(X(f_3 = f_1+f_2)+N(f_3))^*\} \quad (3.18)$$

Since we are dealing with shaft harmonics, our signal of interest mainly consists of sinusoidal components rather than broadband spectral components. Thus, signal spectral component at certain frequency can be represented as magnitude and phase; for example, $X(f_1) = \frac{A_1}{2}e^{j\theta}$. Thus, cross-bispectrum in equation (3.18) can be rewritten as follows;

$$S_{XXY}(f_1, f_2) = E\left\{\left(\frac{A_1}{2}e^{j\theta_1} + N(f_1)\right)\left(\frac{A_2}{2}e^{j\theta_2} + N(f_2)\right)\left(\frac{A_3}{2}e^{j(\theta_1+\theta_2)} + N(f_3)\right)^*\right\} \quad (3.19)$$

Please note that magnitude A and phase θ of each sinusoidal frequency components are deterministic. Thus, $E\{.\}$ works only on the noise components which we will refer to as N_1, N_2, and N_3 for simplicity. Hence, equation (3.19) can be simplified as follows;

$$\begin{aligned} S_{XXY}(f_1, f_2) \quad &= \left(\frac{A_1A_2A_3}{8}\right) + E\{N_1N_2N_3^*\} \\ &+ \frac{A_1}{2}e^{j\theta_1}\frac{A_2}{2}e^{j\theta_2}E\{N_3^*\} + \frac{A_1A_3}{4}e^{j\theta_2}E\{N_2\} + \frac{A_2A_3}{4}e^{j\theta_1}E\{N_1\} \\ &+ \underbrace{\frac{A_1}{2}e^{j\theta_1}E\{N_2N_3^*\}}_{E_1} + \underbrace{\frac{A_2}{2}e^{j\theta_2}E\{N_1N_3^*\}}_{E_2} + \underbrace{\frac{A_3}{2}e^{-j(\theta_1+\theta_2)}E\{N_1N_2\}}_{E_3} \\ &= \left(\frac{A_1A_2A_3}{8}\right) + 0 + 0 + 0 + 0 + E_1 + E_2 + E_3 \end{aligned} \quad (3.20)$$

The noise is assumed to be zero-mean white Gaussian noise. Thus, in equation (3.20), first-order moments and third order moments are equal to zero, $E\{N_1\} =$

$E\{N_2\} = E\{N_3\} = E\{N_1 N_2 N_3^*\} = 0$. Also, E_1 in equation (3.20) can be rewritten as follows;

$$\begin{aligned} E_1 \quad &= \frac{A_1}{2} e^{j\theta_1}\ E\{N_2 N_3^*\} = (A_{1r} + jA_{1i}) E\{(N_{2r} + jN_{2i})(N_{3r} - jN_{3i})\} \\ &= A_{1r}\ E\{N_{2r}N_{3r} + N_{2i}N_{3i}\} - A_{1i}\ E\{N_{2i}N_{3i} - N_{2r}N_{3r}\} \\ &+ jA_{1r}\ E\{N_{2i}N_{3r} - N_{2r}N_{3i}\} + jA_{1i}\ E\{N_{2r}N_{3r} + N_{2i}N_{3i}\} \end{aligned} \tag{3.21}$$

In (3.21) above, each estimation $E\{N_x N_y\}$ is estimated by ensemble-averaging over M segments. Then, the ensemble averages can be considered as the sum of the product of independent Gaussian random variables. Although the product of the Gaussian random variables is not a Gaussian, the sum of the product of the Gaussian random variables can be approximated as a Gaussian random variable by the central limit theorem [45]. Thus, if N_x and N_y are independent, the variance of the approximated Gaussian random variable becomes;

$$var\{E\{N_x N_y\}\} \simeq var\{\frac{1}{M}\sum_{k=1}^{M} N_x^{(k)} N_y^{(k)}\} \simeq \frac{1}{M^2}.M.\left(\frac{\sigma_n^2}{L}\right)^2 = \frac{\sigma_n^4}{ML^2} \tag{3.22}$$

The real and the imaginary parts of E_1 in equation (3.21) become Gaussian random variables since they are weighted sum of Gaussian random variables, and the variance of E_1 becomes as follows;

$$var\{E_1\} \simeq 2A_{1r}^2\ \frac{\sigma_n^4}{ML^2} + 2A_{1i}^2\ \frac{\sigma_n^4}{ML^2} = 2(A_{1r}^2 + A_{1i}^2)\ \frac{\sigma_n^4}{ML^2} = A_1\ \frac{\sigma_n^4}{ML^2} \tag{3.23}$$

Therefore, variance of the random variable term $(E_1 + E_2 + E_3)$ in equation (3.20) becomes as follows;

$$var\{E_1 + E_2 + E_3\} \simeq (A_1^2 + A_2^2 + A_3^2)\ \frac{\sigma_n^4}{ML^2} \tag{3.24}$$

Thus, the cross-bispectrum of the noisy signal in equation (3.20) consists of two main quantities; first quantity, $\left(\frac{A_1 A_2 A_3}{8}\right)$, is deterministic which represents the value of the pure three-wave coupling when noise does not exist, and second quantity is zero-mean Gaussian random variable with variance given in (3.24). Therefore, equation (3.20) can be rewritten as follow;

$$S_{XXY}(f_1, f_2) = \left(\frac{A_1 A_2 A_3}{8}\right) + \mathcal{N}(0, (A_1^2 + A_2^2 + A_3^2)\ \frac{\sigma_n^4}{ML^2}) \tag{3.25}$$

Noise Effect on CIs Based on Magnitude of Cross-Bispectrum

Referring to the above subsection, the cross-bispectrum of the noisy signal can be written as summation of two main quantities; first quantity is deterministic which represents the value of the pure three-wave coupling when noise does not exist, and second quantity is zero-mean Gaussian random variable as follow;

$$S_{XXY}(f_1, f_2) = \left(\frac{A_1 A_2 A_3}{8}\right) + \mathcal{N}(0, (A_1^2 + A_2^2 + A_3^2)\ \frac{\sigma_n^4}{ML^2}) \tag{3.26}$$

Now, if the condition indicator CI is based on magnitude of the cross-bispectrum at certain coordinate bi-frequency f_1, f_2 ($(1R, 1R)$ in our shaft-fault case), this CI is estimated from the cross-bispectrum as follows;

$$\begin{aligned} CI^2 = |S_{XXY}(f_1, f_2)|^2 \quad &= \left|\left(\frac{A_1 A_2 A_3}{8}\right)\right|^2 + E\{|\mathcal{N}(0, (A_1^2 + A_2^2 + A_3^2)\ \frac{\sigma_n^4}{ML^2})|^2\} \\ &= \left|\left(\frac{A_1 A_2 A_3}{8}\right)\right|^2 + (A_1^2 + A_2^2 + A_3^2)\frac{\sigma_n^4}{ML^2}\chi_1^2 \end{aligned} \tag{3.27}$$

If the magnitude of the sinusoidal components contributing to the three-wave coupling are all in the same order, we can assume that $A_1 = A_2 = A_3 = A$ for more simplified form of equation (3.27), and when used in estimate the probability of false

alarm in equations (3.10) gives

$$P_{fa} = P(\left(\frac{A^6}{64}\right) + 3A^2\frac{\sigma_n^4}{ML^2}\chi_1^2 \geq \gamma^6 \mid \text{No significant fault exist})$$
$$P_{fa} = P\left(\chi_1^2 \geq \frac{ML^2}{3(A/\gamma)^2(\sigma_n/\gamma)^4}\left(1 - \frac{1}{64}\left(\frac{A}{\gamma}\right)^6\right)\right) \tag{3.28}$$

where (A/γ) is signal-to-threshold ratio (STR), and (σ_n/γ) is noise-to-threshold ratio (NTR).

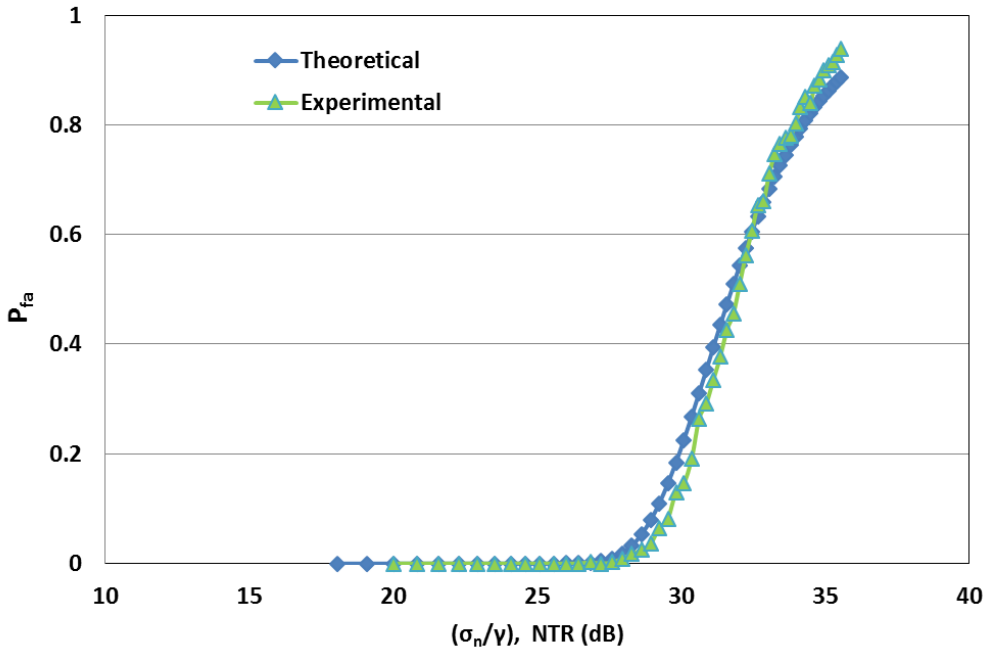

Figure 3.12 Effect of noise on CI based on magnitude of cross-bispectrum: variation of the probability of false alarm, P_{fa}, with respect to noise-to-threshold power ratio, NTR (σ_n/γ)

Figure 3.12 illustrates the theoretical and experimental results regarding the change of the probability of false alarm as the noise-to-threshold power ratio (NTR) increases. Theoretical result is derived from (3.28), and Monte-carlo type numerical experiments are carried out using the synthesized signal in (3.11).

Finally, combining graphs from Figures 3.10 and 3.12 clearly indicates that CI

based on bispectrum has better immunity to white Gaussian noise than CI based on magnitude of the conventional power spectrum, as illustrated in Figure 3.13.

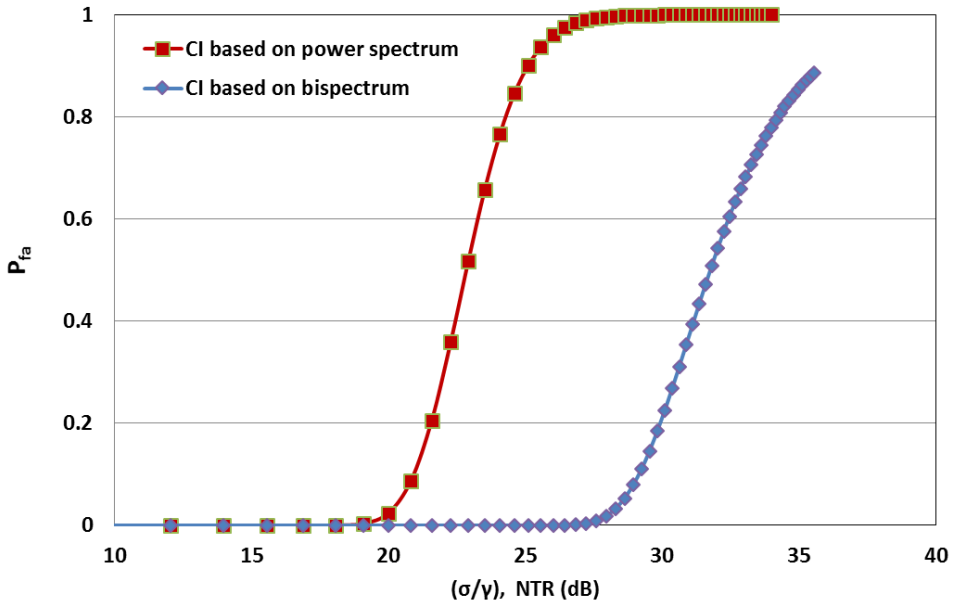

Figure 3.13 Comparison of the effect of noise on CI based on magnitude of either power spectrum or bispectrum

3.7 Conclusion

Based on cross-bispectral analysis, vibration quadratic-nonlinearity metric has been proposed and used to assess health conditions of an AH-64D helicopter tail rotor drive shafts. Nonlinear transfer function has been derived from the cross-bispectrum in analogy to the way linear transfer function is derived from cross-power spectrum. Using system approach, vibration data collected at the bearing supporting the drive shaft has been used as input and output signals to characterize the unknown conditions of the drive shaft system.

Three different hanger bearings have been used to compare vibration data collected from four different shaft settings, making grand total of twelve experiment runs. Magnitude response of both linear and quadratic coupling has been able to

detect the faulted cases compared to the baseline case. However, theoretical and Monte-carlo type experimental analysis have proven that using condition indicators based on magnitude of the bispectrum has better immunity to white Gaussian noise than condition indicators based on magnitude of the conventional power spectrum. Moreover, using the phase of the proposed nonlinear coupling has shown better capabilities in distinguishing the four studied shaft settings than the conventional linear coupling. Phase of the $A_{QC}(1R, 1R)$ metric has shown more consistent result among the three studied bearing cases for each shaft setting than what the phase of $H(2R)$ has done. It also has shown wider phase difference between the studied cases without overlap among them. Wider phase difference relaxes the requirements when setting threshold values to diagnose different faulted cases.

Chapter 4

Quadratic-Nonlinearity Power-Index Spectrum

In this chapter, a new concept of Quadratic-Nonlinearity Power-Index spectrum, $QNLPI(f)$, that can be used in signal detection and classification, is proposed based on bicoherence spectrum. The proposed $QNLPI(f)$ is derived as a projection of the three-dimensional bicoherence spectrum into two-dimensional spectrum that quantitatively describes how much of the mean square power at certain frequency f is generated by nonlinear quadratic interaction between different frequencies.

4.1 Introduction

Bispectrum and its normalized version bicoherence have shown to be useful tools in machine condition monitoring fields (e.g., [46]-[51]). However, investigation of quadratic nonlinearities using bispectrum/bicoherence becomes a challenging task when the studied signal contains wide range of frequency interactions. The three dimensional nature of these spectra requires careful design of the view and expert personnel to interpret the results in the frequency domain. Therefore, it is easier to use features extracted from those spectra to summarize and describe nonlinearities in the monitored signals. For example; bispectrum mean-magnitude and phase-entropy have been used in blind detection of photo-montage [52], normalized bispectrum entropy and normalized bispectrum squared entropy have been used in health assessment of human cardiac [53], and invariant phases of integrated bispectrum has been used to detect mines in acoustic images [54], [55]. Since machine fault diagnostic is better archived by linking certain frequency to a particular rotating component,

quadratic-nonlinearity power-index ($QNLPI(f)$) spectrum has been proposed as a way to summarize information in the 3D bicoherence into 2D frequency spectrum [56], [57].

In this Chapter, the proposed concept of the $QNLPI(f)$ is discussed including mathematical derivation, considerations in its digital computation and boundary limits. The quadratic-nonlinear power spectral density $P_{QNL}(f)$ and percentage of quadratic nonlinear power $PQNLP$ are also introduced based on the $QNLPI(f)$, as will be discussed in section 4.3. Based on higher order statistical (HOS) analysis, this chapter presents applications of the proposed nonlinearity measures to real-world vibration data obtained from a dedicated condition based maintenance experimental helicopter drive-train, as will be shown in sections 4.8 and 4.9. Health condition of different rotating components in the drive train is assessed including different combinations of drive-shaft and gearbox faults. The $QNLPI(f)$ spectrum enables us to gain more details about nonlinear harmonic generation patterns that can be used to distinguish between different cases of mechanical faults, which in turn helps to gaining more diagnostic/prognostic capabilities.

4.2 Bicoherence Spectrum

As discussed previously in section 2.3, the magnitude of the bispectrum $B_{xxx}(f_1, f_2)$ at coordinate point (f_1, f_2) measures the degree of phase coherence between the three frequency components f_1, f_2, and f_3, as repeated in equation (4.1) for convenience.

$$B_{xxx}(f_1, f_2) \quad = \quad E\{X(f_1)X(f_2)X^*(f_3 = f_1 + f_2)\} \tag{4.1}$$

However, this magnitude is also dependent on the magnitude of the relevant Fourier coefficients. Therefore, a common function used to normalize the bispectrum is called bicoherence. The bicoherence function is defined as shown in equation

(4.2) [35], [58], [59].

$$b^2_{xxx}(f_1, f_2) = \frac{|B_{xxx}(f_1, f_2)|^2}{E\{|X(f_1)X(f_2)|^2\}E\{|X(f_1 + f_2)|^2\}} \tag{4.2}$$

The bicoherence $b_{xxx}(f_1, f_2)$ in (4.2) is independent of the magnitude of the Fourier transform and bounded by $0 \leq b_x(f_1, f_2) \leq 1$, where unity means full three-waves coupling (i.e., interaction has taken place between the waves), and zero implies an absence of coherence or interaction. Moreover, it has been proven in [35] that the squared bicoherence, $b^2_x(f_1, f_2)$, quantifies the fraction of mean square power at $f_3 = f_1 + f_2$ due to the quadratic coupling between the waves at f_1 and f_2. This previous property inspired us to propose a metric that shows the quadratic interaction relation (3 waves coupling) in terms of the "result" instead of the "source" of the interaction. Hence, the bi-frequency space required to plot the bicoherence (showing the source of interaction) can be reduced to a single-frequency space (showing the accumulative results).

4.3 $QNLPI(f)$ Spectrum

The Quadratic-Nonlinearity Power-Index, $QNLPI(f)$, spectrum is proposed as an implementation of the idea discussed above, and hence it should quantify the fraction of the mean square power at a certain frequency f produced by all the possible combinations of quadratic interactions that may cause the creation of this frequency, f. This idea can be achieved by integrating the bicoherence spectrum along a straight line $f_1 + f_2 = f$ represents the locus of all quadratic interactions in $f_1 - f_2$ space that result in f, as represented by equation (4.3).

$$QNLPI(f) = \int_{f_1+f_2=f} b^2_{xxx}(f_1, f_2)\, df_1 \tag{4.3}$$

This integration along $f_1 + f_2 = f$ is depicted by the dashed line in Figure 4.1. However, we should be very careful when we apply this integration in (4.3) to the conventional region of computation indicated by the triangle "A" shown in Figure 4.1. Due to the symmetry properties, the bicoherence of interacted frequencies in the fourth quadrant (positive f_1 and negative f_2) has a redundant copy in this "A" region. Therefore, the region of computation in $f_1 - f_2$ plane is modified to fully map the quadratic interaction between different frequencies as shown in Figure 4.1. The area covered by triangle "B" maps the difference part of the interaction between two frequencies $(f_1, -f_2)$, while area covered by the upper triangle "A" maps only the sum part (f_1, f_2). Based on this new region of computation, $QNLPI(f)$ in (4.3) can be rewritten as follows:

$$\begin{aligned} QNLPI(f) &= \int_{\frac{f}{2}}^{\frac{f}{2}+\frac{f_s}{4}} b^2_{xxx}(f_1, f - f_1)\, df_1 \\ &= \int_{0}^{\frac{f_s}{4}} b^2_{xxx}(\frac{f}{2} + f_1, \frac{f}{2} - f_1)\, df_1 \end{aligned} \tag{4.4}$$

Equation (4.4) indicates that all the information contained in the bicoherence is represented in the $QNLPI(f)$ which is function in one variable, f. Moreover, the $QNLPI(f)$ inherits useful characteristics from the third order statistics, bicoherence, such as high capability of nonlinear-systems identifications, high immunity to additive gaussian noise, and amplification invariance. Furthermore, it can be proven that $QNLPI(f)$ is theoretically bounded between zero and one ($0 \leq QNLPI(f) \leq 1$) as shown in the following section. Zero value of $QNLPI(f)$ means that no quadratic-nonlinearity produces any power at this frequency, while one means all the power at frequency f result from quadratic-nonlinearity.

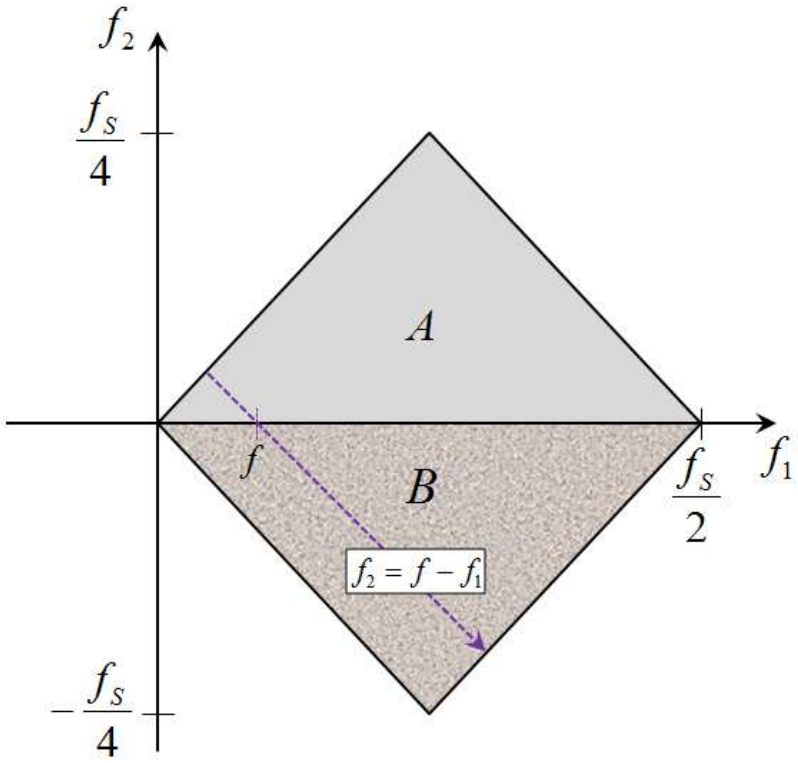

Figure 4.1 Region of computation (ROC) for the proposed $QNLPI(f)$ assuming aliasing is absent: triangle "A" is the conventional ROC for the bispectrum/bicoherence, region "$A - B$" is used to calculate the proposed $QNLPI(f)$, and dashed line indicates the direction of integration

4.4 Boundary Limits of $QNLPI(f)$

Assume that the signal at frequency m, $X(m)$, is constructed from finite number of quadratic coupling pairs plus non-quadratic coupling part as shown in equation (4.5).

$$X(m) = \sum_{\forall l+k=m} A_{l,k}\, X(l)X(k) + X'(m) \tag{4.5}$$

where $A_{l,k}$ is the coupling coefficient between two frequencies l and k to produce sum frequency m. $X'(m)$ represents any non-quadratic coupling power in the signal, either independent excitation or from other higher order interactions. Assuming that $x(t)$ is a zero-mean wide-sense stationary random signal, the mean square power at frequency m, $P_x(m)$, can be proven to be as follows [35];

$$P_x(m) = \sum_{(\forall\, l+k=m)} |A_{l,k}|^2\, E\{|X(l)X(k)|^2\} + E\{|X^{'}(m)|^2\} \tag{4.6}$$

First part of equation (4.6) represents the total power at frequency m due to all quadratic coupling pairs, while the second part is due to any non-quadratic-coupling power at this frequency. Substituting from equation (4.2) in equation (4.4),

$$QNLPI(m) = \int_0^{f_s/4} \frac{|E\{X(\frac{m}{2}+f_1)X(\frac{m}{2}-f_1)X^*(m)\}}{P_x(m)\cdot E\{|X(\frac{m}{2}+f_1)X(\frac{m}{2}-f_1)|^2\}}\, df_1 \tag{4.7}$$

Then, from equation (4.5) in equation (4.7) recalling properties of expected value operator, we get the following equation:

$$QNLPI(m) = \frac{1}{P_x(m)} \int_0^{f_s/4} \left(\frac{|A+B|^2}{C}\right) df_1 \tag{4.8}$$

where,

$$A = \sum_{\forall\, l+k=m} A_{l,k}\, E\left\{X(\frac{m}{2}+f_1)X(\frac{m}{2}-f_1)X^*(l)X^*(k)\right\}$$

$$B = E\left\{X(\frac{m}{2}+f_1)X(\frac{m}{2}-f_1)X^{'*}(m)\right\}$$

$$C = E\left\{|X(\frac{m}{2}+f_1)X(\frac{m}{2}-f_1)|^2\right\}$$

The value of the expected value operators in the numerator of equation (4.8) will be zero except when variable f_1 equals to $f_1 = \frac{m}{2} - l = \frac{m}{2} + k$. Therefore, integration in equation (4.8) is reduced to summation as follows:

$$QNLPI(m) = \frac{\sum\limits_{\forall l+k=m} |A_{l,k}|^2 E\{|X(l)X(k)|^2\}}{P(m)} \tag{4.9}$$

Note that numerator of equation (4.9) represents the total power at frequency m due to all quadratic coupling pairs and it is fraction of $P_x(m)$ as shown before in equation (4.6). Hence, the proposed index, $QNLPI(m)$, measures the fraction of the

mean square power at frequency m due to quadratic coupling between all combination of frequencies that possibly result in m. Also, from (4.9), $0 \leq QNLPI(m) \leq 1$, and will equal one if, and only if, $X^{'}(m) = 0$.

4.5 Digital Computation of $QNLPI(f)$

The same procedure described in [35] can be followed in order to calculate digital bicoherence talking into consideration the modified region of computations described before in Figure 4.1 to separate and account for both positive and negative parts of frequency interactions. Next, digital computation of the $QNLPI(f)$ can be carried out by replacing integration in (4.4) by summation as shown in (4.10).

$$QNLPI(f) = \sum_{n=0}^{n=\frac{N}{2}-1} b^2_{xxx}((\frac{f}{2} + n\Delta f), (\frac{f}{2} - n\Delta f)) \tag{4.10}$$

where Δf is the elementary band width determined from the resolution of DFT calculation. $\Delta f = f_N/N$, $f_N = f_S/2$, and N is the number of points used in DFT calculation. The frequency resolution Δf should be smaller than the difference between the smallest two frequencies expected to interact in any particular case.

4.6 Quadratic-Nonlinear Power Spectral Density, $P_{QNL}(f)$

As discussed in section 2.2, power spectral density $P_{xx}(f)$ is the Fourier transform of the auto-correlation function $R_{xx}(\tau)$ for a stationary random process $x(t)$ according to Wiener-Khintchine theorem [33], [34]. Thus, it can be estimated using the following equation:

$$P_{xx}(f) = E\{X(f)X^*(f)\} = E\{|X(f)|^2\} \tag{4.11}$$

$P_{xx}(f)$ has the dimensions of mean square values/Hz and it indicates how the mean square value is distributed over frequency.

Based on the proposed $QNLPI(f)$ index discussed in the preceding subsection, one can estimate how much of the mean square power at certain frequency is generated due to the second order nonlinearity by multiplying the $QNLPI(f)$ index at this frequency by the power spectral density $P_{xx}(f)$, as follows:

$$P_{QNL}(f) = QNLPI(f) \cdot P_{xx}(f) \tag{4.12}$$

where $P_{QNL}(f)$ is the nonlinear power spectral density showing the distribution of quadratic-nonlinearly-generated mean square power over frequency, and it also has the dimensions of mean square values/Hz. Thus, integration of $P_{QNL}(f)$ over the whole range of frequencies estimates the total quadratic nonlinear power contained in the signal. It would be also useful to quantify the percentage of quadratic nonlinear power ($PQNLP$) to the total mean square power as follow:

$$PQNLP = \frac{\sum_{n=0}^{N-1} QNLPI(n\Delta f) \cdot P_{xx}(n\Delta f)}{\sum_{n=0}^{N-1} P_{xx}(n\Delta f)} \tag{4.13}$$

where denominator in equation (4.13) estimates the total power in the signal while the numerator estimates the overall quadratic nonlinear power. $PQNLP$ is a single-value metric that is useful in monitoring the severity of nonlinear behavior of the signal under study which can be used to monitor fault-progress, as will be shown in section 4.9.

4.7 Numerical Example of $QNLPI(f)$

Before we apply the proposed indices to study nonlinear coupling in real world vibration data, we will use simple signal to illustrate the usefulness of these metrics and help understand the physical interpretation of their values. Thus, a computer-generated test signal has been used as shown in equation (4.14).

$$x(t) = A_b \cos(2\pi f_b t + \theta_b) + A_c \cos(2\pi f_c t + \theta_c) + A_e \cos(2\pi f_e t + \theta_e)$$
$$+A_g \cos(2\pi f_g t + \theta_g) + A_{bc} \cos(2\pi f_b t + \theta_b) \times \cos(2\pi f_c t + \theta_c)$$
$$+A_{eg} \cos(2\pi f_e t + \theta_e) \times \cos(2\pi f_g t + \theta_g) + A_d \cos(2\pi f_d t + \theta_d) \quad (4.14)$$

where $A_b = A_c = A_d = A_e = A_g = 2, A_{bc} = A_{eg} = 4$, sampling frequency $f_s = 2f_N = 4.8$ kHz, $f_b/f_N = 0.22, f_c/f_N = 0.375, f_e/f_N = 0.292, f_g/f_N = 0.303$ and $f_d = f_b + f_c = f_e + f_g$. All the phases are independently taken from a set of uniformly distributed random numbers.

In this testing signal $x(t)$, the total power at f_d is a share of three equal source; the independent excitation, the quadratic nonlinear interaction between f_b and f_c, and the quadratic nonlinear interaction between f_e and f_g. The power spectrum of the test signal, the modified bicoherence $b^2_{xxx}(f_1, f_2)$, the quadratic-nonlinearity power-index $QNLPI(f)$, and the quadratic-nonlinear power spectrum $P_{QNL}(f)$ are shown in Figure 4.2.

From Figure 4.2-(b), $b^2_{xxx}(f_c, f_b) = 0.324$, and $b^2_{xxx}(f_g, f_e) = 0.329$ are lined up on the same $f_1 + f_2 = f_d$ axis. This means that each group contributes to the quadratic-nonlinearity power-index in Figure 4.2-(c) by approximately one third. $b^2_{xxx}(f_g, -f_e) = 1$ and $b^2_{xxx}(f_c, -f_b) = 1$ lie in the "B" zone of the modified bicoherence and represent the negative part of the interaction for both $f_c - f_b$ and $f_g - f_e$. The detailed bicoherence spectrum in Figure 4.2-(b) is represented by the $QNLPI(f)$ in Figure 4.2-(c). $QNLPI(f_d) = 0.653$ which means that two-thirds of the total power at frequency f_d is coming from quadratic-nonlinear interaction between different frequencies. The power spectral contents that generated only by quadratic nonlinearity are separated in the $P_{QNL}(f)$ as shown in Figure 4.2-(d). Percentage of quadratic nonlinear power, $PQNLP$, is estimated and found to be = 42.93%.

(a)

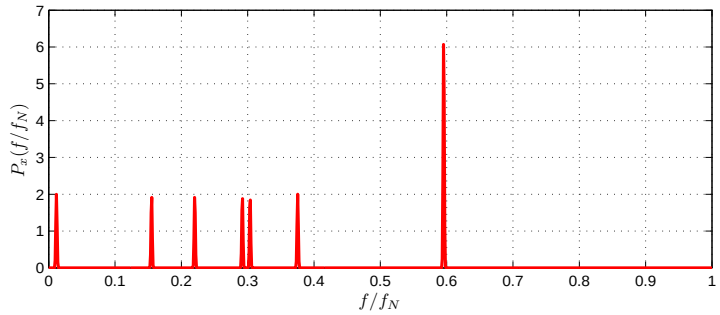

(b)

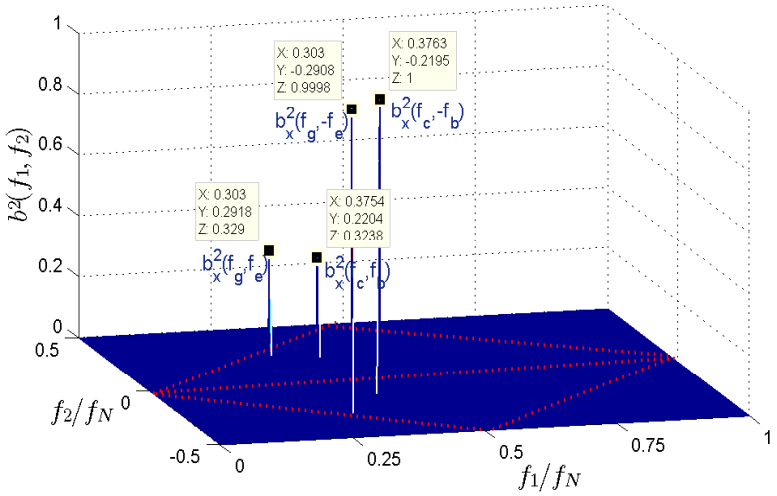

(c)

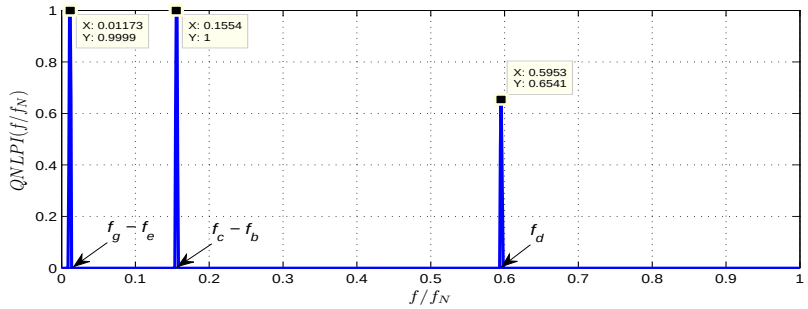

(d)

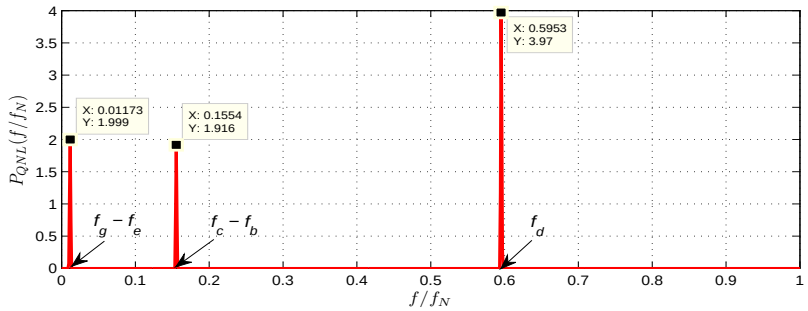

Figure 4.2 (a) Power spectral density, (b) Modified bicoherence, (c) QNLPI, and (d) Quadratic-nonlinear power spectral density; for test signal in (4.14)

4.8 Application of $QNLPI(f)$ in Health Assessment of Helicopter's Tail-Rotor Drive-Shafts

Focus of this study is centered on studying different combinations of drive-shafts faults using both conventional power spectral density (PSD) and the proposed $QNLPI(f)$. Shafts numbered 3-5 in Figure 1.5-(a) operate at a rotation speed of 4863 RPM (81.05Hz) corresponding to full-speed of shaft rotation on the fielded rotorcraft, as shown in the schematic in Figure 4.3. The vibration signals denoted as FHB and AHB, measured at forward and afterward hanger bearings respectively, are gathered at two minutes intervals at a sampling rate of 48 kHz over the course of thirty minute test runs. The measurements are taken for different drive-shafts setting under test which include baseline shaft and bearing configuration, unbalance in different shafts configuration, and shaft misalignment, all common issues on AH-64 drivetrains. Misalignment of the shafts is studied at 1.3° between drive-shafts #3 and #4, 1.3° between drive-shafts #4 and #5. Unbalance is studied at drive-shafts #3, #4 and #5 by 0.140 oz-in, 0.135 oz-in 0.190 oz-in respectively. Different combination of misalignment and unbalance are tested as summarized previously in Table 3.1.

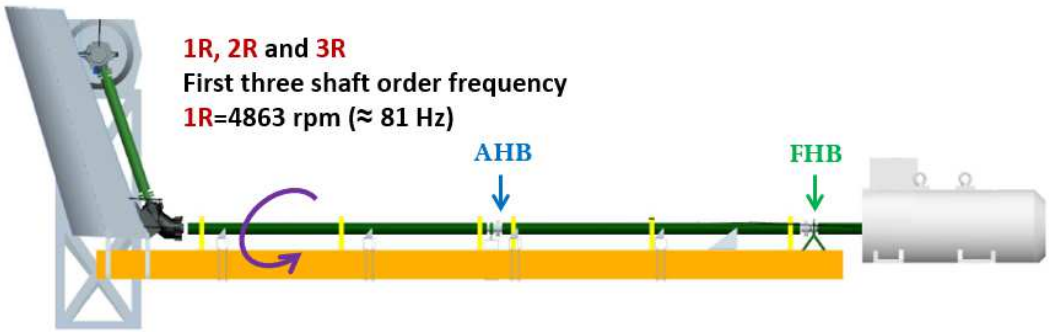

Figure 4.3 Schematic of the TRDT test stand at USC

Due to the loading scheme of the TRDT test stand with the intermediate gear box (IGB) and the output motor torque, the 3^{rd} harmonic of the tail rotor drive shaft (243 Hz) is dominating the power spectrum of the AHB vibrations in the studied

cases with some other different harmonics in each setting, as shown in Figures 4.4 and 4.5. The power spectra of the baseline (00321) and the misaligned (20321) cases in Figure 4.4 have the same dominating spectral peaks with very slight changes in the minor peaks. A similar situation occurs when we compare the unbalanced (10321) and the misaligned-unbalanced (30321) cases in Figure 4.5. It is not an easy task to distinguish between different cases by looking at the whole power spectrum.

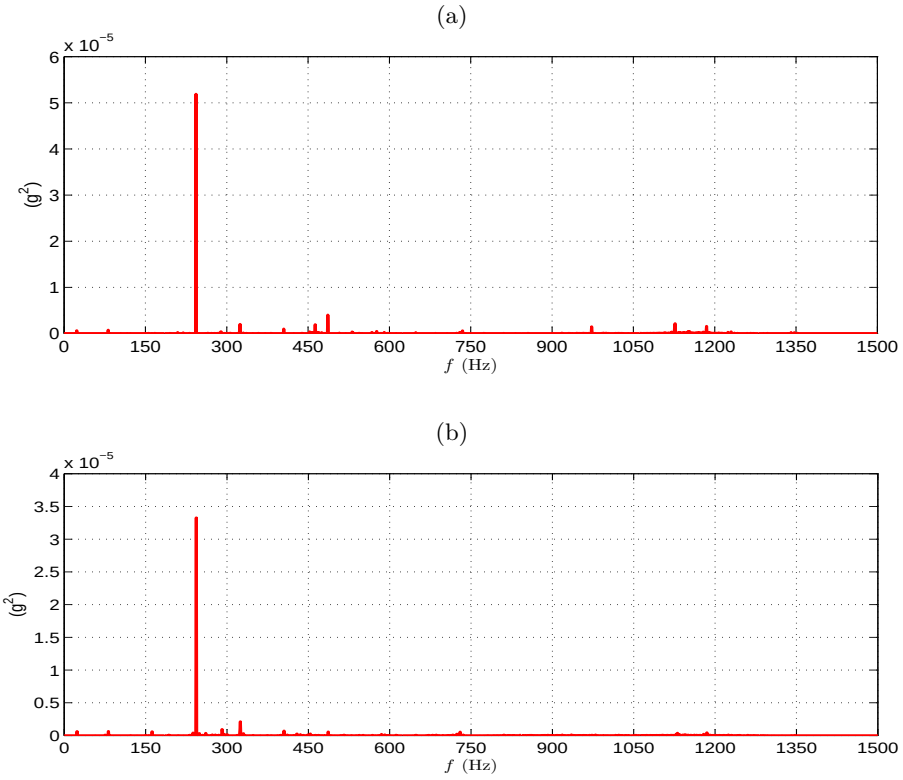

Figure 4.4 Power spectral density of the AHB: baseline (00321) in (a), and misaligned (20321) in (b)

Conventional PSD comparison with the baseline is usually done on a logarithmic amplitude scale with increases of 6-8 dB considered to be significant and changes greater than 20 dB from the baseline considered serious [42]. Table 4.1 summarizes the results of the spectral peak comparison of the three faulted cases (10321, 20321, and 30321) with the baseline case (00321) in terms of the first three spectral peaks (SP1, SP2, and SP3) of the faulted drive-shafts (first three harmonics of the shaft rotating speed (81Hz, 162Hz and 243Hz)). As shown in Table 4.1, values of the

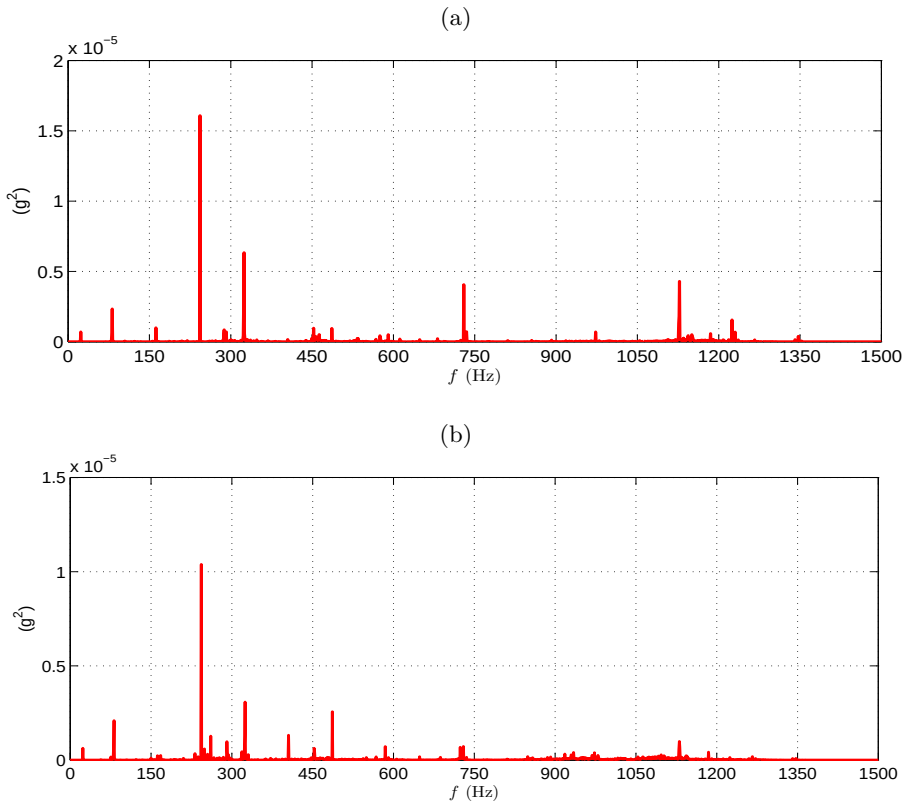

Figure 4.5 Power spectral density of the AHB: unbalanced (10321) in (a), and misaligned-unbalanced (30321) in (b)

SP2 for all faulted cases exceed the 6 dB threshold compared to the baseline and therefore it provides a good indicator for all of the three faulted cases. In fact, SP2 is currently employed in the HUMS system to detect unbalanced and/or misaligned shafts in a tail rotor drive-train of a rotorcraft [38]. However, this Condition Indicator (CI) has limited diagnostic capabilities in specifying whether the fault is unbalance, misalignment or a combination of both faults. The maintainers are told to check for more than one source that might cause that CI to exceed its limit.

Table 4.1 Comparison with baseline case in terms of SP1, SP2, and SP3 (dB)

	A/UB(10321)	MA/B (20321)	UB/MA(30321)
SP1	5.311	-0.081	4.799
SP2	9.997	10.255	8.661
SP3	-2.001	-2.0667	-8.141

The vibration data is then investigated using the proposed $QNLPI(f)$ discussed in section 4.3. Figure 4.6-(a) shows $QNLPI(f)$ spectrum for the baseline case for which nonlinearly-generated frequencies located at 1^{st} and 7^{th} harmonics of the drive-shaft with values 0.68 and 0.77, respectively. These values can be result of interaction between the dominating 3^{rd} harmonic with the 4^{th} to produce 68% and 77% of the power at 1^{st} and 7^{th} harmonics, respectively. The remaining fraction of the power may be independently excited or coming from other forms of nonlinearities.

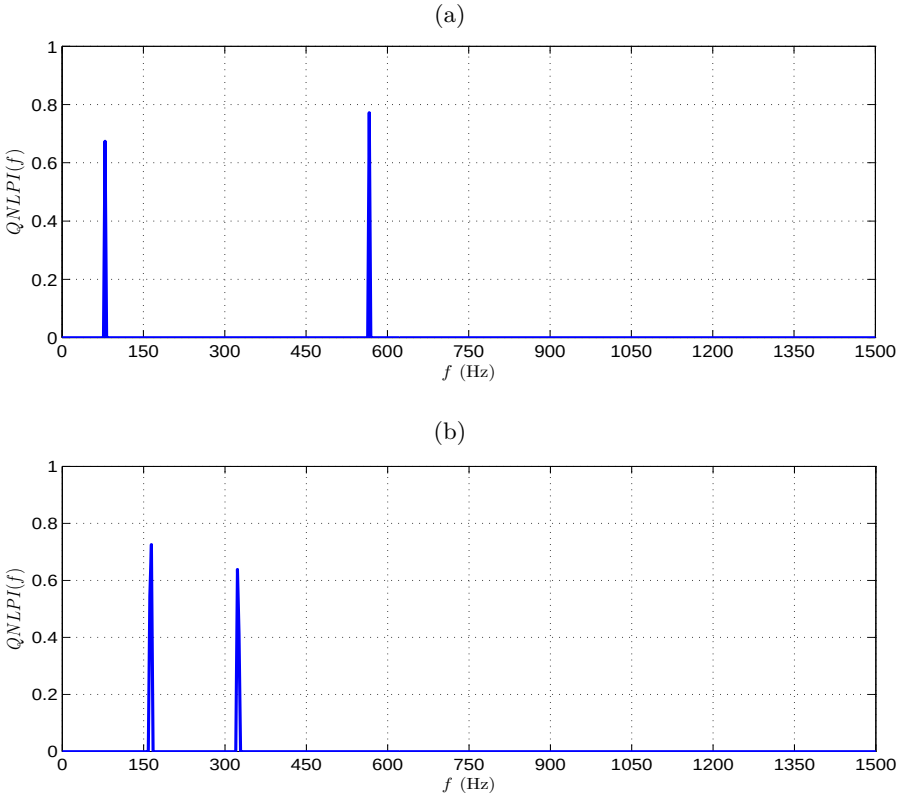

Figure 4.6 $QNLPI$ of the AHB: baseline (00321) in (a), and misaligned (20321) in (b)

Due to different experimental settings, different interaction pattern exists in the case of misalignment as shown in Figure 4.6-(b). In this case, quadratic nonlinear interaction between the 3^{rd} and the 1^{st} harmonics is dominating. As a result of this interaction, 2^{nd} and 4^{th} harmonics are generated with power fraction of 0.72 and 0.64, respectively. The results in Figure 4.6 give us more details about the content of the

power spectrum of the signal. Some frequencies in common between the baseline and misaligned cases have different origins. For example, the 1^{st} and the 4^{th} harmonics exchange there places as sourc/result of the interaction process with the 3^{rd} due to different physical setting of the rotating shaft.

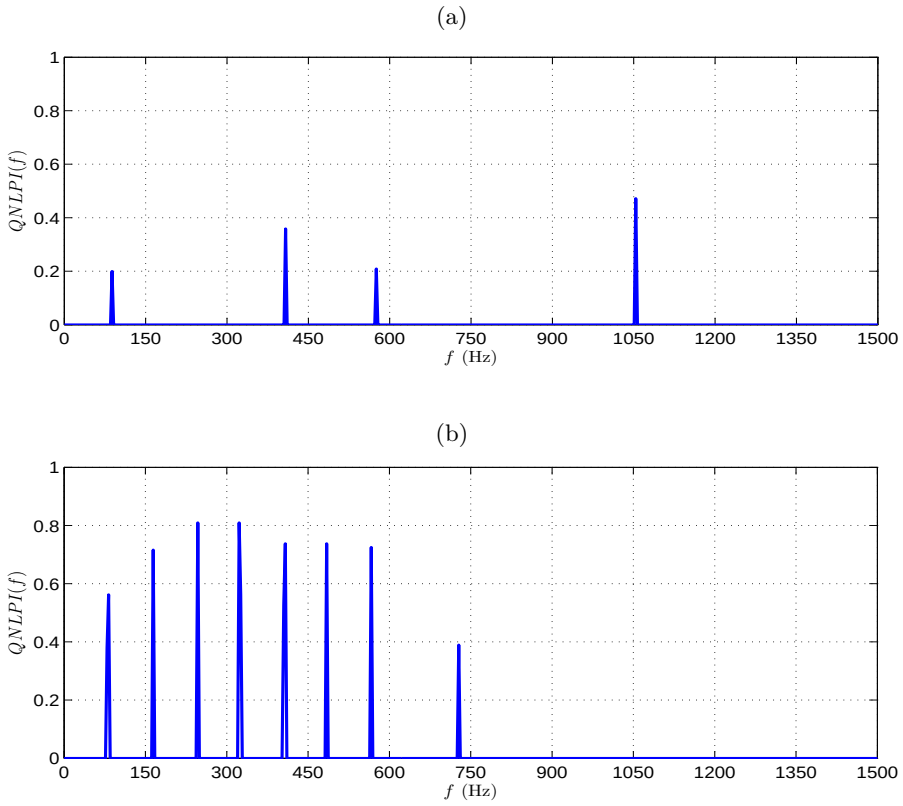

Figure 4.7 QNLPI of the AHB: unbalanced (10321) in (a), and misaligned-unbalanced (30321) in (b)

Comparing the $QNLPI(f)$ of the unbalance case shown in Figure 4.7-(a) with the baseline case in Figure 4.6-(a), we can see a slightly more interaction introduced in the case of the unbalance. The 4^{th} harmonic interacts with both 3^{rd} and 9^{th} producing a series of odd harmonics at 1^{st}, 5^{th}, 7^{th}, and 13^{th}. The increasing production of odd harmonics through the nonlinear interaction is likely a sign of unbalance. On the other hand, as discussed above, the production of even harmonics is likely a sign of misalignment. Thus, when a combination of unbalance and misalignment is introduced to the drive-shafts, one can expect that nonlinearity of the system will

increase so that a variety of odd/even harmonics of the drive shaft rotating frequency is produced as shown in Figure 4.7-(b).

From the discussion above, we can see that beside conventional power spectral density analysis, using $QNLPI(f)$ spectrum helps to gain more details about non-linear harmonic interaction/generation patterns, which can be used to distinguish between different fault settings of the tail rotor drive-shafts.

4.9 Application of $QNLPI(f)$ to Study Progress of Gearbox Fault

In this section, we use vibration data collected in the experimental TRDT test stand to study tail-rotor gearbox failure (denoted TRGB in Figure 1.5) due to lubrication starvation [62]. This experiment was originally designed to demonstrate whether or not a gearbox with a leaking output seal could be used in the filed until the aircraft reached a phase inspection, which currently occurs every 250 hours. The output seals were seeded to represent a worst-case scenario leak for gearboxes, as shown in Figure 4.8.

For all the tested articles, it was observed that a persistent grease leak through the output seal resulted in a loss of lubricant in the main gear compartment. Consequently, this condition ultimately resulted in lubricant starvation on the gear meshing region and catastrophic gear teeth failures, as shown in Figure 4.9. One interesting finding of this experiment was that gearbox can survive more than 480 hours after fault seeding for all tested articles.

The secondary objective of the experiment was to identify vibration signatures which might indicate the impending failure. Here, we use vibration data collected from this experiment to illustrate the usefulness of the proposed index in keeping track of the progress of fault in the gearbox.

(a)

(b)

(c)

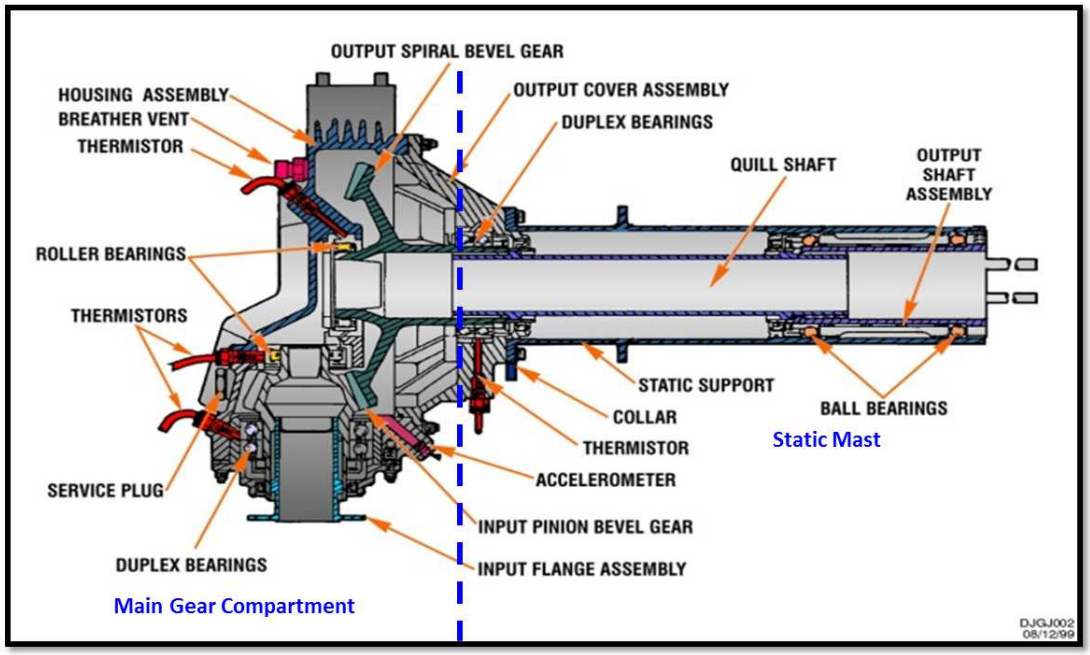

Figure 4.8 TRGB experiment setup: (a) actual TRGB, (b) seeded fault showing removal of the output seal material, and (c) schematic of the TRGB showing the location of the seeded fault

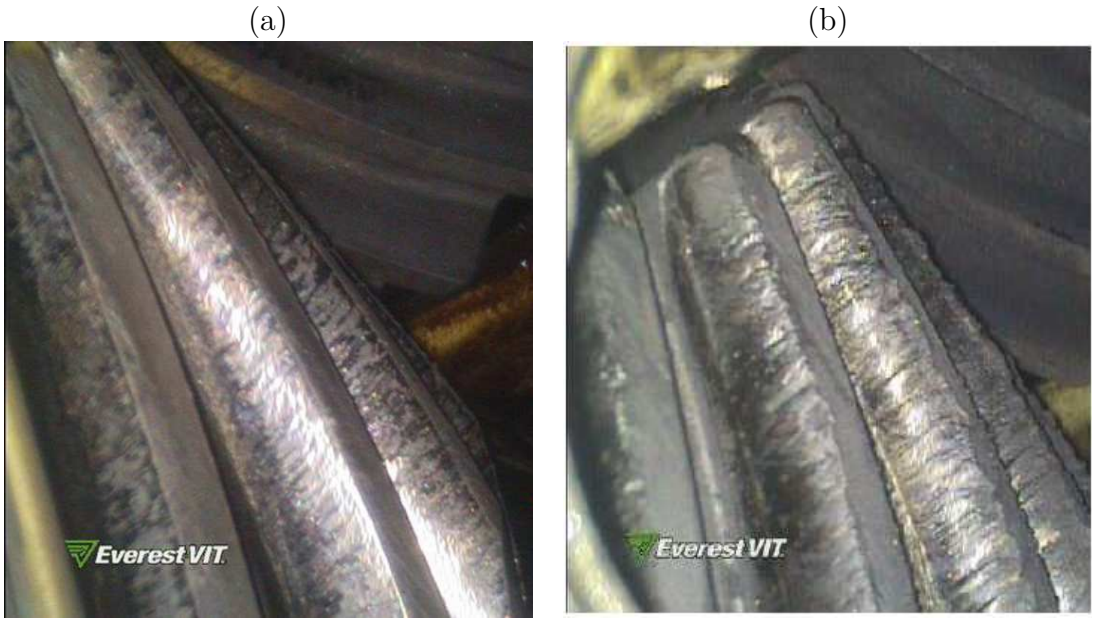

Figure 4.9 Borescope picture showing input gear teeth: (a) earlier stage of testing, and (b) after failure [62]

Figure 4.10 shows how the average power spectral density (PSD) of the gearbox vibration changes during the last four days before failure. Inspection of the PSD plots indicates that it was not until the day of failure that vibration power at the third and fourth harmonics of the gear mesh frequency (1334Hz) increased suddenly to warning values, as shown in Figure 4.10-(d). During the last three days preceding the failure, shown in Figure 4.10-(a) $\sim$ (c), PSD stayed almost the same with slightly monotonic increase of vibration power at the both first and second harmonics of the gear mesh frequency.

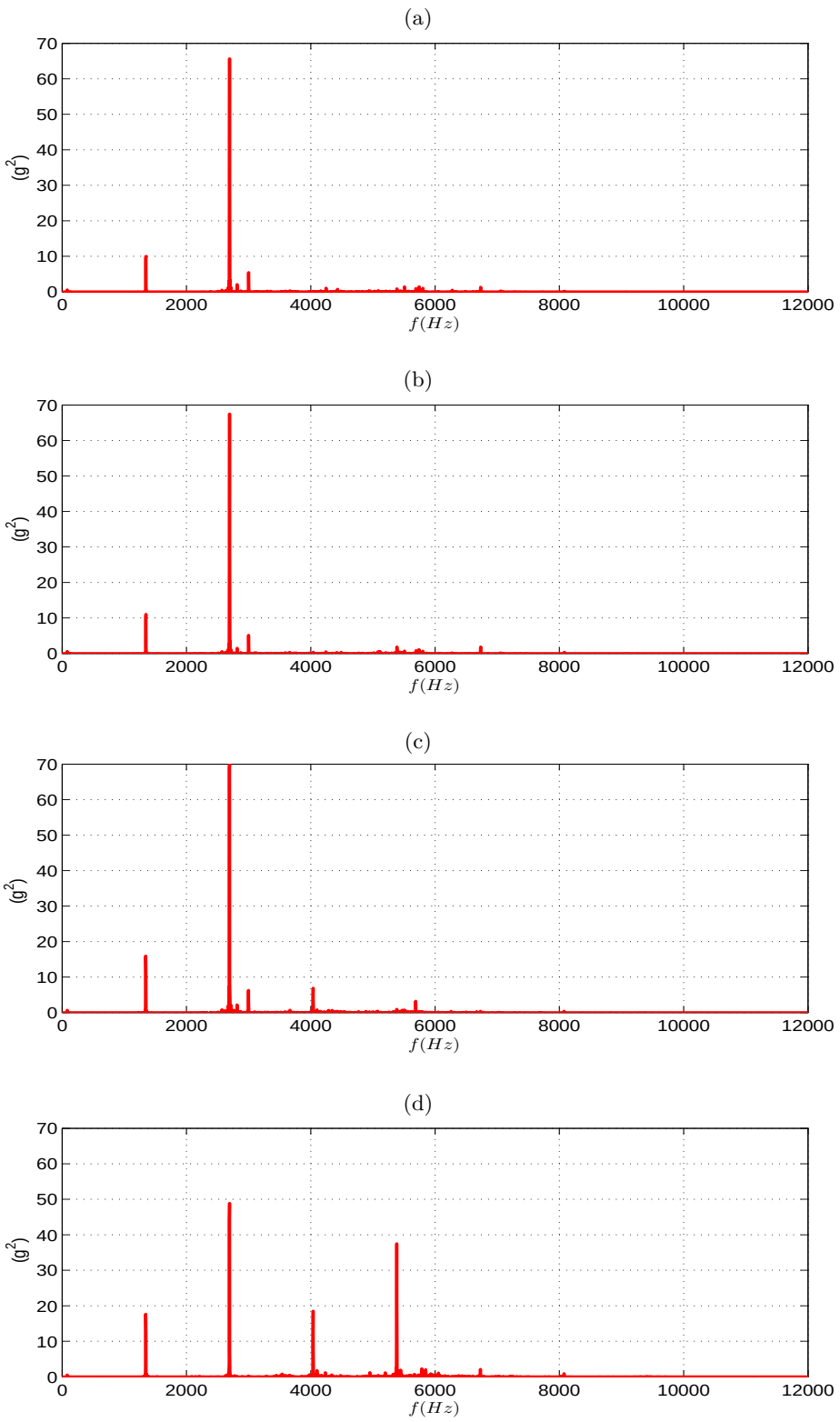

Figure 4.10 Progress of power spectral density (PSD) change during gear teeth failure: (a) 3 days before failure, (b) 2 days before failure, (c) 1 days before failure, and (d) same day of failure

Progress of failure developed in the gearbox is studied using the proposed $QNLPI(f)$, as shown in Figure 4.11-(a) $\sim$ (d), for the same vibration data set which studied previously in Figure 4.10. Figure 4.11-(a) shows the $QNLPI(f)$ of gearbox vibration three days before gearbox failure which has the least quadratic-nonlinearly produced frequencies with only first, third, and fifth mesh harmonics having $QNLPI$ equal to 1, 1, and 0.33, respectively. Two days before failure, vibration nonlinearity increased causing the values of $QNLPI$ at the pre-exist harmonics to increase, and more nonlinearity to show up at the second and sixth harmonics, as seen in Figure 4.11-(b). The highest nonlinearity in the vibration signal is exist one day before failure as shown in Figure 4.11-(c). On that day, beside the high nonlinearity at all the first six harmonics of the TRGB, gear mesh frequency of the intermediate gearbox (IGB), 3000 Hz, shows up interacting with several TRGB harmonics. This IGB frequency disappeared in the day of failure from the $QNLPI(f)$ spectrum, but all gear mesh harmonics of the faulted TRGB stayed at high nonlinear power values, as shown in Figure 4.11-(d). This consistent increase in the nonlinear production/coupling of gear meshing harmonics, regardless of there power spectral values, can be used as precocious indication of gear-teeth failure.

In order to describe the progress of fault in the gearbox using single-valued metric, percentage of quadratic nonlinear power ($PQNLP$) in equation (4.13) is employed. Figure 4.12 compares the progress of the $PQNLP$ to other condition indicators during the last four days of experiment. The $1GMF$ and $2GMF$ are the vibration spectral peaks at the first and the second harmonics of the gear mesh frequency. The root-mean-square (RMS) and the energy-ratio (ER) condition indicators are calculated as reported in [21] to describe heavy gear wear.

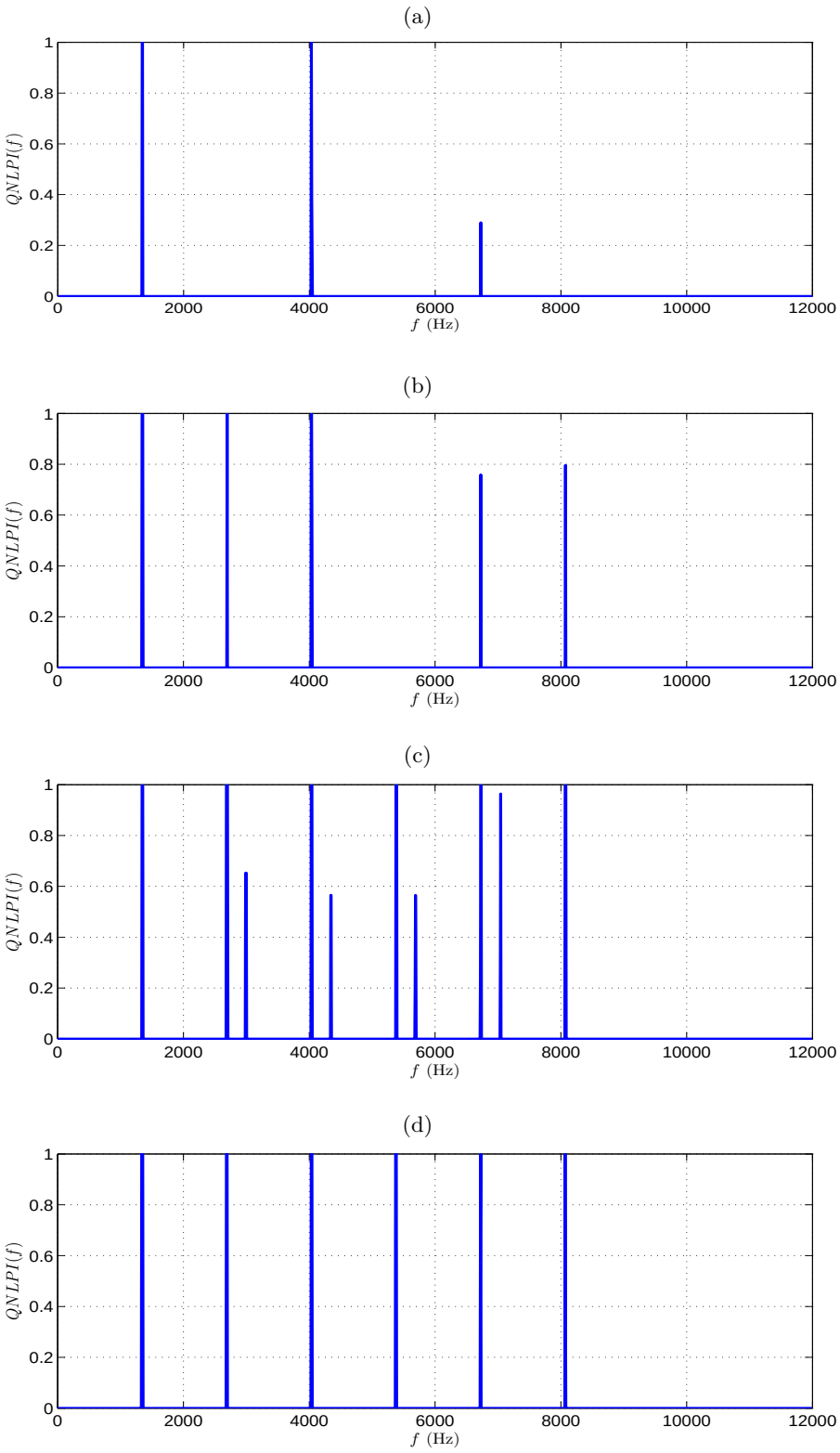

Figure 4.11 Progress of nonlinear harmonic generation due to gear teeth failure: (a) 3 days before failure, (b) 2 days before failure, (c) 1 days before failure, and (d) same day of failure

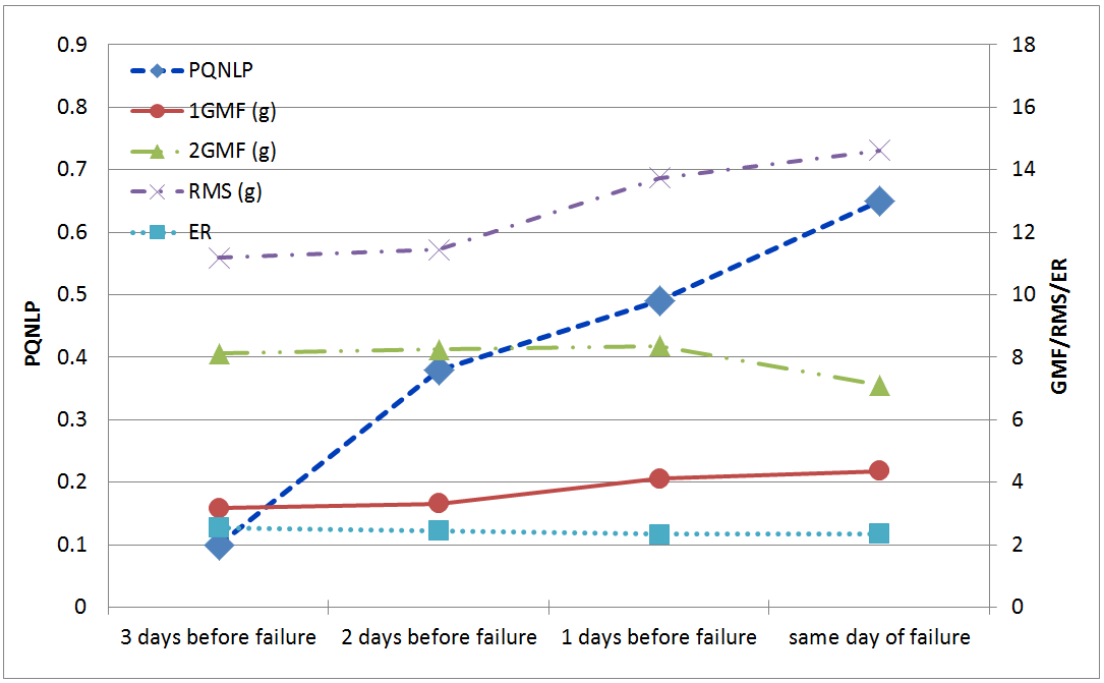

Figure 4.12 Trend of vibration $PQNLP$ compared to different condition indicators for the faulted TRGB during the last four days before failure

As shown in Figure 4.12, the value of $PQNLP$ starts showing considerable increase one day before other condition indicators. It is consistently climbing up until the gearbox failure due to wear in the input gear teeth which physically can be interpreted as increased vibration power due to highly-nonlinear rotating medium. Thus, this trend can be used as precocious indication of failure. The advantage of using $PQNLP$ as condition indicator over conventional power spectrum indicators is the inherent characteristics of HOS-based metrics as amplification invariance and high immunity to additive Gaussian noise, which reduce the dependency on the characteristics of the sensor used to collect the vibration data.

4.10 Conclusion

In this chapter, the quadratic-nonlinearity power-index ($QNLPI(f)$) has been proposed which provides a summary of the nonlinearity information contained in the the

3D bicoherence into 2D spectrum presenting an easier way to studying third-order statistic of signals.

The proposed index has been used to study real-world vibration data collected from tail-rotor drive train of an AH-64D helicopter. Two case studies have been conducted. In the first case, $QNLPI(f)$ has shown better diagnostic capabilities in differentiating between different drive-shaft faults by showing how different physical settings affect the nonlinear generation of harmonics. In the second case, $QNLPI(f)$ has shown better capability in detecting gearbox failure. For easier monitoring of the fault-progress in the gearbox, percentage of total quadratic nonlinear power ($PQNLP$) has been calculated based on the proposed $QNLPI(f)$ and has shown consistent increase during the gear fault aging. This single-valued metric can be used in prognostic models to estimate the remanding useful life of mechanical components.

Chapter 5

Condition Assessment of Faulted Hanger Bearing in Multi-Faulted Drivetrain System

In this chapter, hanger bearing faults are studied in the presence of more than one simultaneous drive-shaft faults using the proposed $QNLPI(f)$ and bicoherence analysis.

5.1 Introduction

Most of the conventional fault analysis techniques assume that a defect occurs in a rotating element separately, that we can identify this fault by the characterizing frequency of that component. For example, ball pass frequency inner-race rotating frequency (BPFI) is used to detect faults in the inner race of bearings [63]. However, it is not easy to detect bearing faults when it is combined with shaft faults, as will be discussed later in this chapter. In the presence of drive-shaft faults, shaft harmonics dominate the power spectra of the vibration signals collected form the faulted hanger-bearing making it hard to detect bearing's faults. Also, spectral interaction between different fault frequencies leads to unexpected frequencies to appear in the vibration spectrum which can not be explained using conventional power spectral analysis. However, bispectral analysis tools not only detect the bearing's faults in this extreme case of multi-faulted components, but also are able relate all frequencies to their root causes and successfully links the signal processing to the physics of the underlying faults.

HOS analysis has been previously used in analyzing harmonic vibration interaction patterns for different combination of shaft misalignment and unbalance with good (healthy) hanger bearing. In this chapter, two different hanger bearing faults are analyzed under typically misaligned-unbalanced shafts. Experiment setup is described in section 5.2 and results are then discussed in sections 5.3 and 5.4.

5.2 Experimental set up and data description

Seeded hanger bearing faults experiment was designed to include multi-faulted drive train components with two faulted hanger bearings running at the same time, one with a spalled inner race in the FHB position and one with contaminated grease with coarse grit sand run in the AHB position [64], as illustrated in Figure 5.1. This is done with 1.3° misalignment between drive shafts #3 and #4, 1.3° misalignment between drive shafts #4 and #5, and unbalanced drive shafts #3, #4 and #5 by 0.140 oz-in, 0.135 oz-in 0.190 oz-in respectively. The forward hanger bearing is machined to replicate a bearing with a spalled inner race as shown in Figure 5.3. All machining was done at the army research laboratory (ARL). The holes were milled into the inner race with a ball mill and were machined to the specs summarized in Table 5.1.

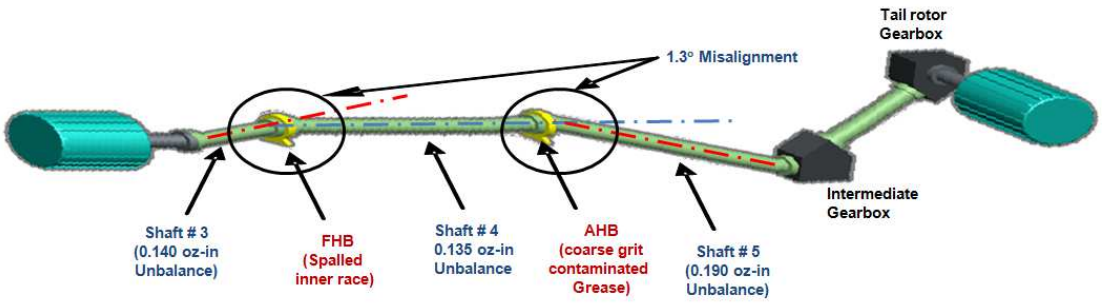

Figure 5.1 Schematic showing seeded hanger bearing faults experimental setup

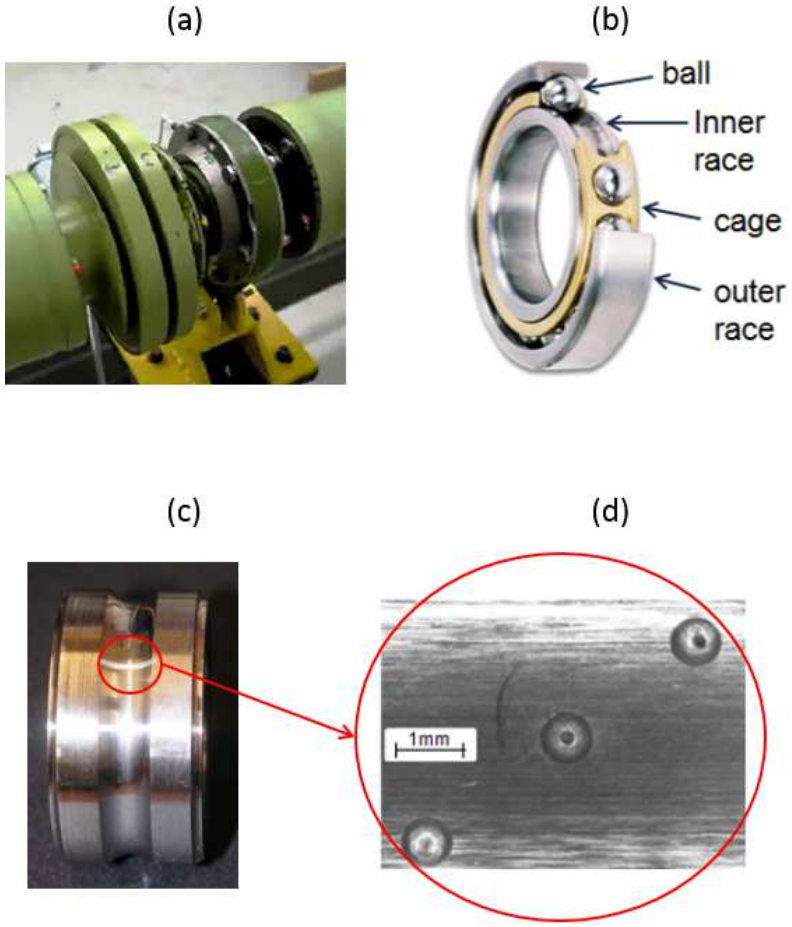

Figure 5.2 Faulted FHB: (a) assembled bearing in the drive train, (b) schematic of assembly components, (c) disassembled inner race, and (d) zoom in view of the spalled inner race fault

Table 5.1 Spalled inner race information in the FHB position

Spall	Spall diameter (inch)	Spall depth (inch)	Distance from left shoulder (inch)	Distance from right shoulder (inch)
#1	0.030	0.017	0.1400	0.2538
#2	0.031	0.016	0.1956	0.1985
#3	0.031	0.017	0.2567	0.1376

The AHB has coarse grit contaminated grease mixed in a ratio of 5% by volume of the grease. This seeded fault is also done at the ARL with a representative sand contaminant consist of crushed quartz with the total particle size distribution as shown in Table 5.2.

Figure 5.3 Faulted AHB: (a) assembled bearing, (b) zoom-in view of the coarse grit contamination

Table 5.2 Coarse grit contaminated grease mixture in the AHB position

Size (μ)	Volume fraction (%)
1	0.6 to 1.0
2	2.2 to 3.7
3	4.2 to 6.0
4	6.2 to 8.2
5	5.0 to 10.5
7	12.0 to 14.0
10	17.0 to 22.0
20	32.0 to 36.0
40	57.0 to 61.0
80	87.5 to 89.5
120	97.0 to 98.0
180	99.5 to 100
200	100

5.3 Spalled Inner Race Hanger Bearing

The power spectrum of the spalled inner race FHB is shown in Figure 5.4. It is estimated using average over ensemble of vibration data collected every two minutes over a 60 minutes run under output torque at the tail rotor equal to 111 lb-ft, and plotted with 1.465Hz frequency resolution. Due to the misaligned-unbalanced drive shafts, high magnitudes of the vibration exist at the 80.57Hz, 162.5Hz, and 243.2Hz as shown in Figure 5.4. These frequencies match 1SO , 2SO, and 3SO reported in Table 5.3 by the Aviation Engineering Directorate (AED). These shaft harmonics are typically used to describe shaft misalignment and unbalance by many vibration-analysis text-books [63], [65]. According to text books, one should also expect to see the ball pass inner-race frequency (BPFI) that characterizes the faulted hanger bearing under test, 441Hz as reported in Table 5.3. However, it is not easy to detect the BPFI frequency in Figure 5.4. The highest non-shaft frequencies in this spectrum is at 684.1Hz and 279.8Hz which do not match any frequency in Table 5.3. Therefore, it is obvious that linear spectral analysis fails to detect hanger bearing fault when it is combined with shaft faults, and also fails to relate all frequencies in the spectrum to known fault source.

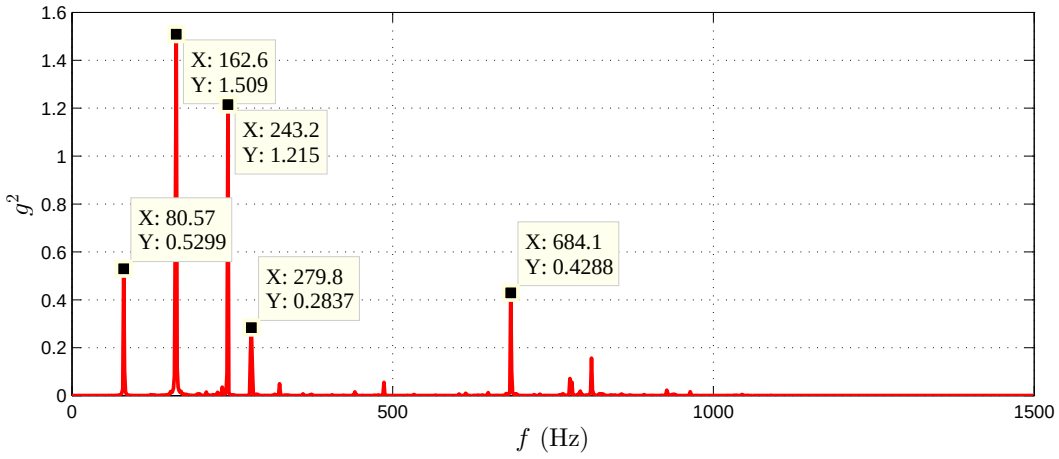

Figure 5.4 Power spectrum of the spalled inner-race FHB with misaligned-unbalanced shafts

Table 5.3 TRDT components rotating frequencies provided by AED

Source(s) or Meshing Components	Harmonic Number	Frequency Type	Frequency (Hz)	Frequency (RPM)
Hanger Bearings	1	CFF	31.95	1917
Hanger Bearings	2	CFF	63.90	3834
Driveshaft	1	SO	81.06	4863
Hanger Bearings	3	CFF	95.85	5751
Hanger Bearings	4	CFF	127.80	7668
Driveshaft	2	SO	162.11	9727
Hanger Bearings	1	BSF	182.89	10974
Driveshaft	3	SO	243.17	14590
Hanger Bearings	1	BPFO	287.55	17253
Driveshaft	4	SO	324.23	19454
Hanger Bearings	2	BSF	365.79	21947
Hanger Bearings	1	BPFI	441.96	26518
Hanger Bearings	3	BSF	548.68	32921
Hanger Bearings	2	BPFO	575.10	34506
Hanger Bearings	4	BSF	731.57	43894
Hanger Bearings	3	BPFO	862.65	51759
Hanger Bearings	2	BPFI	883.92	53035
Hanger Bearings	4	BPFO	1150.19	69012
Hanger Bearings	3	BPFI	1325.89	79553
Hanger Bearings	4	BPFI	1767.85	106071

The FHB vibration is then analyzed using the proposed $QNLPI(f)$ index discussed in Chapter 4. As discussed previously in section 4.8, due to unbalanced-misaligned drive shafts, nonlinearity of the system increases so that a variety of odd/even harmonics of the shaft frequency is produced, as shown in Figure 5.5. Beside shaft harmonics, $QNLPI(f)$ has high values corresponding to frequencies of 279.8Hz and 684.1Hz which do not match any fault frequencies, as stated above. This means that those two frequencies are generated due to quadratic nonlinear interaction between frequency components in the vibration spectrum. This part of the analysis answers the question of "why 279.8Hz and 684.1Hz exist in the FHB vibration spectrum?". However, summarized information in the $QNLPI(f)$ do not answer the question of "what is the original interacted frequencies that produce 279.8Hz and 684.1Hz?".

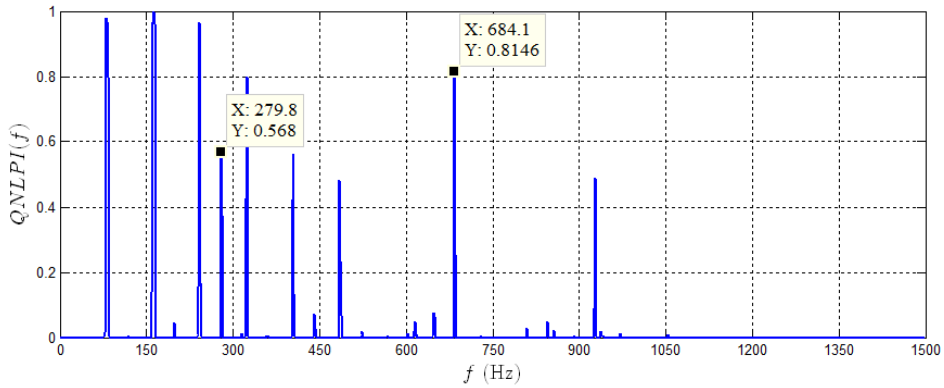

Figure 5.5 $QNLPI(f)$ of the spalled inner-race FHB with misaligned-unbalanced shafts

Therefor, In order to get more information to answer the above question, we utilize the original information in the bicoherence spectrum as shown in Figure 5.6. It can be seen that a number of shaft order harmonics exist along f_1= 161.1Hz, 243.2Hz, and 323.7Hz which nonlinearly interact with other frequencies in f_2 direction. Shaft harmonic interaction patterns is used in previous chapters to assess drive shaft health conditions. In our case here, we are concerned more about any interaction with *non-shaft* frequencies that might be related to hanger bearing faults. Two non-shaft frequencies are of interest here at bi-frequency points (440.9,243.2) and (440.9,-161.1), as shown in Figure 5.6. High bispectral peak at (440.9,243.2) explains that frequency 440.9Hz nonlinearly interacts with third harmonic of the shaft, 243.2Hz, to produce the sum value 684.1Hz. Also, high bispectral peak at (440.9,-161.1) explains that frequency 440.9Hz nonlinearly interacts with second harmonic of the shaft, 161.1Hz, to produce the difference value 279.8Hz. Since 440.9Hz is equal to BPFI in Table 5.3, this implies that a fault exists in the inner race of the hanger bearing.

From the above discussion, it is clear that $QNLPI(f)$ and bicoherence spectrum are more useful in both detecting the hanger bearing fault and giving better explanation about source of frequencies in the vibration spectrum.

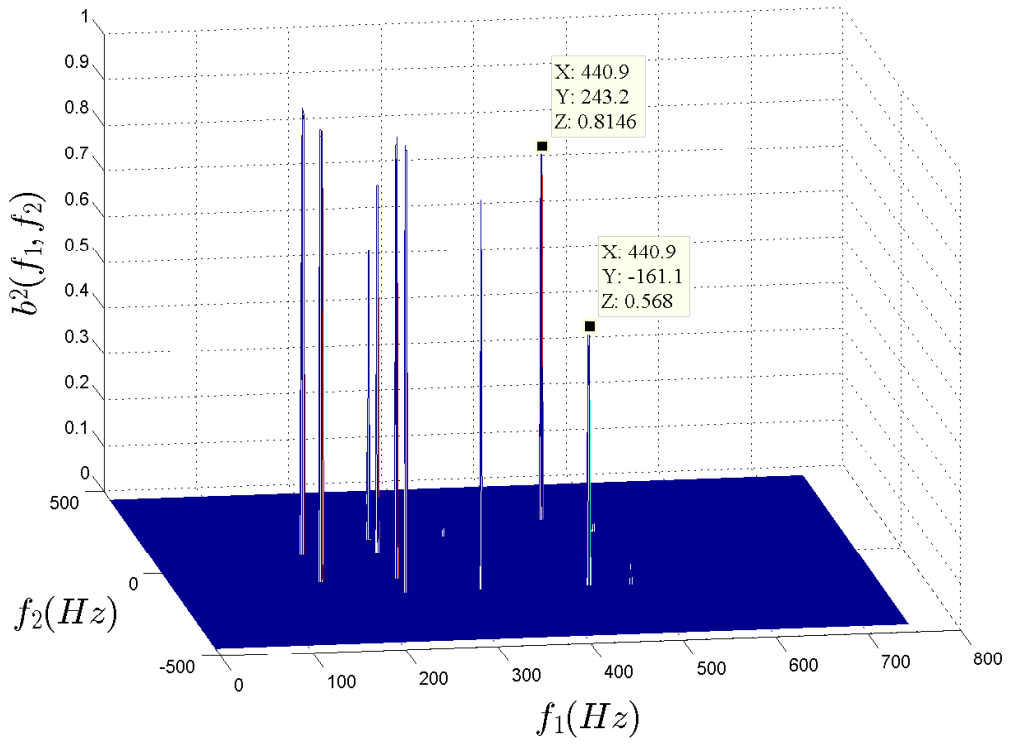

Figure 5.6 Bicoherence of the spalled inner-race FHB with misaligned-unbalanced shafts

5.4 Coarse Grit Contaminated Grease Hanger Bearing

The power spectrum of the coarse grit contaminated grease AHB is shown in Figure 5.7. This fault does not have particular frequency to characterize it in the power spectrum. Although it is clear from the high vibration magnitudes that there is a fault in this bearing, the power spectrum still can not explain the source of generating high vibration magnitudes at 279.8Hz, 360.4Hz, 440.9Hz, 522.9Hz, 603.6Hz, 684.1Hz, 927.2Hz, and some other higher frequencies, which are spaced by the shaft rotating frequency 80.57Hz. The only frequency that can be related to TRDT frequencies in Table 5.3 is 440.9Hz, the BPFI of the faulted inner-race FHB. This can be misleading because this hanger bearing has no fault in the inner race. Thus, more analysis may be needed to confirm whether or not the inner race of this bearing is faulted, and if not what is the source of the hight vibration power.

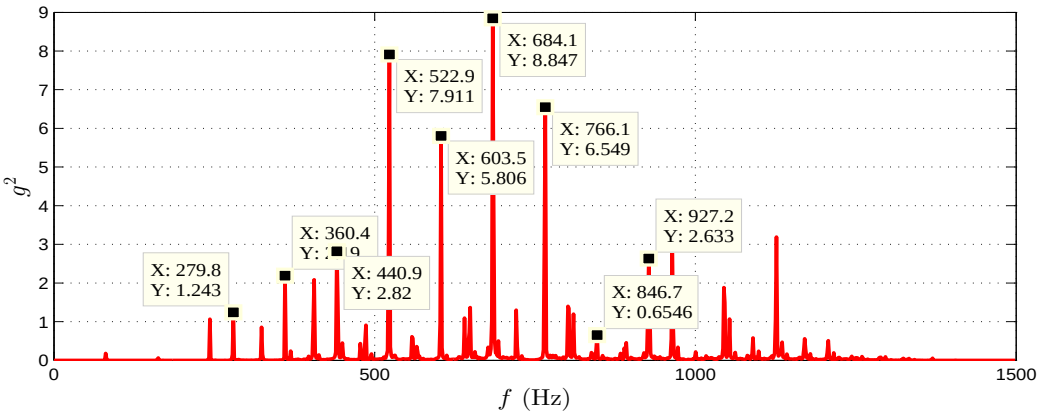

Figure 5.7 Power spectrum of the coarse grit contaminated grease AHB

For quick overview of the nonlinearity in the AHB, vibration collected from this bearing is analyzed using the proposed $QNLPI(f)$ index as shown in Figure 5.8. We can clearly observe the hight nonlinear-generation of frequencies all over the vibration spectrum including the BPFI and the shaft harmonics. However, it is still useful to study the bicoherence spectrum of the vibration for more information about original source interaction between vibration's spectral components

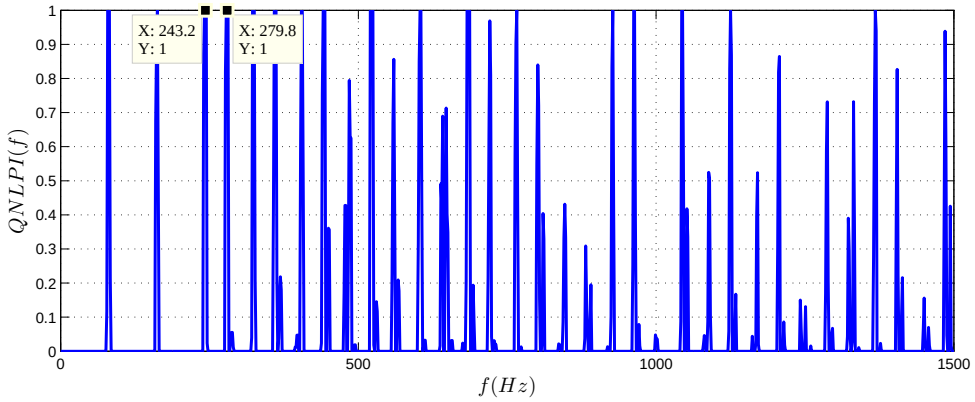

Figure 5.8 $QNLPI(f)$ of the coarse grit contaminated grease AHB

The bicoherence spectrum of the AHB vibration is shown in Figure 5.9 with vibration wave-wave interaction among a wide spread of shaft harmonics and non-harmonics frequencies. This indicates a very high nonlinear rotating medium that results in this large amount of interaction. Although it is hard to follow each coordinate point in the 3D bicoherence plot, we observe that there are particular frequencies over f_2 direction that interact with other frequencies, namely Shaft Orders 1SO, 2SO, 3SO, ...,8SO, and 279.8Hz, 360.4Hz, 440.9Hz, 522.9Hz, 603.6Hz, 684.1Hz. For a better view, bicoherence spectrum is projected along f_1 and f_2 axes, as shown in Figure 5.10. The trend of vibration interaction is clear that shaft harmonics tend to interact with the BPFI group that transferred from the FHB through drive shaft #4, with no other obvious source of interaction. The higher magnitude of the BPFI group of frequencies in the AHB spectrum in Figure 5.7 can be explained by multiple coordinate points of interaction in the bicoherence spectrum between shaft harmonics and frequencies generated at FHB that causes resonance at those frequencies. For example, 522.9Hz can be generated by frequency mix between the following coordinate pairs (279.8+3SO), (440.9+1SO), and (684.1-1SO).

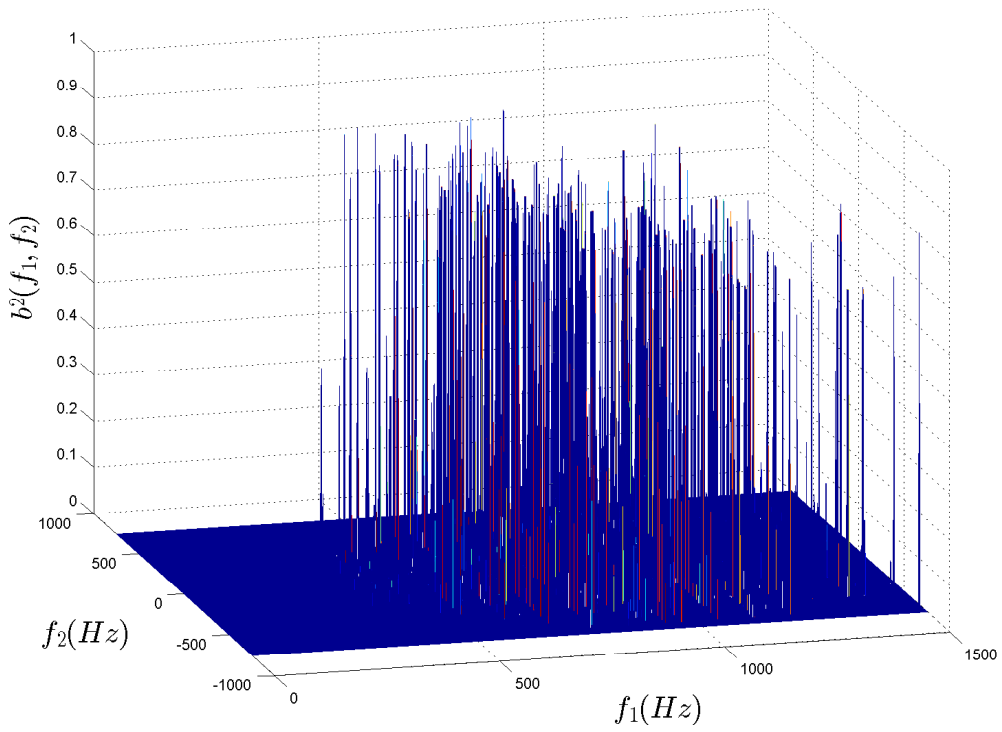

Figure 5.9 Bicoherence the coarse grit contaminated grease AHB

(a)

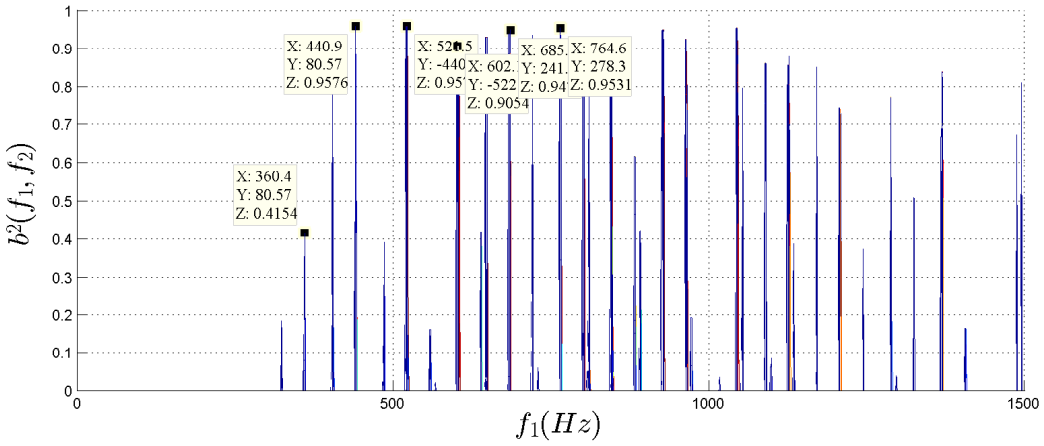

(b)

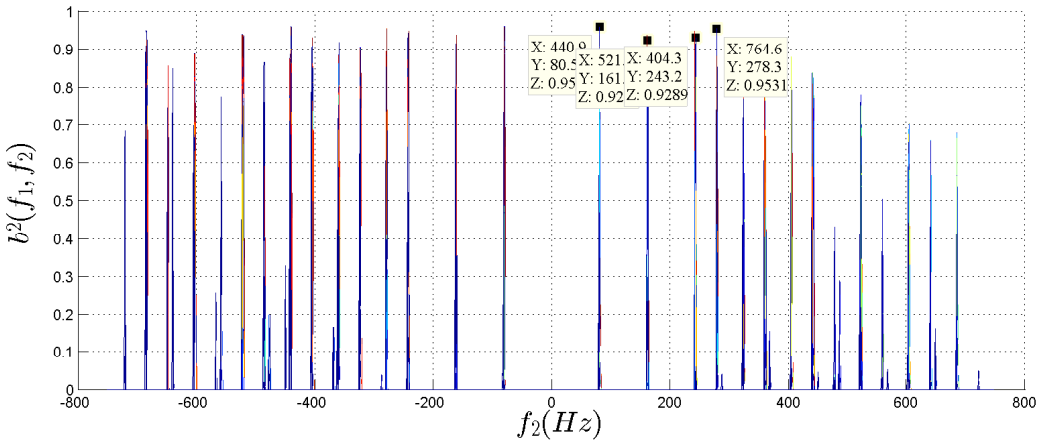

Figure 5.10 Projection of the bicoherence spectrum of the AHB vibration showing interaction with (a) f_1, and (b) f_2

5.5 Conclusion

In this chapter, $QNLPI(f)$ and bicoherence analysis have been used as bispectral tools to investigate nonlinear wave-wave interaction in vibration signals from an AH-64D helicopter drive-train simulating accelerated drive-train conditions under multiple faulted components. TRDT has been tested typically with faulted inner race in one hanger bearing, contaminated grease in another hanger bearing, misaligned and unbalanced drive shafts. The bispectral analysis have provided more details about the spectral content of the vibration signal and how different fault frequencies non-linearly interact with one another. Compared to linear power spectrum, bicoherence enables us to both detect the hanger bearing faults and also explain the source of new generated frequencies appear in the power spectrum of the vibration signal. Studying these cases bispectral analysis was useful to closing the loop between physical source of non-linearities and resultant frequencies showing up in the power spectrum of the vibration signal.

Chapter 6

Conclusion

In this dissertation, different signal processing techniques have been developed based on auto- and cross-bispectra as higher-order statistical analysis to assess health conditions of different critical rotating-components in an AH-64D helicopter tail rotor drive train.

Based on cross-bispectral analysis, vibration quadratic-nonlinearity metric has been proposed and used to assess health conditions of an AH-64D helicopter tail rotor drive shafts. Nonlinear transfer function has been derived from the cross-bispectrum in analogy to the way linear transfer function is derived from cross-power spectrum. Using system approach, vibration data collected at the bearing supporting the drive shaft has been used as input and output signals to characterize the unknown conditions of the drive shaft system. Vibration power at the shaft second-harmonic frequency ($2R$) has shown considerable increase in the studied faulted cases compared to the baseline case. Thus, this frequency has been used to compare between two condition indicators that characterize the shaft condition using two different approaches. Classical approach based on cross-power spectrum, on one hand, measures the second-order correlation (linear coupling) between the two vibration signals at the $2R$ frequency, $H(2R)$, and uses the phase of the coupling to diagnose different fault conditions. On the other hand, proposed approach in this paper measures the quadric coupling between the two signals that result in $2R$ frequency, $A_{QC}(1R, 1R)$, and also uses the phase of the quadratic coupling to diagnose different shaft faults.

Three different hanger bearings have been used to compare vibration data col-

lected from four different shaft settings, making grand total of twelve experiment runs. Magnitude response of both linear and quadratic coupling has been able to detect the faulted cases compared to the baseline case. However, theoretical and Monte-carlo type experimental analysis have proven that using condition indicators based on magnitude of the bispectrum has better immunity to white Gaussian noise than condition indicators based on magnitude of the conventional power spectrum. Moreover, using the phase of the proposed nonlinear coupling has shown better capabilities in distinguishing the four studied shaft settings than the conventional linear coupling. Phase of the $A_{QC}(1R, 1R)$ metric has shown more consistent result among the three studied bearing cases for each shaft setting than what the phase of $H(2R)$ has done. It also has shown wider phase difference between the studied cases without overlap among them. Wider phase difference relaxes the requirements when setting threshold values to diagnose different faulted cases.

The quadratic-nonlinearity power-index ($QNLPI(f)$) has been proposed which provides a summary of the nonlinearity information contained in the the 3D bicoherence into 2D spectrum presenting an easier way to studying third-order statistic of signals. The proposed index inherits useful characteristics of the bicoherence such as high immunity to additive gaussian noise, and amplification invariance; two properties of interest in practical applications to relax the pardon on sensors used in collecting time-varying waveforms.

The proposed index has been used to study real-world vibration data collected from tail-rotor drive train of an AH-64 helicopter. Two case studies have been conducted. In the first case, $QNLPI(f)$ has shown better diagnostic capabilities in differentiating between different drive-shaft faults by showing how different physical settings affect the nonlinear generation of harmonics. In the second case, $QNLPI(f)$ has shown better capability in detecting gearbox failure. For easier monitoring of the fault-progress in the gearbox, percentage of total quadratic nonlinear power

($PQNLP$) has been calculated based on the proposed $QNLPI(f)$ and has shown consistent increase during the gear fault aging. This single-valued metric can be used in prognostic models to estimate the remanding useful life of mechanical components.

It is worthwhile to mention here that although the proposed metrics provide more accurate tools to diagnose mechanical faults compared to the conventional power spectral analysis, this comes at the cost of computational resources and time. The computational complexity is $O(N^2)$ where N is the number of points in one signal realization. For example, for N= 4096, it takes 34.517 sec to compute the $QNLPI(f)$, while it takes 0.251 sec to compute the power spectral density using the same platform.

The behavior of the helicopter's tail-rotor drive-train under more than one simultaneous fault has been studied using the proposed signal analysis techniques. In the presence of drive-shaft faults, shaft harmonics have dominated the power spectra of the vibration signals collected form faulted hanger-bearing making it hard to detect bearing's faults. Also, unexpected frequencies have appeared in the vibration spectrum which can not be explained using conventional power spectral analysis. However, bispectral analysis tools have not only detected the bearing's faults in this extreme case of multi-faulted components, but also have shown better ability to relate all frequencies to their root causes and successfully link the signal processing to the physics of the underlying faults.

Future research in this area includes studying the effect of loading by the trail-rotor blades on the proposed metrics, and extending the application of the proposed metrics to study more faults and failure modes in aircrafts and similar rotating systems such as wind turbines. The unique nonlinearity signature of each fault can be used to design more accurate and reliable diagnostic algorithms for the condition based maintenance (CBM) practice.

Bibliography

[1] A. K.S. Jardine, D. Lin, and D. Banjevic, "A review on machinery diagnostics and prognostics implementing condition-based maintenance," *Mechanical Systems and Signal Processing*, vol. 20, no. 7, pp. 1483-1510, Oct. 2006.

[2] V. Blechertas, A. Bayoumi, N. Goodman, R. Shah, and Yong-June Shin, "CBM fundamental research at the university of south carolina: a systematic approach to U.S. army rotorcraft CBM and the resulting tangible benefits," *Presented at the American Helicopter Society Technical SpecialistsâĂŹ Meeting on Condition Based Maintenance*, Huntsville, AL, USA, pp. 1-20, Feb. 2009.

[3] K. Swearingen, W. Majkowski, B. Bruggeman, et al, "An Open System Architecture for Condition Based Maintenance Overview," *IEEE Aerospace Conference,* pp. 1-8, March 2007.

[4] ISO 13374 Standards, "Condition monitoring and diagnostics of machines," *International Organization for Standardization,* 2003.

[5] Link C. Jaw, "Recent Advancements in Aircraft Engine Health Management (EHM) Technologies and Recommendations for the Next Step," *Proc. of Turbo Expo, 50th ASME Int. Gas Turbine & Aeroengine Technical Congress,* Reno-Tahoe, Nevada, June, 2005.

[6] S. Kim, J. Choi, Y. Kim, "Fault detection and diagnosis of aircraft actuators using fuzzy-tuning IMM filter," *IEEE Transactions on Aerospace and Electronic Systems*, vol. 44, no. 3, pp. 940-952, Jul. 2008.

[7] Q. Cheng, P. K. Varshney, C. M. Belcastro, "Fault detection in dynamic systems via decision fusion," *IEEE Transactions on Aerospace and Electronic Systems*, vol. 44, no. 1, pp. 227-242, Jan. 2008.

[8] T. D. Batzel, D. C. Swanson, "Prognostic health management of aircraft power generators," *IEEE Transactions on Aerospace and Electronic Systems*, vol. 45, no. 2, pp. 473-482, Apr. 2009.

[9] H. M. Hashemian, W. C. Bean, "State-of-the-art predictive maintenance techniques," *IEEE Transactions on Instrumentation and Measurement*, vol. 60, no. 10, pp. 3480-3492, Oct. 2011.

[10] J. Yu, "Health condition monitoring of machines based on hidden markov model and contribution analysis," *IEEE Transactions on Instrumentation and Measurement*, vol. 61, no. 8, pp. 2200-2211, Aug. 2012.

[11] A. Tantawy, X. Koutsoukos, G. Biswas, "Aircraft power generators: hybrid modeling and simulation for fault detection," IEEE Transactions on Aerospace and Electronic Systems, vol. 48, no. 1, pp. 552-571, Jan. 2012

[12] P. Grabill, T. Brotherton, J. Berry, and L. Grant, "The US Army and National Guard Vibration Management Enhancement Program (VMEP): Data Analysis and Statistical Results," *Proceeding of the American Helicopter Society 58th Annual Forum*, Montreal, Cananda, pp. 1-15, June 2002.

[13] Intelligent Automation Corporation, AH-64 VMEP Crewmember Information Guide. Huntsville, AL, 2004.

[14] A. Bayoumi, W. Ranson, L. Eisner, and L.E. Grant, "Cost and effectiveness analysis of the AH-64 and UH-60 on-board vibrations monitoring system," *IEEE Aerospace Conference,* Big Sky, MT, pp. 3921-3940, Mar. 2005.

[15] A. Bayoumi, and L. Eisner, "Transforming the US Army through the Implementation of Condition-Based Maintenance," *Journal of Army Aviation,* May 2007.

[16] Damian Carr, "AH-64A/D Conditioned Based Maintenance (CBM) Component Inspection and Maintenance Manual Using the Modernized Signal Processor Unit (MSPU) or VMU (Vibration Management Unit)," Aviation Engineering Directorate Apache Systems, Alabama, Tech. Rep., Oct. 2010.

[17] N. Goodman, " Application of Data Mining Algorithms for the Improvement and Synthesis of Diagnostic Metrics for Rotating Machinery," Ph.D. dissertation, Dept. of Mech. Eng., USC, Columbia, SC, 2011.

[18] A. Bayoumi, N. Goodman, R. Shah, L. Eisner, L. Grant, and J. Keller, "Conditioned-Based Maintenance at USC - Part I: Integration of Maintenance Management Systems and Health Monitoring Systems through Historical Data Investigation," *Proceedings of AHS International Specialists' Meeting on Condition Based Maintenance,* Huntsville, AL, Feb. 2008.

[19] D. Coats, Cho Kwangik, Yong-June Shin, N. Goodman, V. Blechertas, and A. Bayoumi, "Advanced Time-Frequency Mutual Information Measures for Condition-Based Maintenance of Helicopter Drivetrains," *IEEE Transactions on Instrumentation and Measurement*, vol. 60, no. 8, pp. 2984-2994, Aug. 2011.

[20] G. Betta, C. Liguori, A. Paolillo, and A. Pietrosanto, "A DSP-based FFT-analyzer for the fault diagnosis of rotating machine based on vibration analysis," *IEEE Transactions on Instrumentation and Measurement*, vol. 51, no. 6, pp. 1316-1322, Dec. 2002.

[21] P. D. Samuel, and D. J. Pines, "A review of vibration-based techniques for helicopter transmission diagnostics," *Journal of Sound and Vibration*, vol. 282, no. 1-2, pp. 475-508, Apr. 2005.

[22] A. S. Sait, and Y. I. Sharaf-Eldeen, "A review of gearbox condition monitoring based on vibration analysis techniques diagnostics and prognostics," in *Rotating Machinery, Structural Health Monitoring, Shock and Vibration*, Vol. 8, T. Proulx, Ed. New York: Springer, 2011, pp. 307-324.

[23] W. Bartelmus, R. Zimroz, "Vibration condition monitoring of planetary gearbox under varying external load," *Mechanical Systems and Signal Processing*, vol. 23, no. 1, pp. 246-257, Jan. 2009.

[24] R. B. Randall, J. Antoni, "Rolling element bearing diagnostics-A tutorial," *Mechanical Systems and Signal Processing*, vol. 25, no. 2, pp. 485-520, Feb. 2011.

[25] J. Dybala, "Vibrodiagnostics of gearboxes using NBV-based classifier: A pattern recognition approach," *Mechanical Systems and Signal Processing*, vol. 38, no. 1, pp. 5âĂŞ22, July 2013.

[26] Y. Zhan, V. Makis, A. K. S. Jardine, "Adaptive model for vibration monitoring of rotating machinery subject to random deterioration," *Journal of Quality in Maintenance Engineering*, vol. 9, no. 4, pp. 351-375, 2003.

[27] W.J. Wang, R.M. Lin, "The application of pseudo-phase portrait in machine condition monitoring," *Journal of Sound and Vibration*, vol. 259, no. 1-2, pp. 1-16, January 2003.

[28] T. Koizumi, N. Tsujiuchi, Y. Matsumura, "Diagnosis with the correlation integral in time domain," *Mechanical Systems and Signal Processing*, vol. 14, no. 6, pp. 1003-1010, November 2000.

[29] R. R. Schoen, and T.G. Habetler, "Effects of time-varying loads on rotor fault detection in induction machines," *IEEE Transactions on Industry Applications*, vol.31, no. 4, pp.900-906, Jul/Aug 1995.

[30] R. G. T. De Almeida, S.A. Da Silva Vicente, and L.R. Padovese, "New technique for evaluation of global vibration levels in rolling bearings," *Shock and Vibration*, vol. 9, no. 4-5, pp. 225-234, 2002.

[31] Z. Liu, X. Yin, Z. Zhang, D. Chen, and W. Chen, "Online rotor mixed fault diagnosis way based on spectrum analysis of instantaneous power in squirrel cage induction motors,"*IEEE Transactions on Energy Conversion*, vol.19, no.3, pp. 485-490, Sept. 2004.

[32] B. Boashash, E. J. Powers, A. M. Zoubir, "*Higher-Order Statistical Signal Processing,*" Wiley, 1996.

[33] Leon W. Couch II, "*Digital and Analog Communications Systems (sixth ed.),*" New Jersey, Prentice Hall, 2001, pp. 406-409.

[34] John G. Proakis, and Dimitris G. Manolakis, "Power spectrum estimation," in *Digital Signal Proccessing: Principles, Algorithms, and Applications*, 4th ed. New Jersey: Prentice Hall, 2007, pp. 960-1040.

[35] Y. C. Kim, and E. J. Powers, "Digital bispectral analysis and its application to nonlinear wave interactions," *IEEE Transactions on Plasma Science*, vol. 7, no. 2, pp. 120-131, July 1979.

[36] B. Jang, C. Shin, E. J. Powers, and W. M. Grady, "Machine fault detection using bicoherence spectra," *Proceeding of the IEEE Instrumentation and Measurement Technology Conference*, vol. 3, no. 1, pp. 1661-1666, May 2004.

[37] James J. Zakrajsek, et al. "Rotorcraft health managment issues and challenges," *first international forum on integrated system health engineering and management in aerospace,* Nampa, California, pp. 1-20, Feb. 2006.

[38] P. Grabill, J. Seale, D. Wroblewski, and T. Brotherton, "iTEDS: the intelligent turbine engine diagnostic system," *Proceedings of 48 International Instrumentaion Symposium*, pp. 345-353, May 2002.

[39] C. Scheffer, P. Girdhar, "Practical Machinery Vibration Analysis and Predictive Maintenance," Oxford: Newnes, 2004.

[40] M. A. Hassan, A. Bayoumi, and Yong-June Shin, "Condition monitoring of helicopter drive-shafts using quadratic-nonlinearity metric based on cross-bispectrum," *to appear in the IEEE Transactions on Aerospace and Electronic Systems.*

[41] T. Kim, W. Cho, E. J. Powers, W. M. Grady, and A. Arapostathis, "ASD system condition monitoring using cross bicoherence," *proceeding of the IEEE electricship technologies symposium*, pp. 378-383, May 2007.

[42] R. B. Randall, "Fault Detection," in *Vibration-based Condition Monitoring: Industrial, Aerospace and Automotive Applications,* Wiley, 2011.

[43] S. M. Kay, "*Fundamentals of Statistical Signal Processing,*" Volume 2: Detection Theory, Prentice Hall, January 1998.

[44] H. L. VanTrees, "*Detection, Estimation, and Modulation Theory,*" John Wiley& Sons, December 1968.

[45] R. Ware and F. Lad, "*Approximating the distribution for sums of products of normal variables,*" University of Canterbury Research Report, 2003.

[46] T. W. S. Chow, and Gou Fei, "Three phase induction machines asymmetrical faults identification using bispectrum," *IEEE Transactions on Energy Conversioin*, vol. 10, no. 4, pp. 688-693, Dec. 1995.

[47] N. Arthur, and J. Penman, "Induction machine condition monitoring with higher order spectra," *IEEE Transactions on Industrial Electronics*, vol. 47, no. 5, pp. 1031-1041, Oct. 2000.

[48] T. Chow, and H.-Z. Tan, "HOS-based nonparametric and parametric methodologies for machine fault detection," *IEEE Transactions on Industrial Electronics*, vol.47, no. 5, pp. 1051-1059, Oct. 2000.

[49] M. A. Hassan, D. Coats, K. Gouda, Yong-June Shin, and A. Bayoumi, "Analysis of Nonlinear Vibration-Interaction Using Higher Order Spectra to Diagnose Aerospace System Faults," *proceeding of the IEEE Aerospace Conference*, March 2012.

[50] D. Coats, M. A. Hassan, N. Goodman, V. Blechertas, Yong-June Shin, and A. Bayoumi, "Design of advanced time-frequency mutual information measures for aerospace diagnostics and prognostics," *proceeding of the IEEE Aerospace Conference*, pp.1-8, March 2011.

[51] J. K. Sinha, K. Elbhbah, "A future possibility of vibration based condition monitoring of rotating machines," *Mechanical Systems and Signal Processing*, vol. 36, no. 1-2, pp. 231âĂŞ240, Jan. 2013.

[52] T-T. Ng, S-F. Chang, and Q. Sun, "Blind detection of photomontage using higher order statistics," *Proceeding of the IEEE International Symposium on Circuits and Systems (ISCAS)*, vol. 5, pp. 688-691, May 2004.

[53] K. C. Chua, V. Chandran, U. R. Acharya, and C. M. Lim, "Cardiac state diagnosis using higher order spectra of heart rate variability," *Journal of Medical Engineering & Technology*, vol. 32, no. 2, pp. 145âĂŞ155, March/April 2008.

[54] V. Chandran, and S. Elgar, "Pattern recognition using invariants defined from higher order spectra- One dimensional inputs," *IEEE Transactions on Signal Processing*, vol. 41, no. 1, pp. 205-212, Jan. 1993.

[55] V. Chandran, S. Elgar, and A. Nguyen, "Detection of mines in acoustic images using higher order spectral features," *IEEE Journal of Oceanic Engineering*, vol. 27, pp. 610- 618, Jul 2002.

[56] M. A. Hassan, D. Coats, Yong-June Shin, and A. Bayoumi, "Quadratic-nonlinearity power-index spectrum and its application in condition based maintenance (CBM) of helicopter drive trains," *Proceeding of the IEEE International Instrumentation and Measurement Technology Conference (I2MTC)*, pp. 1456-1460, May 2012.

[57] M. A. Hassan, A. Bayoumi, and Yong-June Shin, "Quadratic-Nonlinearity Index Based on Bicoherence and Its Application in Condition Monitoring of Drive-Train Components," *accepted to appear in the IEEE Transactions on Instrumentation and Measurement.*

[58] S. Elgar, and R.T. Guza, "Statistics of bicoherence,"*IEEE transaction on Acoustics Speech and Signal Processing*, vol. 36, no. 10, pp. 1667-1668, Oct. 1988.

[59] J. W. A. Fackrell, S. McLaughlin, and P. R. White, "Practical issures in the application of the bicoherence for the detection of quadratic phase coupling," *in IEEE signal processing ATHOS workshop on Higher-order statistics*, pp.310-314, 1995.

[60] J. M. Nichols, C. C. Olson, J. V. Michalowicz, and F. Bucholtz, "The Bispectrum and Bicoherence for Quadratically Nonlinear Systems Subject to Non-Gaussian

Inputs," *IEEE Transactions on Signal Processing*, vol. 57, no. 10, pp.3879-3890, Oct. 2009.

[61] H. He, and D. J. Thomson, "The Canonical Bicoherence- Part II: QPC Test and Its Application in Geomagnetic Data," *IEEE Transactions on Signal Processing*, vol. 57, no. 4, pp. 1285-1292, Apr. 2009.

[62] N. Goodman, A. Bayoumi, V. Blechertas, R. Shah, and Yong-June Shin, "CBM component testing at the university of south carolina: AH-64 tail rotor gearbox studies," *Presented at the American Helicopter Society Technical SpecialistsâĂŹ Meeting on Condition Based Maintenance*, Huntsville, AL, pp. 1-8, Feb. 2009.

[63] R. K. Mobley, "Failure-Mode Analysis," in *An Introduction to predictive Mainenance,* Elsevier, 2002.

[64] "Amendment 1 to the Test Plan for AH-64 seeded fault Tail Rotor Hanger Bearings, Aft and Forward hanger Bearing Assemblies," U.S. Aviation and Missile R&D, and Engineering Center Memorandum for Record AMSRD-AMR-AE-K, July 27, 2007.

[65] C. Scheffer, P. Girdhar, "*Practical Machinery Vibration Analysis and Predictive Maintenance,*" 2004.